

The Molecular Composition of Shadowed Protosolar Disk Midplanes beyond the Water Snowline

SHOTA NOTSU,^{1,*} KAZUMASA OHNO,² TAKAHIRO UEDA,^{3,4} CATHERINE WALSH,⁵ CHRISTIAN EISTRUP,³ AND
HIDEKO NOMURA⁴

¹*Star and Planet Formation Laboratory, RIKEN Cluster for Pioneering Research, 2-1 Hirosawa, Wako, Saitama 351-0198, Japan*

²*Department of Astronomy and Astrophysics, University of California, Santa Cruz, 1156 High St, Santa Cruz, CA 95064, USA*

³*Max Planck Institute for Astronomy, Königstuhl 17, D-69117 Heidelberg, Germany*

⁴*National Astronomical Observatory of Japan, 2-21-1 Osawa, Mitaka, Tokyo 181-8588, Japan*

⁵*School of Physics and Astronomy, University of Leeds, Leeds, LS2 9JT, UK*

(Received May 10, 2022; Revised July 25, 2022; Accepted August 7, 2022)

Submitted to ApJ

ABSTRACT

The disk midplane temperature is potentially affected by the dust traps/rings. The dust depletion beyond the water snowline will cast a shadow. In this study, we adopt a detailed gas-grain chemical reaction network, and investigate the radial gas and ice abundance distributions of dominant carbon-, oxygen-, and nitrogen-bearing molecules in disks with shadow structures beyond the water snowline around a protosolar-like star. In shadowed disks, the dust grains at $r \sim 3 - 8$ au are predicted to have more than $\sim 5 - 10$ times amounts of ices of organic molecules such as H_2CO , CH_3OH , and NH_2CHO , saturated hydrocarbon ices such as CH_4 and C_2H_6 , in addition to H_2O , CO , CO_2 , NH_3 , N_2 , and HCN ices, compared with those in non-shadowed disks. In the shadowed regions, we find that hydrogenation (especially of CO ice) is the dominant formation mechanism of complex organic molecules. The gas-phase N/O ratios show much larger spatial variations than the gas-phase C/O ratios, thus the N/O ratio is predicted to be a useful tracer of the shadowed region. N_2H^+ line emission is a potential tracer of the shadowed region. We conclude that a shadowed region allows the recondensation of key volatiles onto dust grains, provides a region of chemical enrichment of ices that is much closer to the star than within a non-shadowed disk, and may explain to some degree the trapping of O_2 ice in dust grains that formed comet 67P/Churyumov-Gerasimenko. We discuss that, if formed in a shadowed disk, Jupiter does not need to have migrated vast distances.

Keywords: Protoplanetary disks(1300) — Astrochemistry(75) — Planet formation(1241) — Interstellar molecules(849) — Interstellar abundances(832) — Exoplanet atmospheres(487)

1. INTRODUCTION

Protoplanetary disks are composed of bare and ice-coated refractory grains, and gas, which are the ingredients of planetesimals and planets (e.g., Williams & Cieza 2011; Öberg & Bergin 2021). Disks are chemically active environments which create simple and complex molecules, including organic material. The physical and

chemical conditions of protoplanetary disks determine the properties of forming planets, including mass and chemical composition (e.g., Öberg et al. 2011; Öberg & Bergin 2016, 2021; Madhusudhan et al. 2014; Pontoppidan et al. 2014; Eistrup et al. 2016, 2018; Cridland et al. 2017; Booth & Ilee 2019; Notsu et al. 2020; Schneider & Bitsch 2021; Turrini et al. 2021a; Mollière et al. 2022). In addition, molecular abundances in comets and other primitive small bodies in our solar system are determined by the combination of chemical evolution in the protosolar disk and inheritance from molecular clouds (e.g., Mumma & Charnley 2011; Caselli & Ceccarelli 2012; Walsh et al. 2014; Eistrup et al. 2016, 2018; Al-

Corresponding author: Shota Notsu
shota.notsu@riken.jp

* RIKEN Special Postdoctoral Researcher (SPDR, Fellow)

twegg et al. 2019; Drozdovskaya et al. 2019; Öberg & Bergin 2021).

The disk thermal structure plays a predominant role in controlling the disk chemical structure. The midplane temperature $T(r)$ in protoplanetary disks is determined by heating due to viscous dissipation (only in the innermost region) and the stellar irradiation grazing the disk surface (e.g., Oka et al. 2011; Mori et al. 2021). Since the amount of heating per unit volume from both of these sources decreases with increasing disk radius r , in a smooth (non-shadowed) disk the temperature monotonically decreases as the disk radius increases (Kusaka et al. 1970; Kenyon & Hartmann 1987; Chiang & Goldreich 1997; Oka et al. 2011). Inside the water snowline H_2O ice evaporates from the dust grain surfaces into the gas phase, whereas outside it is frozen out onto the dust grain surfaces (Hayashi 1981). In addition, the cold outer disk is needed for the formation of various complex organic molecules, since the sequential hydrogenation of CO on the cold ($T(r) \sim 10 - 30$ K) dust grain surfaces leads to the formation of H_2CO and CH_3OH , which are key feedstock molecules that produce more complex organic molecules (e.g., Tielens & Hagen 1982; Watanabe & Kouchi 2002; Cuppen et al. 2009; Fuchs et al. 2009; Drozdovskaya et al. 2014; Furuya & Aikawa 2014; Walsh et al. 2014, 2016; Chuang et al. 2016; Bosman et al. 2018; Aikawa et al. 2020).

Under the assumption of classical monotonically decreasing disk temperature profiles, previous studies have discussed the disk radial locations of formation of planets. Here we introduce the examples of Jupiter in the Solar System. Recent extensive observations towards Jupiter’s atmosphere (by the Galileo probe, Cassini, and Juno spacecraft) have revealed uniform enrichment patterns of the elemental abundances from protosolar abundances by a factor of two to four (see e.g., Atreya et al. 2020; Li et al. 2020). The heavy element enrichment has been proposed to originate from planetesimals and/or pebbles dissolved in the atmospheres (e.g., Pollack et al. 1986; Iaroslavitz & Podolak 2007; Hori & Ikoma 2011; Venturini et al. 2016; Shibata & Helled 2022) and/or core erosion (e.g., Moll et al. 2017). It has been noted that the abundances of highly volatile elements, such as N and noble gas elements, are comparable to the other elemental abundances. Owen et al. (1999) suggested that this uniform enrichment originates from planetesimals formed in extremely cold ($T(r) < 30$ K) environments, where nitrogen and noble gases can freeze. Öberg & Wordsworth (2019) and Bosman et al. (2019) suggested that such uniform en-

richment could be explained if the Jovian core had formed at $r > 30$ au, where the disk temperature is extremely cold ($T(r) < 30$ K, outside the N_2 snowline) under the classical monotonically decreasing disk temperature profile. However, according to theoretical studies on core formation and migration (Bitsch et al. 2019), the occurrence rate of the migration of a core from $r > 30$ au to 5 au is extremely low, and the core migration time scale is of the order of a few Myr even if such a migration occurs. Kruijer et al. (2017, 2020) discussed that Jupiter’s core may be formed within 1 Myr to demarcate the inner and outer Solar System, on the basis of the isotope analyses of meteorites.

However, the disk temperature profile may not have a monotonically decreasing distribution if a disk has substructures, as found in recent observations of radial gas and dust distributions on many disks (e.g., Isella et al. 2018; Andrews 2020; Öberg et al. 2021). Several previous studies have suggested that a shadowed region where the direct stellar light does not reach is potentially generated, depending on the inner disk density structure. A puffed inner disk rim can block the radiation from the central star and cast a shadow, so-called self-shadowing (e.g., Dullemond et al. 2001; Dullemond & Dominik 2004; Dullemond & Monnier 2010; Flock et al. 2016; Ueda et al. 2017). Ueda et al. (2019) showed that a dust pileup at the inner edge of the MRI (magnetorotational instability) dead-zone casts a shadow behind it, producing cold regions of $T(r) \sim 50$ K at $r \sim 2 - 7$ au around Herbig Ae/Be stars. Jang-Condell & Turner (2012), Turner et al. (2012), Isella & Turner (2018), and Okuzumi et al. (2022) described that the outer wall of the gap produced by a giant planet receives extra starlight heating and puffs up, throwing a shadow across the disk beyond. Isella & Turner (2018) showed that the surface brightness contrast between the outer wall and shadow for the $1000 M_{\oplus}$ ($\sim 3.1 M_{\text{Jupiter}}$) planet is an order of magnitude greater than a model neglecting the temperature disturbances. In addition, Ueda et al. (2021) and Okuzumi et al. (2022) discussed that a small puffed-up rim and outer shadowed region will result in the formation of ring and gap structures in disks by thermal wave instabilities (TWI). Recently, Ohashi et al. (2022) found a steep temperature decrease outside the dust clumps at $r \sim 20$ au in the disk around Class 0/I protostar L1527 IRS. They suggest that the dust clumps create a shadowed region outside, resulting in the sudden drop in temperature.

A dust pileup at the water snowline may also cast a shadow behind it. The dust surface density just inside

the water snowline can be enhanced by orders of magnitude. This is because efficient fragmentation slows the radial drift of silicate grains, leading to enhanced production of small grains within the water snowline (e.g., Birnstiel et al. 2010; Banzatti et al. 2015; Cieza et al. 2016; Pinilla et al. 2017; Müller et al. 2021). Such fragmented dust, with higher surface density and scale height, will cast a shadow behind the water snowline and provide cold environments where volatile materials can freeze (Ueda et al. 2019; Ohno & Ueda 2021).

These disk shadow structures may have a significant effect on the atmospheric composition of planets forming within. Ohno & Ueda (2021) computed the temperature structure of a proto-solar (T Tauri) disk which has a shadowed region beyond the water snowline, and investigated the radial volatile distributions. They found that the vicinity of the current orbit of Jupiter ($r \sim 5$ au) could be $T(r) < 30$ K if the small-dust surface density decreases by a factor of $\gtrsim 30$ across the water snowline. They discussed that the shadow can cause the condensation of most volatile substances, namely N_2 and noble gases, and that the dissolution of shadowed solids can explain the elemental abundance patterns of the Jovian atmosphere even if Jupiter formed near the current orbit. However, Ohno & Ueda (2021) included limited carbon, nitrogen, oxygen-bearing molecules (H_2O , CO, CO_2 , C_2H_6 , N_2 , and NH_3 only, see also Öberg & Wordsworth 2019). In addition, they fixed the total (gas+ice) abundances of each volatile and calculated the balance between thermal desorption and freeze-out onto dust grains within each molecular species only. In order to investigate the effects of the shadow beyond the water snowline on disk chemical evolution including H_2CO , CH_3OH , and more complex organic molecules (such as e.g., NH_2CHO and $HCOOCH_3$), more detailed gas-grain chemical modeling is needed (e.g., Walsh et al. 2014, 2015; Eistrup et al. 2016, 2018; Bosman et al. 2018; Notsu et al. 2021).

In this study, we calculate the chemical structure of a shadowed disk midplane around a T Tauri star (a protosolar-like star), using a detailed gas-grain chemical reaction network. We investigate the radial abundance distributions of dominant carbon-, oxygen-, and nitrogen-bearing molecules and the radial distributions of elemental abundance ratios (C/O and N/O ratios) in the gas and ice of disks with shadow structures. We also investigate the dependence of the disk chemical structures on ionisation rates and initial abundances. We discuss the effects of disk shadowing on chemical evolution of complex organic molecules and forming planetary

atmospheres. We also discuss the implications of our results for the chemical composition of comets and asteroids in the Solar System. The outline of our model calculations are explained in Section 2. The results and discussion of our calculations are described in Sections 3 and 4, respectively. The conclusions are presented in Section 5.

2. METHODS

2.1. The physical model of the protoplanetary disk midplane

We adopt the physical model of a steady, axisymmetric Keplerian disk around a T Tauri star (a protosolar-like star) with mass $M_* = 1.0 M_\odot$, radius $R_* = 2.6 R_\odot$, and effective temperature $T_* = 4300$ K. For the disk density structure, we adopted the same parameterized disk model as Ohno & Ueda (2021) in which the dust surface density steeply varies around the water snowline. The radial surface density profiles are described by the following equations,

$$\Sigma_{\text{gas}}(r) = 670 \left(\frac{r}{1 \text{ au}} \right)^{-3/5} \text{ g cm}^{-2}, \quad (1)$$

$$\Sigma_{\text{dust}}(r) = \begin{cases} 0.01 \Sigma_{\text{gas}}(r) & (r < R_{\text{SL}}(H_2O)) \\ 0.01 f \Sigma_{\text{gas}}(r) & (r \geq R_{\text{SL}}(H_2O)), \end{cases} \quad (2)$$

where r is the disk radius from the central star, Σ_{gas} is the gas surface density, Σ_{dust} is the surface density of the small dust ($0.1 - 100 \mu\text{m}$) which contribute to the dust opacity, $R_{\text{SL}}(H_2O) = 1.3$ au is the assumed radial position of the water snowline. In protoplanetary disks, the maximum grain size is expected to be larger than that of the typical ISM dust due to significant dust growth. However, large grains ($\gtrsim 100 \mu\text{m}$) have little impact on the disk temperature structure because they have small opacity and are depleted at the disk surface where stellar irradiation is absorbed. The power index of the radial gas surface density profile ($= -3/5$) is calculated under the assumption of a disk with steady accretion and viscous heating (e.g., Nakamoto & Nakagawa 1994; Oka et al. 2011). We adopted various values of the parameter f ($= 1.0$ to 0.3 , 0.03 , and 0.003) to investigate the effects of the magnitude of shadowing on the disk thermal and chemical structures. The actual values of the parameter f depend on the efficiency of fragmentation of silicate and icy grains, which is controlled by the turbulence viscosity strength and stickiness of the dust grains (e.g., Birnstiel et al. 2010; Banzatti et al. 2015; Pinilla et al. 2017). Banzatti et al. (2015) reported

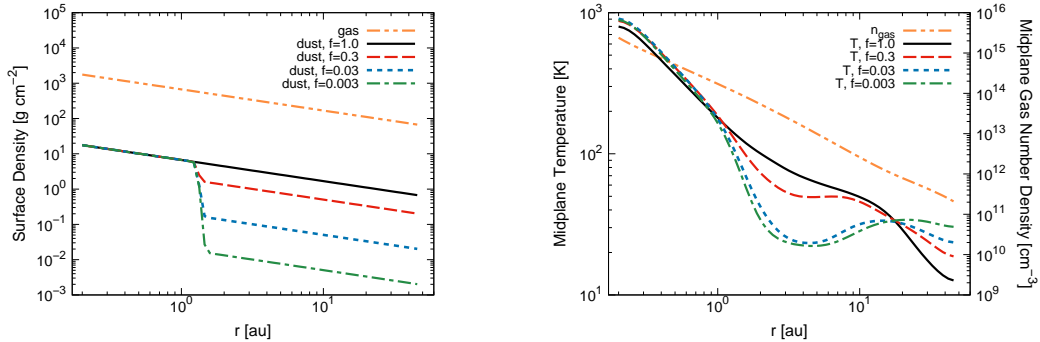


Figure 1. Physical structures of the adopted disk models with shadow structures beyond the water snowline. [Left panel]: The radial profiles of the gas surface density $\Sigma_{\text{gas}}(r)$ [g cm^{-2}] (orange dashed double-dotted line) and the dust surface density $\Sigma_{\text{dust}}(r)$ [g cm^{-2}]. [Right panel]: The radial profiles of the gas number density $n_{\text{gas}}(r)$ [cm^{-3}] (orange dashed double-dotted line) and the temperature $T(r)$ [K] in the disk midplane. In the profiles of $\Sigma_{\text{dust}}(r)$ and $T(r)$, the black solid lines, the red dashed lines, the blue dotted lines, and the green dashed dotted lines show the profiles for different values of the parameter f ($=1.0, 0.3, 0.03$, and 0.003), respectively.

dust surface density variations of $f \sim 0.1, 0.001$, and 0.01 around the water snowline for turbulence viscosity strengths of $\alpha_t^1 = 10^{-2}, 10^{-3}$, and 10^{-4} , respectively.

The disk midplane temperature profiles were extracted from the results of the 2D thermal model calculation in Ohno & Ueda (2021) (see also Section 2 in Ueda et al. 2019). In this calculation, the above radial density profiles (see Equations 1 and 2) are adopted and the Monte Carlo radiative transfer code RADMC-3D (Dullemond et al. 2012) is used. Scattering is assumed to be isotropic because full-scattering treatment is computationally expensive. We expect that the temperature structure is not significantly modified even if we consider the full scattering because the temperature at the shadowed region seems to be insensitive to the presence of scattering (Ueda et al. 2019). The vertical dust density distribution and the temperature structure are mutually dependent, thus the radiative transfer calculations were iteratively performed to obtain a self-consistent disk structure (for more details, see Ueda et al. 2019). The calculations also include the internal radiative flux produced by viscous accretion, q_{acc} , determined by the following equation (Lynden-Bell & Pringle 1974; Pringle 1981; Nomura & Millar 2005),

$$q_{\text{acc}} = \frac{9}{4} \alpha_t \rho_{\text{gas}} c_s^2 \Omega_K, \quad (3)$$

¹ α_t is a dimensionless parameter to quantify the disk viscosity (Shakura & Sunyaev 1973).

where α_t is set to be 3×10^{-4} , ρ_{gas} is the gas mass density, c_s is the sound speed, and Ω_K is the Keplerian frequency. The surface density coefficient ($\Sigma_0 = 670 \text{ g cm}^{-2}$) and α_t in Equation 1 are adjusted so that the water snowline position is outside the current Earth orbit ($=1.3 \text{ au}$) in the calculation of the temperature profiles. We note that we have adopted the same dust surface density within the water snowline in all models so that the position of the water snowline is fixed. This is because in this study we focus on the effects of shadowing on disk chemical structures beyond the water snowline. Eistrup et al. (2016) adopted the lower surface density model ($\Sigma_{\text{gas}}(5.2 \text{ au}) = 16 \text{ g cm}^{-2}$) than our adopted model ($\Sigma_{\text{gas}}(5.2 \text{ au}) = 249 \text{ g cm}^{-2}$), and the water snowline position in their model is around 0.7 au . We assume the same dust and gas temperatures ($T_{\text{dust}} = T_{\text{gas}} = T$), which is a valid assumption in the dense molecular regions of the disk. The radial profile of the midplane gas mass density $\rho_{0,\text{gas}}(r)$ is given by the following equation,

$$\rho_{0,\text{gas}}(r) = \frac{\Sigma_{\text{gas}}(r)}{\sqrt{2\pi} h_{\text{gas}}}, \quad (4)$$

where $h_{\text{gas}} = c_s/\Omega_K$ is the gas scale height. We adopted the DSHARP dust opacity model (Birnstiel et al. 2018, see also e.g., Henning & Stognienko 1996; Draine 2003; Warren & Brandt 2008), and assumed a dust-size distribution that follows a power law with an index of -3.5 , similar to the MRN distribution (Mathis et al. 1977), with minimum and maximum dust radii of 0.1 and $100 \mu\text{m}$, respectively. We assume that larger grains have been removed from the disk atmosphere by settling and

radial drift. The bulk densities of dust grains ρ_{internal} are set to be 3.0 g cm^{-3} for the region where the icy component is evaporated ($T > 160 \text{ K}$) and 1.4 g cm^{-3} elsewhere. We note that icy grains can efficiently coagulate into larger ($\gg 1 \text{ mm}$) dust particles and cm-size pebbles outside the water snowline (e.g., Ros & Johansen 2013; Sato et al. 2016; Drążkowska & Alibert 2017; Pinilla et al. 2017), but such large dust particles and pebbles have negligible contribution to the opacity compared with that of smaller dust particles (Miyake & Nakagawa 1993), and they are confined to the disk midplane. Thus, Σ_{dust} is not necessarily the same as the total surface density of all solid components (dust grains and pebbles), for example outside the water snowline (Banzatti et al. 2015). We note that in our disk chemical modeling (see Section 2.2), we use the dust density profile in the disk midplane calculated from this small dust (0.1-100 μm) surface density profile Σ_{dust} .

The left panel of Figure 1 shows $\Sigma_{\text{gas}}(r)$ and $\Sigma_{\text{dust}}(r)$ for different values of the parameter f ($=1.0, 0.3, 0.03$, and 0.003). The right panel of Figure 1 shows the radial profiles of the gas number density $n_{\text{gas}}(r)$ and temperature $T(r)$ in the disk midplane for different values of the parameter f . $n_{\text{gas}}(r)$ is calculated by dividing $\rho_{0,\text{gas}}(r)$ by the mean particle mass ($=2.33 \text{ amu}$). The values of n_{gas} are largest in the innermost region ($\gtrsim 10^{14} \text{ cm}^{-3}$ at $r \lesssim 1.4 \text{ au}$), and decrease as the value of r increases ($\lesssim 10^{12} \text{ cm}^{-3}$ at $r \gtrsim 17 \text{ au}$). The value of T within the water snowline is independent of f , and is primarily controlled by viscous heating, yielding the radial dependence of $\propto r^{-9/10}$ (Oka et al. 2011).

As demonstrated in Ohno & Ueda (2021), the depletion of small dust grains outside the water snowline casts a shadow, changing the disk midplane temperature significantly. In the cases of smaller values of f , the decrease of dust surface density outside the water snowline results in reduced dust opacity, which reduces the amount of stellar radiation received per unit volume and cools the outer region compared with the case of the non-shadowed disk ($f = 1.0$). The values of T at $r \sim 1.3 - 17 \text{ au}$ decrease with decreasing f , as the shadow extends to farther-out. Even in the case of a small variation in the dust density profile with $f = 0.3$, T is around 20 K lower than that in the non-shadowed disk with $f = 1.0$. For $f \geq 0.03$, T is $< 30 \text{ K}$ at $r \sim 3 - 8 \text{ au}$, and $< 25 \text{ K}$ at around the current orbit of Jupiter ($\sim 5 \text{ au}$). In contrast, the values of T at $r > 20 \text{ au}$ increase with decreasing f , although the degree of increase is small and T is $< 35 \text{ K}$ even for $f = 0.003$. We interpret that reduced dust surface density beyond

the water snowline allows the reprocessed stellar radiation to enter the outer disk midplane from the upper disk surface (Cleeves 2016). At the outer disk midplane ($r > 20 \text{ au}$), the heating effect by such radiation overcomes the cooling effect which reduces as r increases. The disk temperature is expected to be higher in the outer disk (beyond $r > 20 \text{ au}$) if we assume lower surface densities than we assumed. The values of disk masses are determined by the density profile in the outer region of the disk. We note that we have adopted the surface densities following a single power-law profile for the sake of simplicity (see Equations 1 and 2). The disk gas mass within 20 au and 40 au is $\sim 2.2 \times 10^{-2} M_{\odot}$ and $\sim 5.8 \times 10^{-2} M_{\odot}$, respectively. Eistrup et al. (2016) adopted a disk surface density profile with an outer exponential cutoff radius of $r_c = 20 \text{ au}$. If we include such outer exponential cutoff with $r_c \sim 20 \text{ au}$ in the disk surface density profile, the total disk mass within 40 au will be around half of the value without cutoff. Recently, Trapman et al. (2022) estimated from HD and C¹⁸O line observations that the disk masses for some typical Class II T Tauri disks (such as TW Hya) are around a few $\times 10^{-2} M_{\odot}$.

We assumed that the water snowline position as 1.3 au, but it might be outside the current orbit of Mars (1.52 au). Hansen (2009) discussed that Mars forms from a protoplanet that has moved by scattering from near the current orbit of Earth.

In our calculations, the FUV and X-ray radiation from both the central T Tauri star and interstellar radiation fields are neglected, since the disk has a high surface density ($\Sigma_{\text{gas}}(r) \sim 10^2 - 10^3 \text{ g cm}^{-3}$) and the disk midplane is effectively shielded (e.g., Nomura & Millar 2005; Nomura et al. 2007; Walsh et al. 2015).

Cleeves et al. (2014b), Eistrup et al. (2016, 2018), and Schwarz et al. (2018, 2019) discussed that disk chemical evolution (such as chemical processing of CO) are affected by the degree of (cosmic-ray) ionization. In order to investigate the effects of ionization on chemistry in the shadowed disk, we adopt two values of radially constant ionization rates $\xi_{\text{CR}}(r) = 1.0 \times 10^{-17} [\text{s}^{-1}]$ and $1.0 \times 10^{-18} [\text{s}^{-1}]$ (e.g., Cleeves et al. 2014b; Eistrup et al. 2016, 2018). The former high ionization value includes contributions from the decay products of short-lived radionuclides (SLRs) (Cleeves et al. 2013a,b) and from cosmic-rays, originating externally to the disk (e.g., Umebayashi & Nakano 2009; Padovani et al. 2018), whereas the latter low ionisation value considers contribution from the decay products of SLRs only. We note

that, in reality, the ionization rate has radial dependence, since the contribution from SLRs decreases as r increases (Cleeves et al. 2013b) and that from cosmic-rays increases as r increases (e.g., Umebayashi & Nakano 2009; Padovani et al. 2018; Aikawa et al. 2021; Seifert et al. 2021; Fujii & Kimura 2022). Using the Equation (30) of Cleeves et al. (2013b) and our assumed $\Sigma_{\text{gas}}(r)$ profile, the ionization rates for the contribution from SLRs are estimated to be $\sim 5 \times 10^{-19} [\text{s}^{-1}]$ at $r \sim 5$ au and $\sim 7 \times 10^{-19} [\text{s}^{-1}]$ at $r \sim 1$ au. Nonetheless, we assume a constant value of the ionization rate at all radii to clarify its impacts on the disk chemical evolution.

2.2. Calculation of the disk chemical structure

We calculated the chemical evolution of the shadowed disk midplane around a T Tauri star (a protosolar-like star) using a detailed gas-grain chemical reaction network. The chemical reaction network adopted in this work is basically similar to that in Notsu et al. (2021). The detailed background theories and procedures are also discussed in our previous works (e.g., Walsh et al. 2010, 2012, 2014, 2015, Heinzeller et al. 2011, Eistrup et al. 2016, 2018; Eistrup & Walsh 2019, Notsu et al. 2016, 2017, 2018, 2019), although there are some differences between the models in these studies and our adopted model which we explain in this Section. Our model calculates the time-dependent chemical evolution at the disk midplane of each radial distance and does not include physical mass transport in the radial direction by viscous accretion and in the vertical direction by diffusive turbulent mixing and disk winds (Heinzeller et al. 2011).

2.2.1. Gas-phase reactions

Our gas-phase chemistry includes the complete network from the release of the UMIST Database for Astrochemistry (UDfA), called RATE12, and is publicly available² (McElroy et al. 2013). RATE12 includes gas-phase two-body reactions, photoionization and photodissociation, direct cosmic-ray ionization, and cosmic-ray-induced photoionization and photodissociation. Since the FUV radiation fields from the central T Tauri star and interstellar FUV fields are neglected in our calculations (see also Section 2.1), the photodissociation and photoionization by FUV radiation are effectively zero. In the cosmic-ray-induced photoreactions, UV photons are generated internally via the interaction of secondary electrons produced by cosmic-rays with H_2 molecules (Gredel et al. 1987, 1989).

² <http://udfa.ajmarkwick.net>

Table 1. The binding energies for the major molecules $E_{\text{des}}(j)$ and their estimated snowline positions $R_{\text{SL}}(j)$ in the non-shadowed disk ($f = 1.0$)

Species j	$E_{\text{des}}(j)$ [K]	$R_{\text{SL}}(j)$ [au]
NH_2CHO	5560	~ 1.2
H_2O	4880	1.3
CH_3OH	3820	~ 1.5
HCN	3610	~ 1.5
H_2CO	3260	~ 1.8
NH_3	2715	~ 2.3
C_2H_6	2320	~ 3.2
CO_2	2267	~ 3.3
CH_4	1252	~ 15
O_2	898	~ 20
CO	855	~ 22
N_2	790	~ 24
H	650	~ 34
H_2	430	~ 35

As in Walsh et al. (2015), we also added a set of three-body reactions and “hot” H_2 chemistry, although they are not expected to be important around the water snowline ($\sim 100 - 200$ K). Moreover, the gas phase chemical network is supplemented with reactions for important species, for example the CH_3O radical, which are not included in RATE12. The gas-phase formation and destruction reactions for these species are from the Ohio State University (OSU) network (Garrod et al. 2008).

2.2.2. Gas-grain interactions

As in Notsu et al. (2021), we include the freeze-out of gas-phase molecules on dust grains, and the thermal and non-thermal desorption of molecules from dust grains (Hasegawa et al. 1992; Walsh et al. 2010, 2012; Notsu et al. 2016). As non-thermal desorption mechanisms, cosmic-ray-induced photodesorption, reactive desorption (see Section 2.2.3), and direct cosmic-ray-induced (thermal) desorption (Leger et al. 1985; Hasegawa & Herbst 1993; Hollenbach et al. 2009) are adopted. We note that the direct cosmic-ray-induced (thermal) desorption has no significant impact on chemistry, since its reaction timescale is typically much longer ($\gg 10^7$ years) than the age of Class II disk (Hollenbach et al. 2009). We adopt the value for the integrated cosmic-ray-induced UV photon flux as $10^4 \text{ photons cm}^{-2} \text{ s}^{-1}$ (Prasad & Tarafdar 1983; Walsh et al. 2014). We scale the internal UV photon flux by the cosmic-ray ionization rate. On the basis of the adopted dust-size distribution (see Section 2.1), we assume compact spherical grains with an average radius a of $0.1 \mu\text{m}$. We note that

the total dust surface area is mainly dominated by the smallest dust grains, under the MRN distribution. The values of photodesorption yields adopted in this work, $Y_{\text{des}}(j)$, are the same as those adopted in Notsu et al. (2021). We use experimentally determined photodesorption yields, where available (e.g., Öberg et al. 2007, 2009a,b; Fillion et al. 2014; Bertin et al. 2016; Cuppen et al. 2017, see Table 1 of Notsu et al. 2021). For all species without experimentally determined photodesorption yields, a value of 10^{-3} molecules photon $^{-1}$ is used. As in Notsu et al. (2021), we include the fragmentation pathways for photodesorption of water and methanol molecules (e.g., Öberg et al. 2009b; Arasa et al. 2010, 2015; Bertin et al. 2016; Cruz-Diaz et al. 2016).

The sticking coefficient is assumed to be 1 for all species, except for H, which leads to H $_2$ formation (for more details, see Appendix B.2 of Bosman et al. 2018). We adopt the same values of the binding (desorption) energies $E_{\text{des}}(j)$ for all molecules as used in Notsu et al. (2021). In Table 1, $E_{\text{des}}(j)$ for several dominant molecules and their estimated snowline positions $R_{\text{SL}}(j)$ in the non-shadowed disk ($f = 1.0$) are listed (see also Section 3). We defined the snowline positions as the radii where the gas and ice abundances of each molecule are the same because of the balance between thermal desorption and freeze-out. We note that the binding energies of molecules depend on the chemical compositions and physical structures (e.g., crystal or amorphous) of the ice mantles on the dust grains (e.g., Cuppen et al. 2017; Penteado et al. 2017; Kouchi et al. 2021, see also Section 4.2). For CO and N $_2$, we assume the values of pure CO and N $_2$ ices, respectively (Öberg et al. 2005).

2.2.3. Grain-surface reactions

For the grain-surface reactions, we adopt the same reaction network as Notsu et al. (2021) used. Those reactions are mostly based on the Ohio State University (OSU) network (Garrod et al. 2008), with including some extended network for some molecules (such as CH $_3$ OH and NH $_2$ CHO, see Section 2.2.3 of Notsu et al. 2021 and e.g., Noble et al. 2015; Chuang et al. 2016). In addition to grain-surface two-body reactions (Hasegawa et al. 1992) and reactive desorption, grain-surface cosmic-ray-induced photodissociation is also included in our calculations (Garrod et al. 2008; Walsh et al. 2014, 2015). Only the top two monolayers of the ice mantle are chemically active. We assume that the size of the barrier to surface diffusion is $0.3 \times E_{\text{des}}(j)$ (Walsh et al. 2015). For the lightest reactants, H and H $_2$, we adopt either the classical diffusion rate or the quantum

tunneling rate depending on which is fastest (Hasegawa et al. 1992; Bosman et al. 2018). For the quantum tunneling rates, we adopt a rectangular barrier of width 1.0 Å (Hasegawa et al. 1992; Bosman et al. 2018).

2.2.4. Initial abundances

As Eistrup et al. (2016, 2018) conducted, the disk chemical evolution is calculated with two different sets of initial abundances: molecular species and atomic species. All abundances in our calculations of this paper are with respect to the total number density of H nuclei. For both sets of initial abundances (molecular and atomic) the elemental ratios are consistent. The choice of these initial abundances is motivated by the following two extreme scenarios about the history of the disk midplane material (Öberg & Bergin 2021; van Dishoeck et al. 2021).

The use of molecular initial abundances assumes that the disk material is wholly inherited from the molecular cloud and the pre-stellar core from which the central star formed, implying a more quiescent mode of disk formation. The enhanced deuterium fractionation of water and organic molecules in disks is considered to be a probe of pre-stellar inheritance, since efficient deuteration of water and organic molecular ices is only possible in cold and embedded pre-stellar cloud cores where UV radiation is almost completely attenuated and CO is frozen-out onto dust grains (e.g., Cleeves et al. 2014a; Furuya et al. 2016, 2017; Drozdovskaya et al. 2019; Jensen et al. 2021). Drozdovskaya et al. (2019) described that the relative abundances of volatile organic molecules (with respect to e.g., methanol) correlate, with some scatter, between ALMA data towards the protostar IRAS 16293-2422 B and Rosetta’s in-situ monitoring data of comet 67P/Churyumov-Gerasimenko. This result implies that the volatile composition of solar system comets may be partially inherited from the pre-stellar and protostellar phases. In contrast, the use of atomic initial abundances implies that full chemical reset has occurred during disk formation. Throughout disk formation, infalling material is subject to radiation from the central star and accretion shocks, which may alter the chemical composition of material (e.g., Visser et al. 2009; Drozdovskaya et al. 2016; Miura et al. 2017; Notsu et al. 2021). Öberg & Bergin (2021) and van Dishoeck et al. (2021) discussed that neither a complete inheritance nor a complete reset scenario can explain the results of recent disk observations (by e.g., ALMA) and the full solar system record. They described that both must have played an important role during disk formation.

Table 2. Initial gas and ice molecular abundances with respect to total H nuclei assumed in the inheritance scenario.

Species j	$n_{j,\text{gas}}/n_{\text{H}}$	$n_{j,\text{ice}}/n_{\text{H}}$
H	3.807×10^{-5}	4.458×10^{-17}
H ₂	4.997×10^{-1}	4.140×10^{-5}
He	9.750×10^{-2}	7.823×10^{-20}
H ₂ O	7.080×10^{-7}	1.984×10^{-4}
O	0.0	2.073×10^{-13}
O ₂	0.0	4.035×10^{-12}
OH	5.164×10^{-8}	6.019×10^{-14}
C	2.571×10^{-8}	1.310×10^{-16}
CO	7.532×10^{-5}	2.946×10^{-5}
CO ₂	7.487×10^{-7}	2.856×10^{-7}
CH ₄	1.120×10^{-6}	7.384×10^{-6}
C ₂ H ₆	1.152×10^{-7}	2.417×10^{-6}
H ₂ CO	1.108×10^{-7}	8.437×10^{-6}
CH ₃ OH	3.558×10^{-9}	6.027×10^{-7}
N	2.105×10^{-5}	5.531×10^{-14}
N ₂	9.765×10^{-6}	5.411×10^{-6}
NH ₃	2.933×10^{-7}	1.327×10^{-5}
HCN	7.718×10^{-8}	2.772×10^{-6}
NH ₂ CHO	2.811×10^{-10}	4.155×10^{-7}
CN	3.016×10^{-9}	1.406×10^{-15}
NO	3.453×10^{-8}	7.510×10^{-17}
OCN	5.379×10^{-10}	8.189×10^{-19}
C ₂ H	1.776×10^{-10}	5.537×10^{-17}
C ₂ H ₂	7.440×10^{-8}	3.291×10^{-10}
C ₂ H ₄	1.516×10^{-8}	2.009×10^{-10}
C ₃ H ₂	5.416×10^{-8}	8.463×10^{-10}
CH ₃ CCH	1.514×10^{-8}	5.170×10^{-7}
CH ₂ CCH ₂	1.698×10^{-8}	5.171×10^{-7}
CH ₃ CHCH ₂	3.296×10^{-8}	1.691×10^{-9}
CH ₃ NH ₂	5.982×10^{-10}	4.645×10^{-7}
CH ₂ NH	4.834×10^{-10}	1.185×10^{-10}
CH ₃ CN	1.029×10^{-9}	1.033×10^{-8}
HC ₃ N	6.041×10^{-9}	8.024×10^{-9}
NH ₂ OH	2.862×10^{-9}	4.322×10^{-6}
HNCO	8.720×10^{-10}	1.097×10^{-9}
CH ₃ CHO	3.539×10^{-9}	2.133×10^{-9}
CH ₃ OCH ₃	1.710×10^{-13}	3.966×10^{-14}
HCOOH	3.622×10^{-10}	1.061×10^{-10}
HCOOCH ₃	2.869×10^{-13}	3.789×10^{-14}
CH ₃ COOH	8.920×10^{-24}	6.340×10^{-21}
C ₂ H ₅ OH	2.455×10^{-12}	1.251×10^{-13}

NOTE—These initial abundances are the same as [Notsu et al. \(2021\)](#) used in their chemical modeling.

As [Walsh et al. \(2015\)](#) and [Notsu et al. \(2021\)](#) adopted, the values of volatile elemental abundances for He, O, C, N, and S are respectively 9.75×10^{-2} , 3.20×10^{-4} , 1.40×10^{-4} , 7.50×10^{-5} , and 8.00×10^{-8} relative to total hydrogen nuclei density. For other elements, we use the low-metallicity elemental abundances from [Graedel et al. \(1982\)](#). In the reset scenario, we use the above elemental abundances as initial abundances of our disk chemical calculations, except hydrogen. We assume that the abundances for H₂ and H are respectively 5.0×10^{-1} and 5.0×10^{-5} .

Table 2 shows the gas and ice fractional molecular abundances with respect to total hydrogen nuclei density which are used as molecular initial abundances in the inheritance scenario. In this Table 2, we include dominant species and molecules which are important in disk chemical evolution. We adopt the same molecular abundances as [Notsu et al. \(2021\)](#) used for the initial abundances in their chemical modeling. Previous chemical calculations (e.g., [Walsh et al. 2015](#); [Eistrup et al. 2016, 2018](#); [Drozdovskaya et al. 2016](#)) adopted a similar water-rich molecular abundances as initial conditions.

3. RESULTS

In Sections 3.1-3.2, we investigate the results for our standard model (assuming molecular initial abundances and $\xi_{\text{CR}}(r) = 1.0 \times 10^{-17} [\text{s}^{-1}]$), and describe the effects of a disk shadow on the radial molecular abundance distributions. In Appendix A, we also study the disk chemical structures for different disk ionization rates and for atomic initial abundances (see also Section 3.3). In addition, in Sections 3.1-3.2 we show the chemical abundance distributions at $t = 10^6$ years, which is the typical age of Class II disks and consistent with previous studies (e.g., [Eistrup et al. 2016](#)). In Appendix B, we also investigate the time evolution of radial molecular abundance distributions (see also Section 3.4).

3.1. Dominant carbon-, oxygen-, and nitrogen-carriers around the current orbit of Jupiter

In this Section, we show the composition of the dominant carbon-, oxygen-, and nitrogen-carriers around the current orbit of Jupiter. Figure 2 shows pie charts of the percentage contributions of the dominant carbon-, oxygen-, and nitrogen-bearing molecules to the total elemental abundances ($= 1.4 \times 10^{-4}$ for carbon, $= 3.2 \times 10^{-4}$ for oxygen, $= 7.5 \times 10^{-5}$ for nitrogen) at $r = 5.3$ au (around the current orbit of Jupiter) and $t = 10^6$ years, in the non-shadowed disk ($f = 1.0$) and a shadowed disk ($f = 0.03$). These results are from the

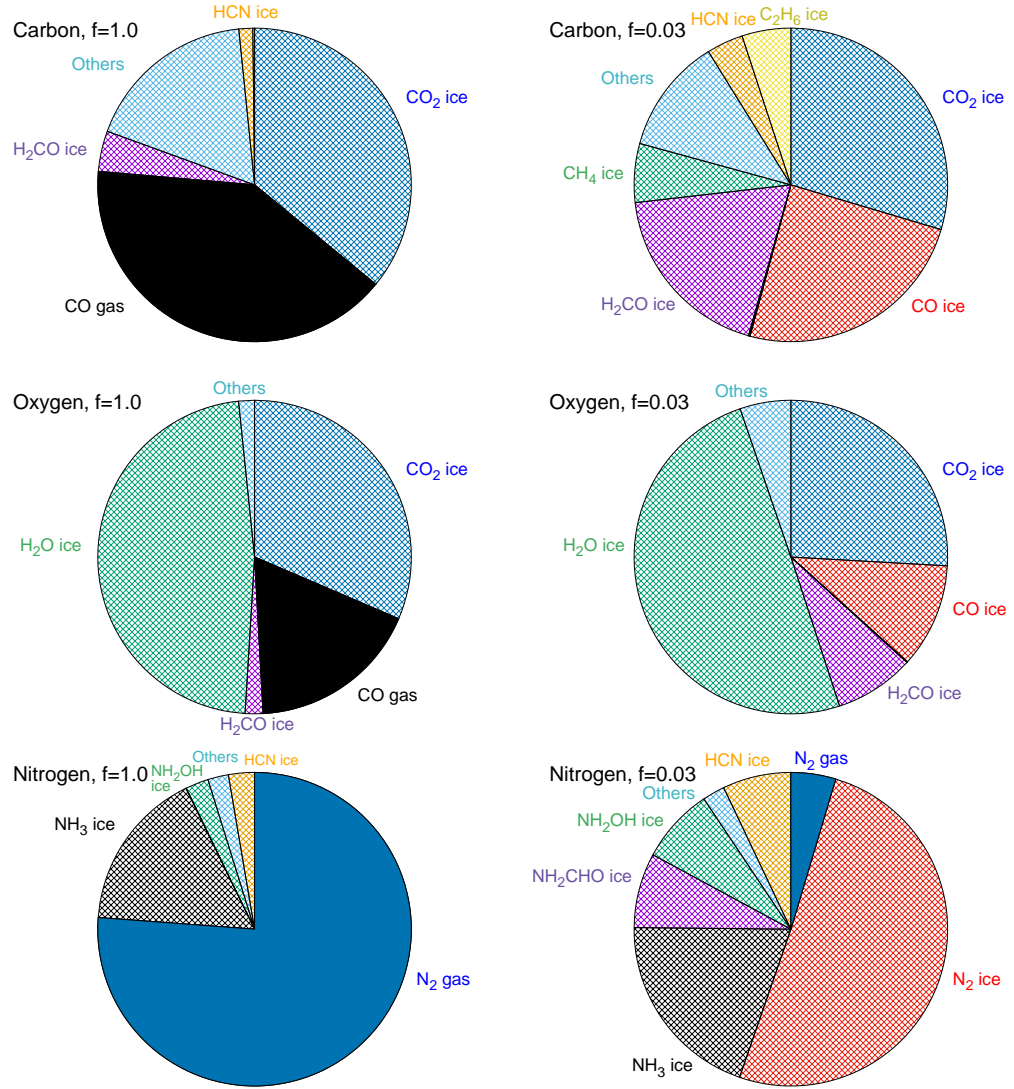


Figure 2. Pie charts of the percentage contributions of the dominant carbon-bearing molecules to the total elemental carbon abundance ($= 1.4 \times 10^{-4}$, top panels), the dominant oxygen-bearing molecules to the total elemental oxygen abundance ($= 3.2 \times 10^{-4}$, middle panels), and the dominant nitrogen-bearing molecules to the total elemental nitrogen abundance ($= 7.5 \times 10^{-5}$, bottom panels), at $r = 5.3$ au (around the current orbit of Jupiter) and $t = 10^6$ years. The left panels show the contributions for the disk midplane with the monotonically decreasing density and temperature profile ($f = 1.0$), whereas the right panel shows the contributions for the shadowed disk midplane ($f = 0.03$). These panels show the results for molecular initial abundances (the “inheritance” scenario) and $\xi_{\text{CR}}(r) = 1.0 \times 10^{-17} \text{ [s}^{-1}\text{]}$. The filled and hatched slices are respectively the contributions of gaseous and icy molecules. [Top panels]: The dark blue, red, black, purple, green, orange, yellow, and light blue slices are respectively the contributions of CO₂ ice, CO ice, CO gas, H₂CO ice, CH₄ ice, HCN ice, C₂H₆ ice, and other molecules (such as NH₂CHO ice and CH₃OH ice for $f = 0.03$, and CH₃CCH ice, CH₂CCH₂ ice, and CH₃CHCH₂ ice for $f = 1.0$). [Middle panels]: The dark blue, red, black, purple, green, and light blue slices are respectively the contributions of CO₂ ice, CO ice, CO gas, H₂CO ice, H₂O ice, and other molecules (such as NH₂CHO ice and CH₃OH ice). [Bottom panels]: The dark blue, red, black, purple, green, orange, and light blue slices are respectively the contributions of N₂ gas, N₂ ice, NH₃ ice, NH₂CHO ice, NH₂OH ice, HCN ice, and other molecules (such as HC₃N ice).

model in which we assume molecular initial abundances and a high ionisation rate (see Figures 3-5 in Section 3.2).

In the non-shadowed disk, the dominant carbon carriers at $r = 5.3$ au are CO₂ ice ($\sim 36\%$) and CO gas ($\sim 40\%$). In the shadowed disk, CO freezes out onto the dust grain surface, and the amounts of CO₂ ice ($\sim 30\%$), CO ice ($\sim 25\%$), and ices of unsaturated hydrocarbon molecules (such as C₃H₄) decrease, whereas those of H₂CO ice ($\sim 19\%$), CH₄ ice ($\sim 6\%$), C₂H₆ ice ($\sim 5\%$), HCN ice ($\sim 4\%$), NH₂CHO ice ($\sim 4\%$), and CH₃OH ice ($\sim 3\%$) increase. The enhanced abundances of these organic molecules in the shadowed disks are owing to the reaction pathways in which the sequential hydrogenation of CO on the dust grain surfaces and cosmic-ray-induced photodissociation of CH₃OH are the key reactions, as we explain in Sections 3.2.2 and 3.2.3.

In the non-shadowed disk, the dominant oxygen carriers at $r = 5.3$ au are H₂O ice ($\sim 47\%$), CO₂ ice ($\sim 31\%$) and CO gas ($\sim 18\%$). In the shadowed disk, the amounts of CO₂ ice ($\sim 26\%$) and CO ice ($\sim 11\%$) decrease, whereas that of H₂O ice is similar ($\sim 50\%$), and that of H₂CO ice ($\sim 8\%$) increases.

In the non-shadowed disk, the dominant nitrogen carriers at $r = 5.3$ au are N₂ gas ($\sim 76\%$) and NH₃ ice ($\sim 17\%$). In the shadowed disk, N₂ mostly freezes-out onto the dust grain surface, and the amount of N₂ gas ($\sim 5\%$) decreases, whereas that of NH₃ ice is almost similar ($\sim 20\%$), and those of N₂ ice ($\sim 51\%$) and other nitrogen-bearing molecules such as NH₂OH, NH₂CHO, and HCN ices ($\sim 7 - 8\%$ each) increase. The enhanced abundances of NH₂OH, NH₂CHO, and HCN in the shadowed disks are due to hydrogenation reactions on the dust grain surfaces (see Section 3.2.3).

According to these results, in shadowed disks the dust grains at around the current orbit of Jupiter ($r \sim 5.3$ au) are expected to have significant amounts of saturated hydrocarbon ices such as CH₄ and C₂H₆, ices of organic molecules such as H₂CO, NH₂CHO, and CH₃OH, in addition to H₂O, CO, CO₂, NH₃, N₂, HCN, and NH₂OH ices, compared with those in the non-shadowed disks (mostly ices of H₂O, CO₂, NH₃, and unsaturated hydrocarbon molecules). These abundant saturated hydrocarbons and various organic molecules such as H₂CO, NH₂CHO, and CH₃OH were not reported by Ohno & Ueda (2021), since they approximated various organic molecules by considering C₂H₆ alone. In addition, our results provide intriguing implications for

the compositions of small bodies (such as comets and asteroids) formed at around the current orbit of Jupiter, as we discuss in Section 4.2.

3.2. Radial molecular abundance distributions for our standard model

In this Section, we describe the effects of disk shadowing on the radial molecular abundance distributions. The radial profiles of fractional abundances with respect to total hydrogen nuclei densities n_X/n_H at $t = 10^6$ years for dominant carbon-, oxygen-, nitrogen-bearing molecules are shown in Figures 3-5 in Sections 3.2.1-3.2.3, with separate panels for each molecule, for different values of the parameter f ($=1.0, 0.3, 0.03, \text{ and } 0.003$), respectively. In Figures 6-8 in Section 3.2.4, the radial fractional abundance distributions at $t = 10^6$ years of other major carbon-, nitrogen-, and oxygen-bearing molecules, mainly complex organic molecules, are shown. In Figure 9 in Section 3.2.5, the radial profiles of fractional abundances with respect to total hydrogen nuclei densities at $t=10^6$ years for sums of larger (complex) organic molecules are shown. We show this to demonstrate the efficiency of conversion from more simple to more complex molecules for different dust depletion factors. The panels in these Figures 3-9 show the results for the radially constant cosmic-ray ionization rate of $\xi_{CR}(r) = 1.0 \times 10^{-17} [\text{s}^{-1}]$ with assuming molecular initial abundances (the ‘‘inheritance’’ scenario).

Since previous studies (e.g., Eistrup et al. 2016, 2018) have discussed the chemical structure of the non-shadowed disk ($f = 1.0$) in detail, in this paper we mainly focus on the effects of shadowing on disk chemical structures. We note that the results of our calculations for the non-shadowed disk are largely consistent with those in Eistrup et al. (2016, 2018) with some exceptions, such as HCN (see Section 3.2.3 of this paper).

3.2.1. H₂O, CO, CO₂, and O₂

Figure 3 shows the radial profiles of fractional abundances for dominant oxygen-bearing molecules; H₂O (water), CO (carbon monoxide), CO₂ (carbon dioxide), and O₂ (molecular oxygen). The water snowline position (~ 1.3 au, $T(r) \sim 140$ K) and the H₂O gas abundances ($\sim 2 \times 10^{-4}$) within the water snowline do not change for various values of f , since the disk mid-plane temperature is significantly changed only beyond the water snowline. We note that the gas abundances of other molecules are also unchanged within the water snowline.

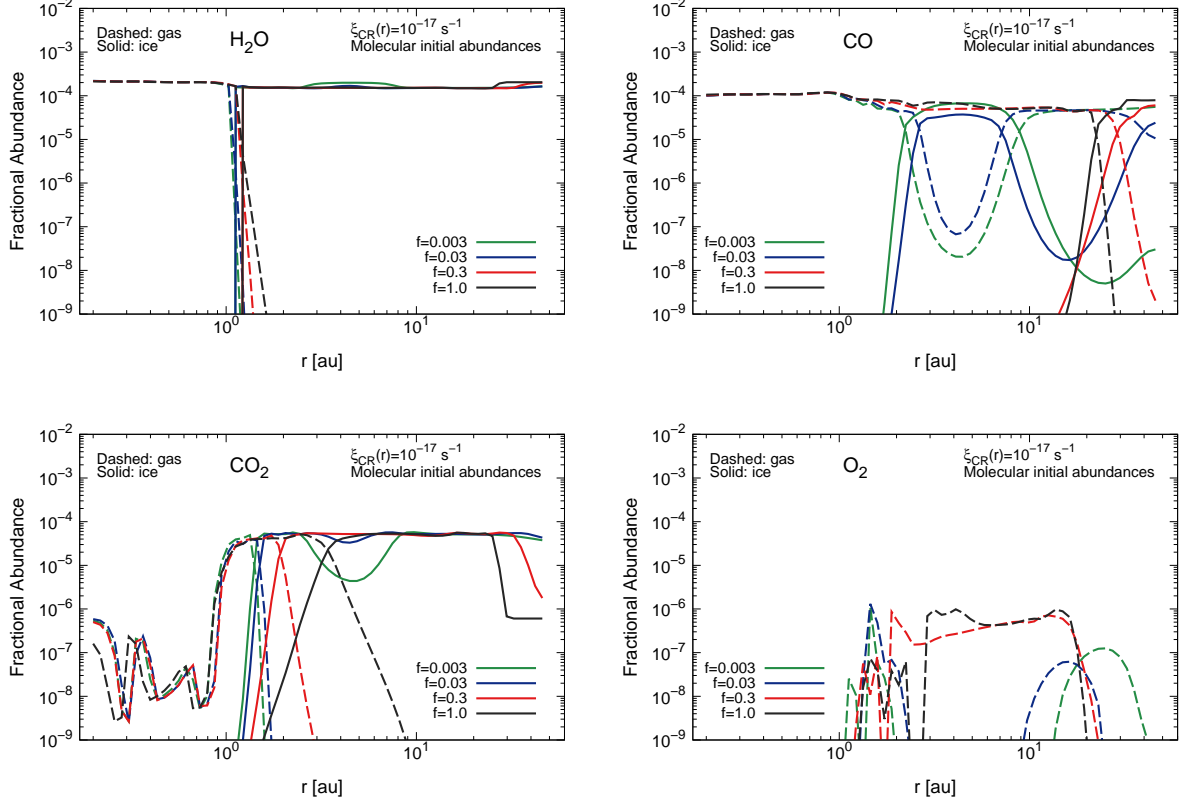
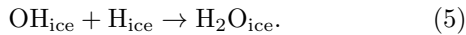


Figure 3. The radial profiles of fractional abundances with respect to total hydrogen nuclei densities at $t=10^6$ years for H_2O ($n_{\text{H}_2\text{O}}/n_{\text{H}}$, top left panel), CO ($n_{\text{CO}}/n_{\text{H}}$, top right panel), CO_2 ($n_{\text{CO}_2}/n_{\text{H}}$, bottom left panel), and O_2 ($n_{\text{O}_2}/n_{\text{H}}$, bottom right panel). These panels show the results for the radially constant cosmic-ray ionization rate $\xi_{\text{CR}}(r) = 1.0 \times 10^{-17} [\text{s}^{-1}]$ and molecular initial abundances (the “inheritance” scenario). The dashed and solid lines show the profiles for gaseous and icy molecules, respectively. The black, red, blue, and green lines show the profiles for different values of the parameter f ($=1.0, 0.3, 0.03, \text{ and } 0.003$), respectively.

Outside the water snowline, H atoms are supplied onto the dust grain surface from the gas or produced in situ within the grain mantles. We note that in the gas-phase, H atoms are mainly produced by cosmic-ray-induced photodissociation of H_2 . Since the fractional abundances of H_2 with respect to total H nuclei ($\sim 5 \times 10^{-1}$) are much larger than those of other molecules, the gas-phase production is dominant. Thus, if we conduct disk chemical modeling with atomic initial abundances (see Appendix A), H_2O ice is efficiently formed outside the water snowline via the following reaction (Eistrup et al. 2016),



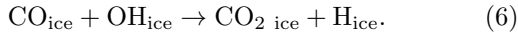
However, because we have adopted abundant initial water ice abundances ($= 1.984 \times 10^{-4}$, see Table 1), further water ice formation in the outer disk midplane

does not proceed efficiently. Thus, the H_2O ice abundances beyond the water snowline are relatively constant ($\sim (1-2) \times 10^{-4}$) for various values of f . We note that the H_2O ice abundances increase (from $\sim 1.5 \times 10^{-4}$ to $\sim 2 \times 10^{-4}$) in the coldest regions with $T(r) \lesssim 20$ K (at $r \sim 3-8$ au for $f = 0.003$ and at $r \gtrsim 25$ au for $f = 1.0$), where the formation of CO_2 ice does not proceed efficiently (see below).

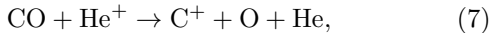
In the non-shadowed disk ($f = 1.0$), the CO snowline position is $r \sim 22$ au ($T(r) \sim 25$ K), and CO gas abundances inside the water snowline are 10^{-4} . In addition, in the non-shadowed disk CO gas abundances between the H_2O and CO snowlines are $\sim (4-8) \times 10^{-5}$.

As introduced later, the chemical conversion of CO

plays vital roles in producing other carbon-bearing molecules. CO molecules accreting onto the dust grain surfaces can react with OH radicals produced on the ice by cosmic-ray-induced photodissociation of H₂O ice (e.g., Drozdovskaya et al. 2016; Eistrup et al. 2016, 2018; Schwarz et al. 2018, 2019). This produces CO₂ ice via the following grain-surface reaction,



In addition, for the ISM level ionization rate ($\xi_{\text{CR}}(r) = 10^{-17} [\text{s}^{-1}]$), the following destruction pathway of gas-phase CO by He⁺ is also efficient,



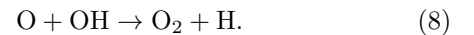
which leads to the formation of CH₄, C₂H₆, and other hydrocarbons (e.g., Aikawa et al. 1999; Furuya & Aikawa 2014; Eistrup et al. 2016, 2018; Yu et al. 2016; Bosman et al. 2018, see also Sections 3.2.2 and 3.2.4). We note that He⁺ is produced by the direct cosmic-ray ionisation of He. Moreover, the sequential hydrogenation of CO on the dust grain surfaces leads to the formation of H₂CO and CH₃OH ices (e.g., Watanabe & Kouchi 2002; Drozdovskaya et al. 2014; Bosman et al. 2018, see also Section 3.2.2 and Appendix A.2). Several studies have suggested that the above chemical processes (partly) explain the depletion of CO in the Class II disks reported by recent observations with ALMA (see e.g., Nomura et al. 2016, 2021; Schwarz et al. 2016; Krijt et al. 2018, 2020; Bergner et al. 2020; Zhang et al. 2020, 2021).

In the shadowed disk ($f \leq 0.03$), CO freezes-out onto dust grains at around the current orbit of Jupiter ($r \sim 3 - 8$ au, $T(r) \lesssim 25$ K), and CO ice abundances are $\sim (3 - 6) \times 10^{-5}$. In addition, CO returns to gas phase at $r > 8$ au. At $r > 20$ au, CO (re-)freezes out onto dust grains, and the adsorption front moves outward with decreasing f , since the values of $T(r)$ at $r > 20$ au increase ($\lesssim 35$ K at the maximum) with decreasing f (see also Section 2.1). This CO abundance profile is consistent with the results reported in Ohno & Ueda (2021). We suggest that reducing the dust surface density beyond the water snowline allows the reprocessed stellar radiation to enter the outer disk midplane from the disk upper layers, and that the penetration of such radiation causes the temperature rise in the outer disk ($r > 20$ au).

In the non-shadowed disk ($f = 1.0$), the CO₂ snowline position is $r \sim 3.3$ au ($T(r) \sim 75$ K). CO₂ ice abundances are $\sim 5 \times 10^{-5}$ between the CO₂ and the CO snowlines, and decrease ($< 10^{-6}$) beyond the CO snowline. The CO₂ snowline position moves inward with

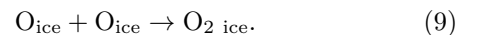
decreasing f . In the shadowed disk ($f \leq 0.03$), CO₂ ice abundances decrease at $r \sim 3 - 8$ au (from $\sim 5 \times 10^{-5}$ to $< 10^{-5}$) with decreasing f , whereas H₂O ice abundances at such radii slightly increase (from $\sim 1.5 \times 10^{-4}$ to $\sim 2 \times 10^{-4}$). Eistrup et al. (2016) discussed that at coldest conditions ($T(r) \lesssim 20$ K), the formation of H₂O ice (Reaction 5) is faster than that of CO₂ ice (Reaction 6). This is because at the coldest conditions ($T(r) \lesssim 20$ K) the mobility of H is higher than those of CO and OH, and because the adsorption rate of atomic hydrogen onto dust grains at $T(r) \lesssim 20$ K becomes larger than that at $T(r) > 20$ K ($E_{\text{des}}(\text{H}) = 650$ K).

In our standard disk model, O₂ abundances are much smaller ($\lesssim 10^{-6}$ for gas and $\lesssim 10^{-9}$ for ice) than those of H₂O, CO, and CO₂. O₂ is formed in the gas-phase via the following reaction (Walsh et al. 2015; Eistrup et al. 2016; Notsu et al. 2021),



Since O₂ is very volatile (the binding energy $E_{\text{des}}(\text{O}_2) = 898$ K, Noble et al. 2012), it remains in the gas-phase at $r \lesssim 20$ au in the non-shadowed disk ($f = 1.0$). The O₂ gas abundances between the water and O₂ snowlines are $\sim 10^{-7} - 10^{-6}$.

In the shadowed disk ($f \leq 0.03$), O₂ freezes-out onto dust grains at $r \sim 2 - 10$ au, and returns to the gas phase at $r > 10$ au. Outside the O₂ snowline, O₂ ice is formed via the following grain-surface reaction (Taquet et al. 2016; Eistrup & Walsh 2019),



In our standard disk model, the initial atomic oxygen is zero (see Table 2). In addition, gas-phase production route of atomic oxygen from CO by Reaction 7 is not efficient outside the O₂ snowline since the binding energies of CO and O₂ are almost similar (see Table 1). Thus, in our standard disk model, O₂ ice abundances are low ($\ll 10^{-9}$) both in the shadowed and non-shadowed disks.

We note that our calculations also yield higher O₂ ice abundances ($\sim 10^{-5} - 10^{-4}$) for atomic initial abundances and low ionisation rates. Such larger abundances are consistent with the measured cometary abundances (Bieler et al. 2015; Rubin et al. 2015b, see also Section 4.2 of this paper). Moreover, we find that in the shadowed disk such an O₂ abundant region is located in the inner region ($r \sim 2 - 10$ au) compared with that in the non-shadowed disk ($r \gtrsim 20$ au), as detailed in Section 4.2 and Appendix A.1.

3.2.2. Other dominant carbon-bearing molecules

Figure 4 shows the radial profiles of fractional abundances for other dominant carbon-bearing molecules (CH_4 , C_2H_6 , H_2CO , and CH_3OH). We note that CH_4 (methane) and C_2H_6 (ethane) are dominant acyclic saturated hydrocarbon molecules (alkanes). In the non-shadowed disk ($f = 1.0$), the CH_4 snowline position is $r \sim 15$ au ($T(r) \sim 38$ K), and the CH_4 gas abundances between the CO_2 and CH_4 snowlines are $\sim 10^{-7}$. These values are much smaller than those in the disk with a lower ionisation rate ($=10^{-18}$ [s $^{-1}$], see Appendix A) and that for the initial CH_4 gas abundance ($= 1.120 \times 10^{-6}$). Outside the CH_4 snowline, CH_4 ice abundances are slightly enhanced ($\sim 10^{-5}$) compared with the initial CH_4 ice abundances ($= 7.384 \times 10^{-6}$).

Here we describe the dominant formation and destruction routes of CH_4 both in the gas-phase and icy-phase. The destruction of gas-phase CO by He^+ (see Section 3.2.1) produces C^+ , and a sequence of reactions with e.g., H_2 transform C^+ to e.g., $\text{CH}_2^+/\text{CH}_3^+/\text{CH}_5^+$, which lead to CH_4 gas and ice (e.g., Aikawa et al. 1999; Furuya & Aikawa 2014; Bosman et al. 2018, see Section 3.2.1). In addition, Bosman et al. (2018) and Eistrup et al. (2018) discussed that CH_4 ice is also produced both inside/outside the CO snowline through the hydrogenation of CH_3 ice, which is formed by cosmic-ray-induced photodissociation of CH_3OH (see also below). Inside the CH_4 snowline, CH_4 gas is destroyed by cosmic-ray-induced photodissociation and ion-molecule reactions (such as $\text{CH}_4 + \text{C}^+$), and the carbon is thus converted from CH_4 gas to CO_2 , H_2CO , and hydrocarbons such as e.g., C_2H_2 , C_2H_4 , and C_3H_4 (Aikawa et al. 1999; Eistrup et al. 2016, 2018; Yu et al. 2016, see also Section 3.2.4).

The CH_4 snowline positions moves inward with decreasing f . In the shadowed disk ($f \leq 0.03$), CH_4 snowline positions are $r \lesssim 2$ au, and CH_4 ice abundances at $r \sim 2 - 15$ au are around $\sim 10^{-5}$. This result indicates that the CH_4 ice abundances are comparable in both CO sublimation and frozen regions. Thus, we interpret that the above reaction pathway starting from cosmic-ray-induced photodissociation of CH_3OH is efficient for CH_4 ice formation in this region.

In the non-shadowed disk ($f = 1.0$), the C_2H_6 snowline position is $r \sim 3.2$ au, which is similar to that for CO_2 ($E_{\text{des}}(\text{CO}_2) = 2267$ K, $E_{\text{des}}(\text{C}_2\text{H}_6) = 2320$ K). The C_2H_6 ice abundances outside its snowline increase with increasing r . The ice abundances are $\sim (3 - 6) \times 10^{-6}$

outside the CH_4 snowline, which is larger than the initial ice abundance ($= 2.417 \times 10^{-6}$).

Previous modeling studies suggested that unsaturated hydrocarbon molecules (such as C_2H_2 , C_3H_2 , C_3H_4) are efficiently produced with the chemical reaction pathways starting from $\text{CH}_4 + \text{C}^+$, where C^+ is formed by $\text{CO} + \text{He}^+$ (e.g., Aikawa et al. 1999; Furuya & Aikawa 2014; Eistrup et al. 2016, 2018; Yu et al. 2016; Bosman et al. 2018, see Section 3.2.1). In addition, such unsaturated hydrocarbon molecules are also supplied by the cosmic-ray-induced photodissociation of CH_4 and subsequent gas-phase combination reactions of CH_x radicals (e.g., Aikawa et al. 1999; Eistrup et al. 2016; Yu et al. 2016). These reaction pathways are efficient in the inner warm disk, at least within the CH_4 snowline (see also Section 3.2.4). The saturated hydrocarbons including C_2H_6 are formed on the grain-surfaces by the hydrogenation of such unsaturated hydrocarbon ices (e.g., Aikawa et al. 1999; Bosman et al. 2018). In addition, Bosman et al. (2018) and Eistrup et al. (2018) discussed that C_2H_6 ice is also produced both inside/outside the CO snowline by $\text{CH}_{3\text{ice}} + \text{CH}_{3\text{ice}}$, where CH_3 ice is formed by cosmic-ray-induced photodissociation of CH_3OH ice. Thus, we conclude that grain-surface reactions are needed to form icy-phase saturated hydrocarbon molecules, including C_2H_6 .

In the shadowed disk ($f \leq 0.03$), C_2H_6 snowline positions are $r < 2$ au, and C_2H_6 ice abundances at $r \sim 2 - 10$ au significantly increase ($\sim 5 \times 10^{-6}$) compared with the values in the non-shadowed disk. We interpret that the reaction pathway starting from CH_3OH ice destruction becomes more important at these radii of the shadowed disk, since the abundances of unsaturated hydrocarbon ices (such as C_2H_2 , C_3H_2 , C_3H_4) decrease in the shadowed disk (see Section 3.2.4 for details).

In the non-shadowed disk ($f = 1.0$), the H_2CO (formaldehyde) and CH_3OH (methanol) snowline positions are $r \sim 1.8$ au ($T(r) \sim 100$ K) and ~ 1.5 au ($T(r) \sim 120$ K), respectively, and they are just outside the water snowline ($r = 1.3$ au). The H_2CO and CH_3OH ice abundances outside their snowlines increase with increasing r . The H_2CO ice abundances between the H_2CO and CO snowlines are $\sim 8 \times 10^{-6}$ at most, which is similar to the initial H_2CO ice abundance ($= 8.437 \times 10^{-6}$). The CH_3OH ice abundances between the CH_3OH and CO snowlines are $\sim 2 \times 10^{-7}$, which is smaller than the initial CH_3OH ice abundance ($= 6.027 \times 10^{-7}$). We suggest that the differences in the CH_3OH and H_2CO abundances with respect to the

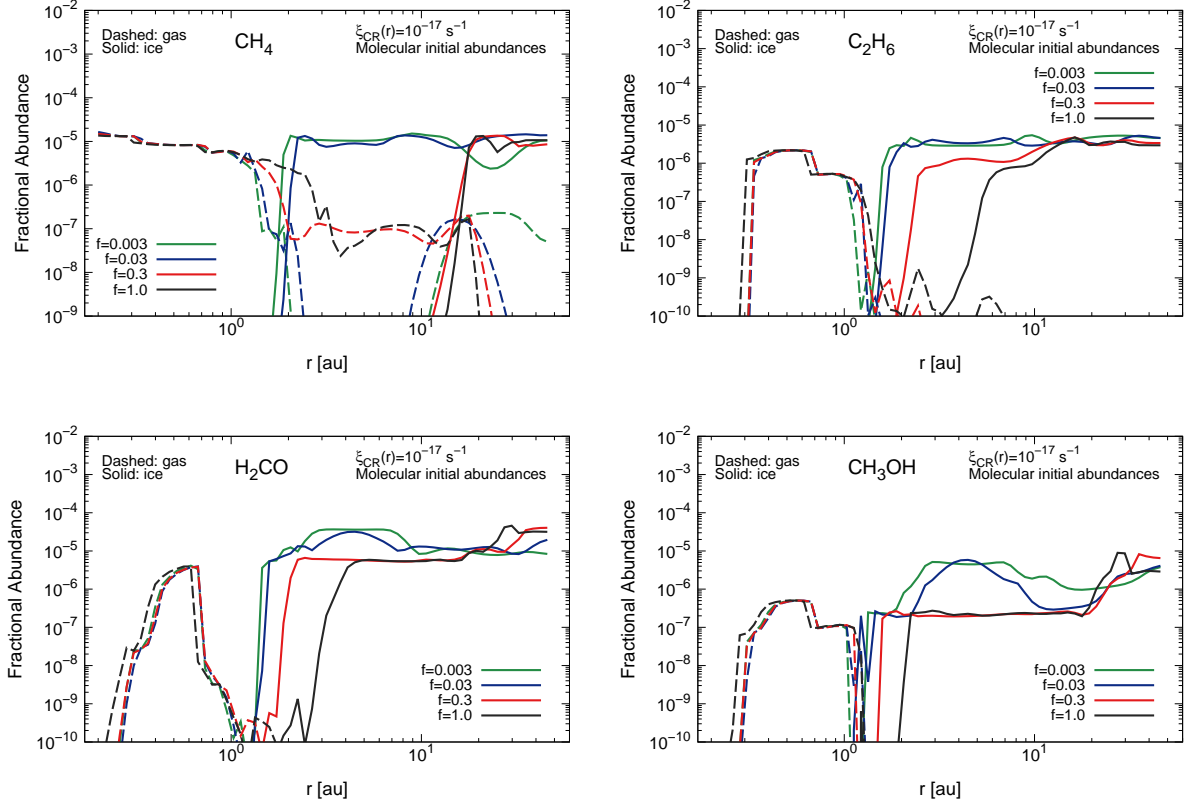
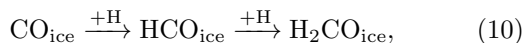


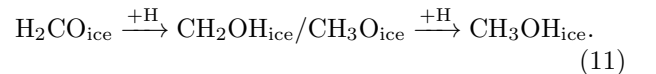
Figure 4. Same as Figure 3, but for CH_4 ($n_{\text{CH}_4}/n_{\text{H}}$, top left panel), C_2H_6 ($n_{\text{C}_2\text{H}_6}/n_{\text{H}}$, top right panel), H_2CO ($n_{\text{H}_2\text{CO}}/n_{\text{H}}$, bottom left panel), and CH_3OH ($n_{\text{CH}_3\text{OH}}/n_{\text{H}}$, bottom right panel).

initial abundances inside the CO snowline are also related to whether or not gas-phase formation pathways are present (e.g., Fockenberg & Preses 2002; Atkinson et al. 2006; Loomis et al. 2015; Walsh et al. 2016; Pegues et al. 2020). Both H_2CO and CH_3OH ice abundances increase outside the CO snowline ($\sim (2 - 5) \times 10^{-5}$ for H_2CO ice and $\sim (2 - 9) \times 10^{-6}$ for CH_3OH ice).

The freeze-out of CO onto dust grains plays a central role in producing organic molecules, such as H_2CO and CH_3OH . According to previous studies (e.g., Tielens & Hagen 1982; Watanabe & Kouchi 2002; Cuppen et al. 2009; Fuchs et al. 2009; Drozdovskaya et al. 2014; Furuya & Aikawa 2014; Walsh et al. 2014, 2016; Chuang et al. 2016; Bosman et al. 2018; Aikawa et al. 2020, see also Appendix A.2), the following sequential hydrogenation of CO on the dust grain surfaces leads to the formation of H_2CO and CH_3OH ices,



and



This grain-surface reaction pathway produces a large amount of H_2CO and CH_3OH ices in the cold regions where CO freezes-out onto dust grains. The cosmic-ray-induced photodissociation of CH_3OH ice produces many radicals such as CH_3O , CH_3 , CH_2OH ices, and radical-radical reactions on the warmer grains also create more complex organic molecules, in addition to atom addition reactions on the colder grains (Walsh et al. 2014). We note that our chemical reaction network includes both hydrogenation and abstraction pathways along the methanol formation route (Chuang et al. 2016), and CH_2OH ice is the dominant methanol H-atom abstraction product.

In the shadowed disk ($f \leq 0.03$), the H_2CO and CH_3OH ice abundances at $r \sim 2 - 10$ au significantly increase

($\sim (1 - 5) \times 10^{-5}$ for H_2CO ice and $\sim (2 - 9) \times 10^{-6}$ for CH_3OH ice) compared with the values in the non-shadowed disk, since the temperature is low ($T(r) \lesssim 30$ K) and the sequential hydrogenation of CO ice (Reactions 10 and 11) proceeds efficiently. In contrast, their ice abundances at $r \gtrsim 20$ au become a bit smaller ($\sim 10^{-5}$ for H_2CO ice and $\sim (1 - 3) \times 10^{-6}$ for CH_3OH ice), since the CO adsorption front moves outward with decreasing f .

3.2.3. Dominant nitrogen-bearing molecules

Figure 5 shows the radial profiles of fractional abundances for dominant nitrogen-bearing molecules (N_2 , NH_3 , HCN , and NH_2CHO). In the non-shadowed disk ($f = 1.0$), the N_2 (molecular nitrogen) snowline position is $r \sim 24$ au ($T(r) \sim 23$ K), which is slightly outside the CO snowline. For the atomic initial abundances, atomic N quickly forms N_2 gas and it freezes out onto dust grains outside its snowline (Schwarz & Bergin 2014; Eistrup et al. 2016). In addition, for the molecular initial abundances, the initial atomic N abundance ($= 2.1 \times 10^{-5}$, see Table 1) is similar to the initial N_2 gas + ice abundance ($= 1.5 \times 10^{-5}$, see Table 1), and this atomic N is also quickly converted to N_2 in the disk. Thus, the N_2 gas + ice abundances are relatively constant ($\sim (2 - 3) \times 10^{-5}$) throughout the disk for various values of f and various initial conditions (see also Appendix A.3).

In the shadowed disk ($f \leq 0.03$), like CO, N_2 freezes-out onto dust grains at around the current orbit of Jupiter ($r \sim 3 - 8$ au), and N_2 ice abundances are $\sim 2 \times 10^{-5}$. In addition, N_2 returns to the gas phase at $r > 8$ au. At $r > 20$ au, N_2 (re-)freezes out onto dust grains, and the adsorption front moves outward with decreasing f , since $T(r)$ at $r > 20$ au increases ($\lesssim 35$ K at the maximum) with decreasing f (see also Section 2.1). This N_2 abundance profile is consistent with the results reported in Ohno & Ueda (2021).

In the non-shadowed disk ($f = 1.0$), the NH_3 (ammonia) snowline position is $r \sim 2.3$ au, which is slightly outside the water snowline ($r = 1.3$ au). NH_3 ice abundances just outside the NH_3 snowline ($r \sim 2 - 4$ au) are $\ll 10^{-6}$, and those at $r > 5$ au are $\sim 1 \times 10^{-5}$, which is similar to the initial NH_3 ice abundance ($= 1.327 \times 10^{-5}$). We suggest that on the warm grain surfaces at $r \sim 2 - 4$ au, NH_3 ice is converted to NH_2CHO ice via the following grain-surface reaction route (Jones et al. 2011; Walsh et al. 2014; López-Sepulcre et al. 2015),



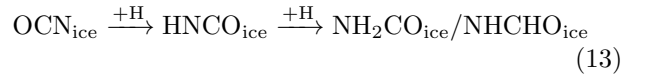
where NH_2 ice is formed by the cosmic-ray-induced photodissociation of NH_3 ice.

In the shadowed disk ($f \leq 0.03$), NH_3 snowline positions are $r \lesssim 2$ au. NH_3 ice abundances at $r \sim 2 - 5$ au are significantly enhanced, since the disk temperature decreases and the above destruction route of NH_3 ice (see Reaction 12) becomes inefficient.

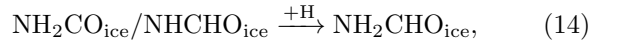
Formamide (NH_2CHO) has been proposed as a key precursor of various (pre)metabolic and (pre)genetic molecules such as pyruvic acid and adenine (Saladino et al. 2012). Gas-phase NH_2CHO has been detected in pre-stellar cores and protostar envelopes (e.g., Kahane et al. 2013; López-Sepulcre et al. 2015; Okoda et al. 2021) and comets (e.g., Bockelée-Morvan et al. 2000), but has not yet been detected in Class II disks. The NH_2CHO snowline position ($r \sim 1.2$ au, $T(r) \sim 150$ K) is slightly inside the water snowline ($E_{\text{des}}(\text{NH}_2\text{CHO}) = 5560$ K, $E_{\text{des}}(\text{H}_2\text{O}) = 4880$ K), thus the NH_2CHO snowline position does not move in our chemical modeling.

In the non-shadowed disk ($f = 1.0$), the NH_2CHO ice abundances are $\gtrsim 10^{-6}$ in the outer cold disk (around the CO/ N_2 snowlines, $r \sim 14 - 33$ au), and $< 10^{-7}$ at $r \lesssim 10$ au. In addition, NH_2CHO is efficiently formed ($\gtrsim 10^{-6}$) just outside its snowline ($r \sim 1.2 - 4$ au). We interpret that just outside its snowline, the above radical-radical formation route on the warm dust grains is efficient (see Reaction 12).

In the shadowed disk ($f \leq 0.03$), NH_2CHO ice abundances at around the current orbit of Jupiter ($r \sim 3 - 8$ au) are enhanced ($\gtrsim 10^{-6}$). We propose that the following hydrogenation routes become efficient in this region. Garrod et al. (2008), Walsh et al. (2014), and López-Sepulcre et al. (2015) discussed that grain-surface NH_2CHO can form via the atom addition reactions in the cold region, such as the following reaction routes,



and



where OCN_{ice} is formed via the grain-surface reactions ($\text{CN}_{\text{ice}} + \text{O}_{\text{ice}}$ and $\text{ON}_{\text{ice}} + \text{C}_{\text{ice}}$) or gas-phase radical-radical reactions. We note that our chemical reaction network includes a competing hydrogenation abstraction pathway during hydrogenation from HNCO to NH_2CHO , on the basis of the experimental results in Noble et al. (2015).

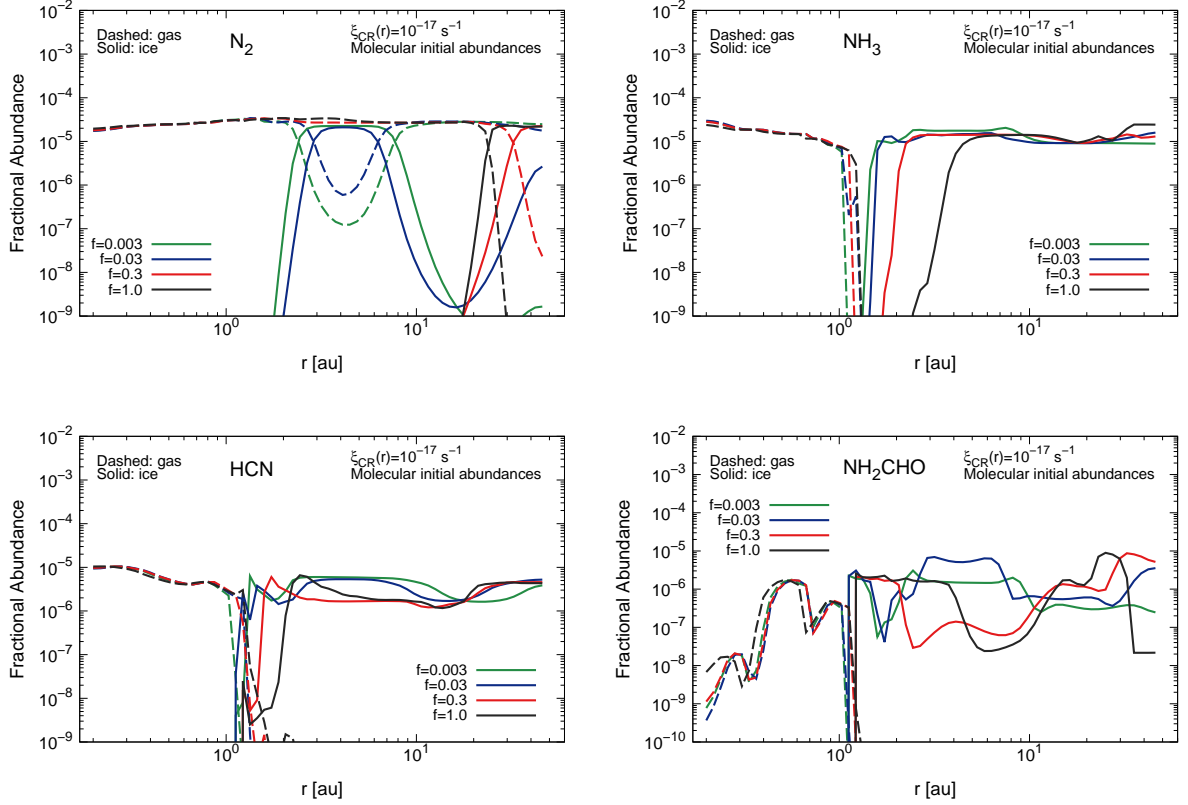


Figure 5. Same as Figure 3, but for N_2 (n_{N_2}/n_H , top left panel), NH_3 (n_{NH_3}/n_H , top right panel), HCN (n_{HCN}/n_H , bottom left panel), and NH_2CHO (n_{NH_2CHO}/n_H , bottom right panel).

HCN (hydrogen cyanide) and CN (cyanide) are the simplest molecules containing both C and N atoms, and reactions including HCN lead to the formation of more complex cyanides (such as CH_3CN and aminoacetonitrile H_2NCH_2CN) (Öberg et al. 2011; Noble et al. 2013). In the non-shadowed disk ($f = 1.0$), the HCN snowline position is $r \sim 1.5$ au ($T(r) \sim 120$ K), which is just outside the water snowline ($r = 1.3$ au). HCN ice abundances are $\sim (1 - 3) \times 10^{-6}$ at $r \sim 3 - 20$ au and $\sim 4 \times 10^{-6}$ at $r \gtrsim 20$ au, which are slightly smaller/larger than the initial HCN ice abundance ($= 2.772 \times 10^{-6}$). Eistrup et al. (2016) showed much lower HCN ice abundances ($\ll 10^{-7}$ outside the HCN snowline) for their model calculations with molecular initial abundances, since they set the initial HCN ice abundance to zero.

In the shadowed disk ($f \leq 0.03$), the HCN ice abundances at around the current orbit of Jupiter ($r \sim 3 - 8$ au) are slightly enhanced ($\sim 5 \times 10^{-6}$). According to

Aikawa et al. (1999) and Eistrup et al. (2016), HCN is formed through the gas-phase reaction of HCO with N atom, with subsequent freeze-out onto dust grains. HCO gas is efficiently formed by hydrogenation of CO on the cold dust-grain surface and cosmic-ray-induced desorption of HCO ice (see also Sections 3.2.1 and 3.2.2). Schwarz & Bergin (2014) and Eistrup et al. (2018) showed that HCN ice becomes abundant in the outer cold region of the disk where CO freezes-out onto dust grains, although it is efficiently produced by a few Myr. Our calculations for both non-shadowed and shadowed disks also show that HCN ice is efficiently formed at the cold regions where CO freezes out onto dust grains. Thus we confirm that the above HCN formation route which starts from hydrogenation of CO is dominant in the disks.

3.2.4. Other organic molecules

In this Section 3.2.4, we show the radial abundance distributions of other major carbon-, nitrogen-,

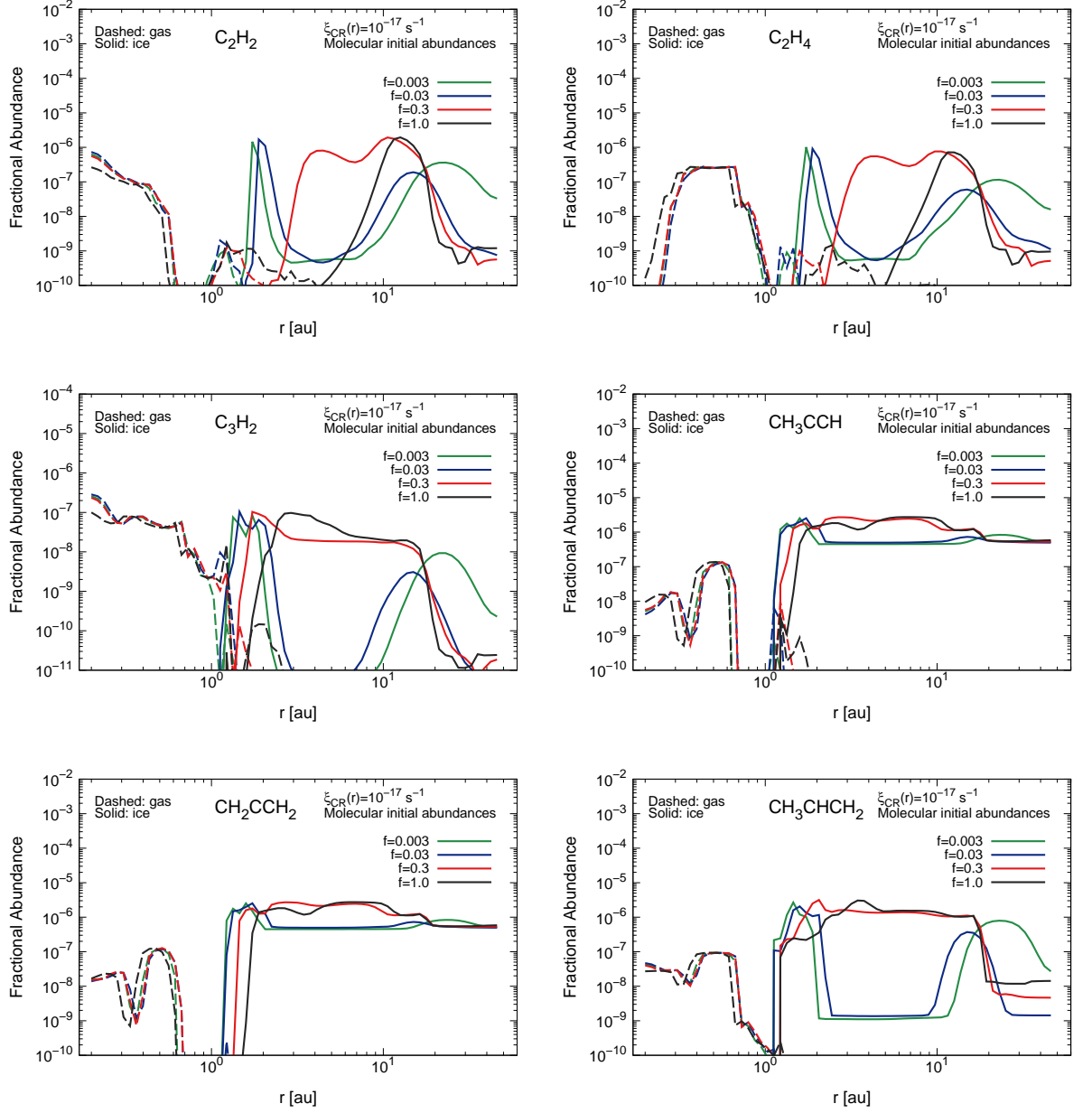


Figure 6. Same as Figure 3, but for C_2H_2 ($n_{C_2H_2}/n_H$, top left panel), C_2H_4 ($n_{C_2H_4}/n_H$, top right panel), C_3H_2 ($n_{C_3H_2}/n_H$, middle left panel), CH_3CCH (n_{CH_3CCH}/n_H , middle right panel), CH_2CCH_2 ($n_{CH_2CCH_2}/n_H$, bottom left panel), and CH_3CHCH_2 ($n_{CH_3CHCH_2}/n_H$, bottom right panel).

and oxygen-bearing molecules, mainly larger organic molecules ³.

Figure 6 shows the radial profiles of fractional abundances for C₂H₂ (acetylene), C₂H₄ (ethylene), C₃H₂ (cyclopropyne), C₃H₄ (propyne CH₃CCH and allene CH₂CCH₂), and C₃H₆ (propylene, CH₃CHCH₂). These are dominant unsaturated hydrocarbon molecules. In the non-shadowed disk ($f = 1.0$), C₂H₂ and C₂H₄ ice abundances are largest ($\sim (1 - 2) \times 10^{-6}$ and $\sim (3 - 8) \times 10^7$, respectively) at $r \sim 10 - 15$ au, which is just inside the CH₄ snowline. In the shadowed disk ($f \leq 0.03$), these ice abundances significantly decrease ($\ll 10^{-7}$) at $r \sim 3 - 15$ au, and increase ($\sim 10^{-6}$) at $r \sim 2$ au. Moreover, in the non-shadowed disk the ice abundances of other molecules (C₃H₂, C₃H₄, and C₃H₆) are enhanced at $r \sim 2 - 15$ au, whereas in the shadowed disk they decrease at $r \sim 2 - 15$ au and increase at $r \sim 1 - 2$ au.

As we describe in Section 3.2.2 (see also e.g., Aikawa et al. 1999; Furuya & Aikawa 2014; Eistrup et al. 2016, 2018; Yu et al. 2016; Bosman et al. 2018), the formation pathways of these unsaturated hydrocarbon molecules are efficient within the CH₄ snowline, since the gas-phase chemical reaction pathways starting from CH₄ + C⁺, and the cosmic-ray-induced photodissociation of CH₄ and subsequent gas-phase combination reactions of CH_x radicals are active. In the shadowed disks ($f \leq 0.03$), the CH₄ snowline positions are $r \lesssim 2$ au and such gas-phase formation reactions do not proceed efficiently at $r \gtrsim 2$ au. Thus, the unsaturated hydrocarbon ices are deficient at $r \sim 3 - 15$ au (including the current orbit of Jupiter), in contrast to saturated hydrocarbons such as CH₄ and C₂H₆.

Figure 7 shows the radial profiles of fractional abundances for CH₃NH₂ (methylamine), CH₂NH (methylene imine), CH₃CN (acetonitrile), HC₃N (cyanoacetylene), NH₂OH (hydroxylamine), and HNCO (isocyanic acid). Figure 8 shows the radial profiles of fractional abundances for CH₃CHO (acetaldehyde), CH₃OCH₃ (dimethyl ether), HCOOH (formic acid), HCOOCH₃ (methyl formate), CH₃COOH (acetic acid), and C₂H₅OH (ethanol). The ice abundances of CH₃NH₂ and NH₂OH at $r \sim 3 - 8$ au (around the Jupiter orbit) are smaller in the non-shadowed disk ($\sim 10^{-8}$ and $\sim 2 \times 10^{-6}$ for $f = 1.0$, respectively) than those in the shadowed disk ($\sim (2 - 7) \times 10^{-6}$ and $\sim (3 - 8) \times 10^{-6}$

for $f \leq 0.03$, respectively). These are saturated molecules. In contrast, the ice abundances of CH₂NH, HC₃N, HCOOH, HCOOCH₃, CH₃COOH, and HNCO at $r \sim 3 - 8$ au are larger in the non-shadowed disk (e.g., $\sim 10^{-7} - 10^{-6}$ for HCOOH and $f = 1.0$) than those in the shadowed disk (e.g., $\lesssim 10^{-8}$ for HCOOH and $f \leq 0.03$). Moreover, the ice abundances of CH₃CN, CH₃CHO, CH₃OCH₃, and C₂H₅OH at $r \sim 3 - 8$ au are larger for $f = 0.03$ (e.g., $\sim 10^{-7} - 10^{-6}$ for CH₃CN) than those for $f = 1.0, 0.3$, and 0.003 (e.g., $< 10^{-7}$ for CH₃CN).

Walsh et al. (2014) discussed that CH₃NH₂ is formed via the sequential hydrogenations of CH₂NH ice, where CH₂NH ice is originated from atom addition to small hydrocarbon radicals (CH₃, CH₂) on the dust grain surfaces. In addition, Garrod et al. (2008) and Walsh et al. (2014) described that on the warm dust grain surfaces the association of the methyl and amine radicals (CH_{3ice} + NH_{2ice}) is also dominant. Such small hydrocarbon radicals are efficiently formed both in the warm and cold grain surfaces by cosmic-ray-induced photodissociation of CH₃OH ice, which is efficiently produced by Reactions 10 and 11 (see Section 3.2.2 and Eistrup et al. 2018). Thus, we find that the former atom addition reaction route is efficient in the shadowed region ($T(r) < 30$ K).

Garrod et al. (2008) explained that NH₂OH is formed initially by NH + OH addition on grains, followed by hydrogenation. In addition, the addition reaction of OH+NH₂ becomes dominant on the warm dust grains (see also e.g., Molyarova et al. 2018). We propose that the former reaction route is efficient in the shadowed region.

We find that the dependance of CH₃CN and HC₃N ice abundances on the values of f are determined by the combination of the following reaction routes. Walsh et al. (2014) described that similar to H₂CO, CH₃CN and HC₃N can form in the gas-phase through multiple pathways. On the cold dust grain surfaces ($T(r) \sim 10 - 30$ K), CH₃CN ice is formed via the sequential hydrogenations of C₂N ice, and C₂N can form via C_{ice} + CN_{ice} and N_{ice} + C_{2ice}, or freeze out from the gas phase (Walsh et al. 2014). In warmer regions, CH₃CN ice can also form via the following radical-radical reaction with no reaction barrier, CN_{ice} + CH_{3ice}. In addition, on the cold dust grain surface ($T(r) \sim 10 - 30$ K), HC₃N ice is formed via the hydrogenation of C₃N ice.

Garrod et al. (2008), Walsh et al. (2014), and López-

³ We note that NH₂OH is technically an inorganic molecule since it does not include carbon.

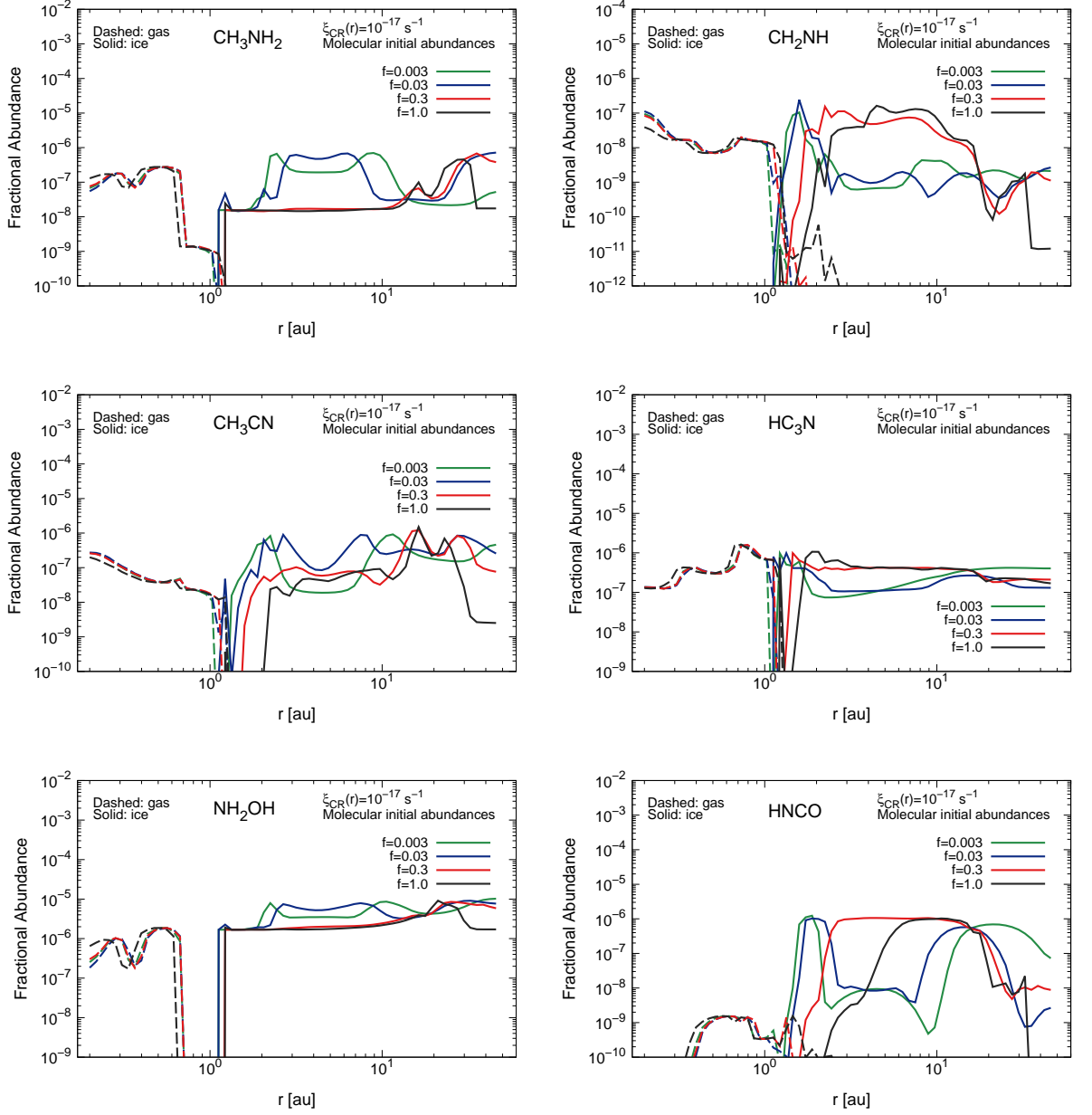


Figure 7. Same as Figure 3, but for CH_3NH_2 ($n_{\text{CH}_3\text{NH}_2}/n_{\text{H}}$, top left panel), CH_2NH ($n_{\text{CH}_2\text{NH}}/n_{\text{H}}$, top right panel), CH_3CN ($n_{\text{CH}_3\text{CN}}/n_{\text{H}}$, middle left panel), HC_3N ($n_{\text{HC}_3\text{N}}/n_{\text{H}}$, middle right panel), NH_2OH ($n_{\text{NH}_2\text{OH}}/n_{\text{H}}$, bottom left panel), and HNCO ($n_{\text{HNCO}}/n_{\text{H}}$, bottom right panel).

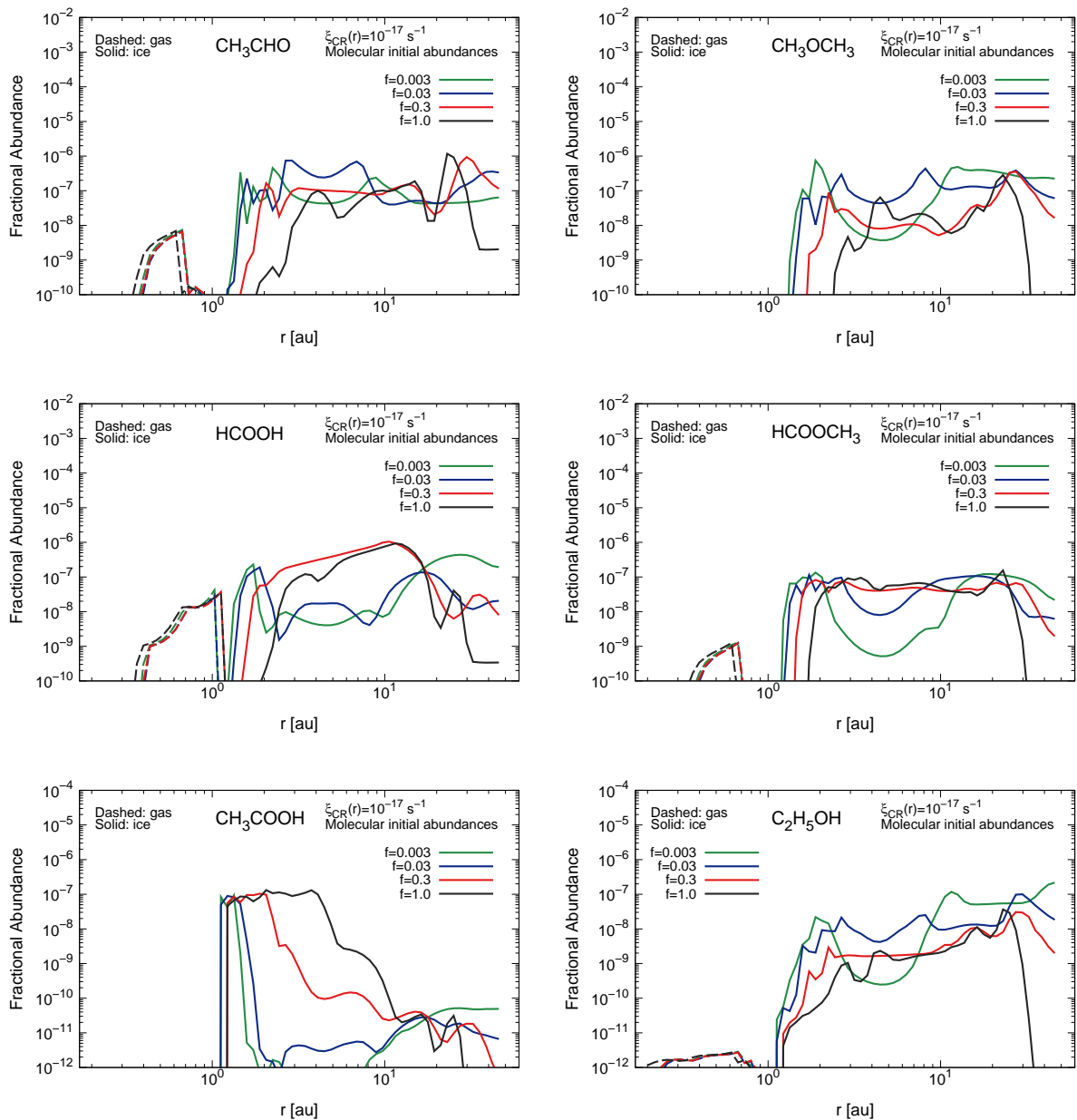
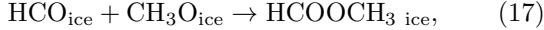


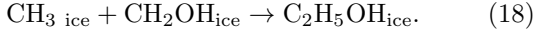
Figure 8. Same as Figure 3, but for CH_3CHO ($n_{\text{CH}_3\text{CHO}}/n_{\text{H}}$, top left panel), CH_3OCH_3 ($n_{\text{CH}_3\text{OCH}_3}/n_{\text{H}}$, top right panel), HCOOH ($n_{\text{HCOOH}}/n_{\text{H}}$, middle left panel), HCOOCH_3 ($n_{\text{HCOOCH}_3}/n_{\text{H}}$, middle right panel), CH_3COOH ($n_{\text{CH}_3\text{COOH}}/n_{\text{H}}$, bottom left panel), and $\text{C}_2\text{H}_5\text{OH}$ ($n_{\text{C}_2\text{H}_5\text{OH}}/n_{\text{H}}$, bottom right panel).

Sepulcre et al. (2015) described that HNCO is formed on the cold dust grain surfaces by hydrogenation of OCN, but is further hydrogenated to NH_2CHO (see Reactions 13 and 14 in Section 3.2.3).

For other organic molecules, grain-surface association of large radical-radical reactions in the warm regions ($T(r) \sim 50$ K) are needed for their formation (e.g., Garrod & Herbst 2006; Garrod et al. 2008; Herbst & van Dishoeck 2009; Vasyunin & Herbst 2013; Walsh et al. 2014). In addition, the dependence of ice abundances on the values of f are determined by the combination of following radical-radical reactions and radical formation reactions from CO and/or CH_3OH on the dust grain surfaces. CH_3CHO , CH_3OCH_3 , HCOOCH_3 , and $\text{C}_2\text{H}_5\text{OH}$ ices can form via the following radical-radical reactions with no reaction barriers on the dust grain surfaces, respectively (Garrod et al. 2008; Walsh et al. 2014);



and



The radicals of HCO, CH_3 , CH_3O , and CH_2OH are produced during the sequential hydrogenation of CO to form CH_3OH and/or the cosmic-ray-induced photodissociation of CH_3OH ice. The abundance of CH_3OH ice at $r \sim 3 - 8$ au is larger in the shadowed disk than that in the non-shadowed disk (see Section 3.2.2), whereas the shadowed disks with lower values of f ($= 0.003$) exhibit lower ice abundances for CH_3CHO , CH_3OCH_3 , HCOOCH_3 , and $\text{C}_2\text{H}_5\text{OH}$. This trend is owing to the temperature dependence of the radical-radical reaction efficiency: the mobility of such radicals is lower than that of hydrogen and light atoms, especially on the cold dust grain surfaces ($T(r) \sim 10 - 30$ K).

HCOOH and CH_3COOH ices can also form via the radical-radical reaction routes on the warm dust grain surfaces. However, CH_3CO , the precursor of CH_3COOH and CH_3CHO (the hydrogenation route), cannot form on the cold dust grain surfaces, since the reaction barrier of $\text{CH}_3\text{ice} + \text{COice}$ is large ($= 3460$ K, Walsh et al. 2014). Moreover, COOH , the precursor of CH_3COOH and HCOOH , cannot form on the cold dust grain surfaces, since the reaction barrier of $\text{OHice} + \text{COice}$ is large ($= 3000$ K, Walsh et al. 2014). We suggest that

HCOOH ice can be formed via $\text{OHice} + \text{HCOice}$, although the mobility of both ices is low on the cold dust grain surfaces (Garrod et al. 2008).

3.2.5. The total complex organic reservoir

Figure 9 shows the radial profiles of sums of fractional abundances with respect to total hydrogen nuclei densities at $t=10^6$ years for larger (complex) organic molecules. In the left (“All”) panel of Figure 9, we show the sums of all larger (complex) organic molecules introduced in Section 3.2 (Figures 4-8); C_2H_6 , H_2CO , CH_3OH , NH_2CHO , C_2H_2 , C_2H_4 , C_3H_2 , CH_3CCH , CH_2CCH_2 , CH_3CHCH_2 , HC_3N , CH_3CN , CH_3CHO , CH_3OCH_3 , CH_3NH_2 , HCOOH , HCOOCH_3 , CH_3COOH , CH_2NH , HNCO , $\text{C}_2\text{H}_5\text{OH}$. We note that CO, H_2O , O_2 , CH_4 , N_2 , NH_3 , HCN , and NH_2OH are not included in this Figure, since they are smaller molecules and/or inorganic molecules.

In the non-shadowed disks, the total icy fractional abundances of the listed organic molecules is $\sim 3 \times 10^{-6}$ just outside the water snowline ($r \sim 1.5$ au), and gradually increases with increasing r . It is $(1 - 2) \times 10^{-5}$ at $r \sim 3 - 8$ au, around the current orbit of Jupiter, and is $(4 - 6) \times 10^{-5}$ outside the CO snowline. In the shadowed disk, it is $(3 - 5) \times 10^{-5}$ at $r \sim 3 - 8$ au, and 2×10^{-5} at $r \gtrsim 10$ au. Thus in the shadowed disk, our model predicts that the dust grains at $r \sim 3 - 8$ au contain $\sim 2 - 5$ times the amount of larger (saturated+unsaturated) organic molecules in total compared with those in the non-shadowed disks.

In the right (“Reduced”) panel of Figure 9, we show the sums of all larger (complex) organic molecules but exclude the dominant unsaturated hydrocarbon molecules shown in Figure 6; C_2H_2 , C_2H_4 , C_3H_2 , CH_3CCH , CH_2CCH_2 , CH_3CHCH_2 . In the non-shadowed disks, at $r \sim 3 - 8$ au, the icy abundances of sums of these “Reduced” organic molecules are smaller ($\sim (3 - 9) \times 10^{-6}$) than those of “All” organic molecules ($(1 - 2) \times 10^{-5}$). In contrast, in the shadowed disks, the icy abundances of sums of organic molecules are similar ($(3 - 5) \times 10^{-5}$) between these two cases. This is because such dominant unsaturated hydrocarbon molecules are frozen onto the dust grains at $r \sim 3 - 8$ au, and their ice abundances significantly decrease with decreasing f (see Figure 6). This result demonstrates that the shadowed region promotes the synthesis of saturated organic molecules rather than unsaturated hydrocarbons. Thus in the shadowed disk, the dust grains at $r \sim 3 - 8$ au are predicted to have around 5 - 10 times the amount of larger saturated organic molecules in total compared

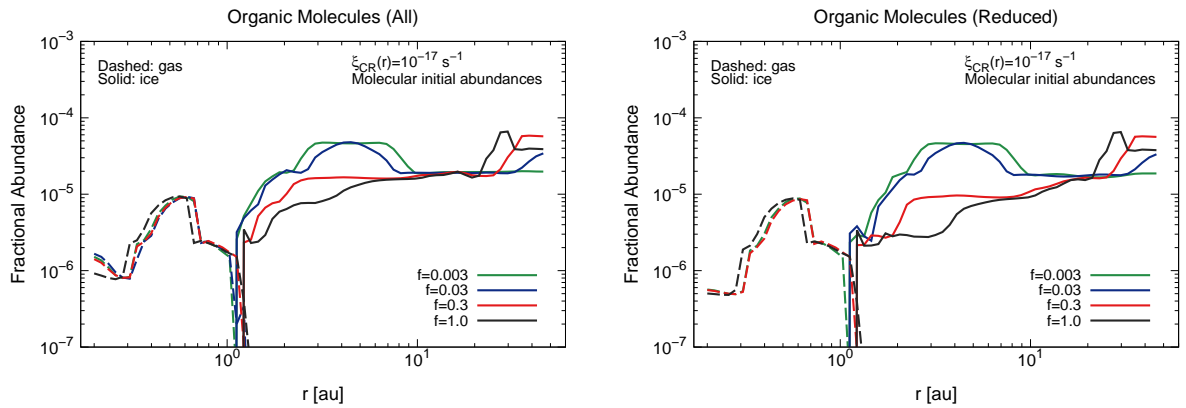


Figure 9. Same as Figure 3, but for the total reservoir of larger (complex) organic molecules. The left panel (“All”) shows the sums of all of larger organic molecules for which we show the results in Section 3.2 (Figures 4-8). The right panel (“Reduced”) shows the sums of all of larger organic molecules after we subtract dominant unsaturated hydrocarbon molecules for which we show the results in Figure 6.

with those in the non-shadowed disks.

3.3. The dependance of the disk chemical structure on ionization rate and initial abundances

In this subsection, we briefly summarize key results of disk chemical evolution for atomic initial compositions and different ionization rates, which are detailed in Appendix A. Figures 14-16 in Appendix A show the radial profiles of fractional abundances at $t=10^6$ years for dominant oxygen-, carbon-, nitrogen-bearing molecules (H_2O , CO , CO_2 , O_2 , CH_4 , C_2H_6 , H_2CO , CH_3OH , N_2 , NH_3 , HCN , and NH_2CHO) in the shadowed and non-shadowed disk midplane ($f = 1.0$ and $f = 0.03$, respectively). In these Figures, we assume either molecular or atomic initial abundances and either low or high ionization rates ($\xi_{\text{CR}}(r) = 10^{-18}$, 10^{-17} [s^{-1}]). We note that Figures 3-5 in Section 3.2 show the radial abundance profiles for the same molecules with molecular initial abundances and $\xi_{\text{CR}}(r) = 10^{-17}$ [s^{-1}].

In Appendix A, we show these results and explain the dependance of the disk chemical evolution on disk ionization rates and initial abundances in detail. According to our calculations, CO/CO_2 abundances become smaller/larger with increasing ionization rates, respectively. CH_4 and C_2H_6 gas abundances within their snowline become smaller as the ionization rates become larger. In addition, abundances of H_2O and organic molecules are larger for molecular initial abun-

dances than those for atomic initial abundances. It is worth noting that O_2 ice abundances are $\sim 10^{-5} - 10^{-4}$ (consistent with the measured cometary abundances, see also Section 4.2) only for atomic initial abundances and the low ionization rates.

3.4. Time evolution of molecular abundances

In this subsection, we briefly summarize some key results for the time evolution of molecular abundances, which are detailed in Appendix B. Figures 17-19 in Appendix B show the time evolution of the radial profiles of fractional abundances for dominant oxygen-, carbon-, nitrogen-bearing molecules (H_2O , CO , CO_2 , O_2 , CH_4 , C_2H_6 , H_2CO , CH_3OH , N_2 , NH_3 , HCN , and NH_2CHO) in the shadowed and non-shadowed disk midplane ($f = 1.0$ and 0.03), when assuming molecular initial abundances and high ionization rates ($\xi_{\text{CR}}(r) = 10^{-17}$ [s^{-1}]). These initial conditions are similar to those in Sections 3.1 and 3.2.

In Appendix B, we describe these results and explain the time evolution of molecular abundances in detail. According to our calculations, in the shadowed region ($r \sim 3 - 8$ au) the icy abundances of CO_2 and organic molecules such as H_2CO , CH_3OH , and NH_2CHO become larger with time. Thus, we find that if the shadowed region is maintained for a relatively long time ($t \sim 10^6$ years), chemical evolution may produce dust grains and solid objects with large amounts of CO_2 and organic molecular ices (see also Section 4.2). In addition, the ice abundances of these molecules can be

a clue in constraining the formation age of solid bodies in the shadowed region.

4. DISCUSSION

4.1. *The C/O and N/O ratios and implication for planetary atmospheres*

The carbon-to-oxygen (C/O) ratios of exoplanet atmospheres have been proposed to be a possible tool to link gas-giant exoplanets to their formation sites in the natal protoplanetary disk (e.g., Öberg et al. 2011; Öberg & Bergin 2016; Madhusudhan et al. 2014; Pon-toppidan et al. 2014; Booth & Ilee 2019; Cridland et al. 2020b; Notsu et al. 2020; Ohno & Ueda 2021; Schneider & Bitsch 2021; Turrini et al. 2021a; Dash et al. 2022; Mollière et al. 2022). This is because the radial-dependent positions of snowlines of abundant oxygen- and carbon-bearing molecules result in systematic radial variations in the C/O ratios in the gas and ice. However, disk chemistry can affect the C/O ratios in the gas and ice, thus potentially erasing the chemical fingerprint of snowlines in atmospheres (Eistrup et al. 2016, 2018; Notsu et al. 2020). Notsu et al. (2020) discussed that hot Jupiters with $C/O > 1$ can only form between the CO_2 and CH_4 snowlines in the non-shadowed disk which has fully inherited interstellar abundances, and where negligible chemistry has occurred because of a low ionisation rate. They also discussed that carbon rich planets are likely rare unless efficient transport of hydrocarbon-rich ices via pebble drift to within the CH_4 snowline (Booth et al. 2017; Booth & Ilee 2019) is a common phenomenon. We note that disk chemistry significantly affect the C/O ratios, through the change of abundances of hydrocarbons and O_2 gas abundances (e.g., Helling et al. 2014; Eistrup et al. 2016, 2018; Notsu et al. 2020; Ohno & Ueda 2021).

The left panels of Figures 10 and 11 shows the radial profiles of C/O ratios at $t=10^6$ years. Different color lines show the profiles for different values of the parameter f ($=1.0, 0.3, 0.03, \text{ and } 0.003$), respectively. As shown in our previous studies (Eistrup et al. 2016, 2018; Notsu et al. 2020), the inclusion of chemistry has a significant impact on the disk elemental abundance ratios of both gas and ice. The ices remain, on the whole, dominated by oxygen (i.e., $C/O < 0.5$). In the non-shadowed disk ($f = 1.0$), between the H_2O and CH_4 snowlines the gas is carbon rich relative to the initial elemental value ($= 0.44$) for molecular initial abundances, whereas gas-phase C/O ratios are $\lesssim 0.44$ for atomic initial abundances. For molecular initial abundances, the gas-phase C/O ratios in these regions are $\sim 1.0 - 1.1$ for the low ionisation rate and $\sim 0.7 - 1.0$ for the high

ionisation rate. In the shadowed disk ($f \leq 0.03$), however, the gas-phase C/O ratios in the shadowed region ($r \sim 2 - 10$ au) are almost unity for the high ionisation rate and/or molecular initial abundances (as suggested by Ohno & Ueda 2021) and 0.8 for the low ionisation rate and atomic initial abundances. This is because CO carries most of the gas-phase C and O there. In addition, the icy-phase C/O ratios reach the initial elemental value ($= 0.44$ in our model) since almost all C and O reservoirs freeze out onto dust grains in the shadowed region ($r \sim 3 - 8$ au). Thus, if planets acquire their atmospheres from the gas in the disk shadowed region, the atmospheres will have sub-stellar metallicities and larger C/O ratios than the initial elemental value ($= 0.44$ in our model) regardless of disk initial abundances and ionisation rates. In addition, the C/O ratios are unity unless the disk has fully atomized initial abundances and negligible chemistry has occurred because of the low ionisation rate. We note that the atmospheres can be polluted by dissolution of accreting oxygen-rich icy planetesimals/pebbles (e.g., Hori & Ikoma 2011; Mordasini et al. 2016) and erosion of cores (e.g., Moll et al. 2017), potentially lowering C/O ratios in planetary atmospheres.

In the bottom left panel of Figure 11 (the case for low ionisation and atomic initial abundances), the icy-phase C/O ratios just outside the water snowline are larger than the initial elemental value, and they exceed 1.0 for $f \leq 0.3$. The peak position shifts inside with decreasing f . In this region, H_2O ice abundances are much smaller ($\sim 10^{-6}$) than those in other models ($> 10^{-5}$). In addition, this region is between HCN and CO_2 snowline, and the HCN ice abundance is larger than those of other molecules (such as H_2O and H_2CO) in this region (see Appendix A). We note that the presence or otherwise of this large peak depends on the relative binding energies of HCN and CO_2 assumed in the model (see also Eistrup et al. 2016).

Since previous studies suggested that atmospheric N/O ratio is also a useful tracer of planet formation locations (Piso et al. 2016; Cridland et al. 2020b; Turrini et al. 2021a; Ohno & Ueda 2021), we also study the radial distributions of N/O ratios in our disk models. The right panels of Figures 10 and 11 shows the radial profiles of N/O ratios at $t=10^6$ years. The ices remain, on the whole, dominated by oxygen (i.e., $N/O < 0.23$). In the non-shadowed disk ($f = 1.0$) and for molecular initial abundances, the gas-phase N/O ratios increase (> 0.4) outside the water snowline, they gradually increase ($\sim 0.4 - 0.5$ and ~ 1.0 outside the H_2O and

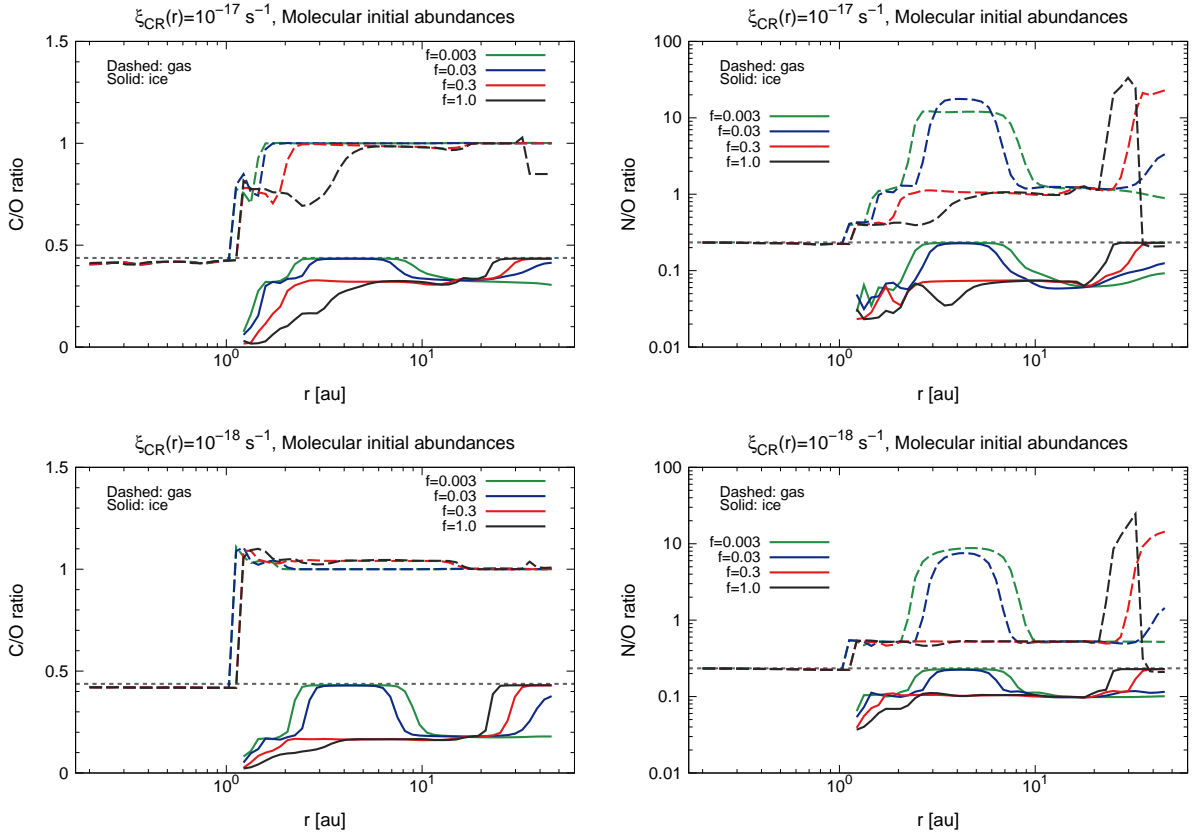


Figure 10. The radial profiles of C/O ratios (left panels) and N/O ratios (right panels) at $t=10^6$ years and for molecular initial abundances (the “inheritance” scenario). The dashed and solid lines show the profiles for gaseous and icy molecules, respectively. The black, red, blue, and green lines show the profiles for different values of the parameter f ($=1.0, 0.3, 0.03$, and 0.003), respectively. Top panels show the results for $\xi_{\text{CR}}(r) = 1.0 \times 10^{-17} [\text{s}^{-1}]$, whereas bottom panels show the results for $\xi_{\text{CR}}(r) = 1.0 \times 10^{-18} [\text{s}^{-1}]$. The horizontal dotted lines show the values of the initial elemental abundance ratios (C/O ratio = 0.44, N/O ratio = 0.23).

CO_2 snowlines, respectively) for the high ionization rate, whereas they are ~ 0.5 for the low ionization rate. This is because of the significant enhancement of CO_2 abundances in the disk with a high ionization rate (see Appendix A.1). In the non-shadowed disk ($f = 1.0$) and for atomic initial abundances, the gas-phase N/O ratios do not increase outside the water snowline, since gas-phase abundances of NH_3 , HCN , and NH_2CHO are at least around an order of magnitude smaller than those for molecular initial abundances (see Appendix A.3). For the high ionisation rate, they reach around unity outside the CO_2 snowline. This is because CO/CO_2 abundance ratios are smaller in the high ionisation rate case than those in the low ionisation rate case (see Appendix A.1). In addition, the gas-phase N/O ratios exceed unity and reach around 10 just outside the CO

snowline in all models, because the binding energy of N_2 is lower than that of CO (see Table 1), leading to the higher N_2 gas abundances around these radii (see also e.g., Turrini et al. 2021a).

In the shadowed disk, the radial profiles of the gas-phase N/O ratios show spatial variations which are much larger than those of the C/O ratios, and thus the N/O ratio would be a useful tracer of the shadowed region in the disks. For molecular initial abundances, the gas-phase N/O ratios are much larger than unity in the shadowed region ($r \sim 3 - 8$ au), and they are $\sim 6 - 9$ for the low ionization rate and $\sim 10 - 20$ for the high ionization rate. This is because of the difference in the binding energies between N_2 and CO , similar to the situation outside the snowline of the non-shadowed disk

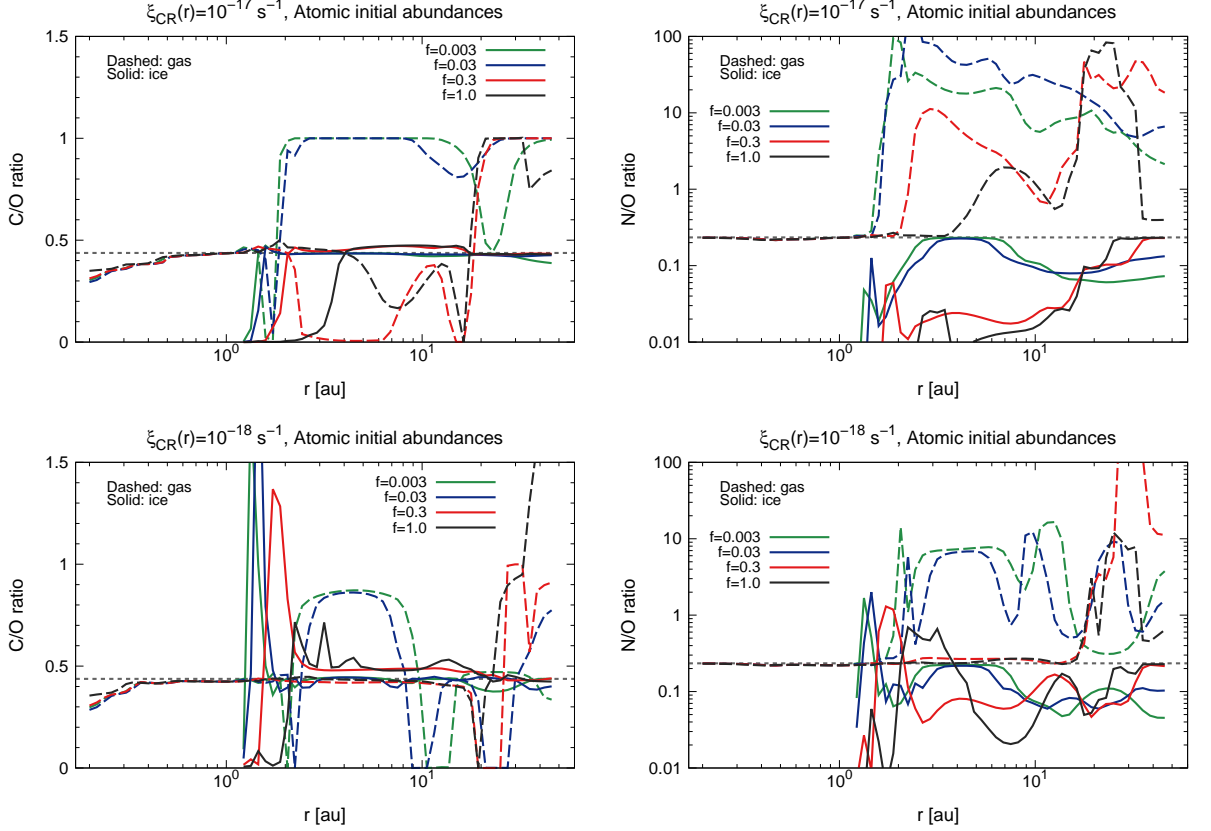


Figure 11. Same as Figure 10, but for atomic initial abundances (“reset” scenario).

($f = 1.0$). In addition, the icy-phase N/O ratios reach the initial elemental value ($= 0.23$ in our model) since almost all N and O reservoirs freeze out onto dust grains in the shadowed region ($r \sim 3 - 8$ au). For atomic initial abundances, the overall pictures are similar, and around the shadowed region the gas-phase N/O ratios are $\gtrsim 10$ and icy-phase N/O ratios reach 0.23. We note that in our results, the icy-phase elemental carbon, oxygen, and nitrogen abundances at $r = 5.3$ au are $\sim 1.4 \times 10^{-5}$, $\sim 3.2 \times 10^{-4}$, and $\sim (6.5 - 7.1) \times 10^{-5}$, respectively, which are similar to the initial elemental abundances.

The results for molecular initial abundances and the low ionisation rate are consistent with those in Ohno & Ueda (2021), although the gas-phase N/O ratios in the shadowed region are much larger (> 100) than that in our disk model (~ 10). This is likely because they used larger literature values of binding energies of CO and N_2 ($E_{\text{des}}(\text{CO})=1180$ K and $E_{\text{des}}(\text{N}_2)=1051$ K) than ours, as the gas-phase N/O ratio is sensitive to those values when both CO and N_2 are frozen. In addition, Ohno & Ueda (2021) included several dominant molecules only

(i.e., N_2 and NH_3 only) and did not include the effects of disk chemical evolution. Moreover, they assumed slightly larger N_2 abundances ($= 3.50 \times 10^{-5}$) and smaller NH_3 abundances ($= 7.78 \times 10^{-6}$) than those in our calculations (see Figure 16). Our calculations also investigate the dependance on initial disk conditions.

Therefore, if planets acquire their atmospheres from the gas in the shadowed region ($r \sim 3 - 8$ au in our disk model), they are expected to have the super-stellar N/O ratios of $\gg 1$ and sub-stellar metallicities. On the other hand, they are expected to have the stellar N/O ratios and super-solar metallicities if the planetary atmospheres are efficiently polluted by solid components (including the case of Jupiter, see Ohno & Ueda 2021).

As discussed in Ohno & Ueda (2021), Saturn, in contrast to Jupiter, may not have the uniform enrichment in the elemental abundances of their atmospheres, if formed in their vicinity of the current orbits. This is because the current Saturn orbit is outside the shadowed region ($r \sim 3 - 8$ au), and N_2 has sublimated into

the gas-phase. In the shadowed disk, the icy-phase N/O ratios at around the current orbit of Saturn ($r \sim 10$ au) are $\lesssim 0.1$ for all models, whereas they reach the initial elemental value ($= 0.23$ in our model) at around the current orbit of Jupiter. In addition, regardless of the initial abundances and ionisation rates, the icy-phase N/O ratios at $r \sim 10 - 40$ au are $\lesssim 0.1$ in the shadowed disk, whereas in the non-shadowed disk they reach the initial elemental value at $r > 24$ au (outside the N_2 snowline). Future observations and entry probe missions on Saturn and also outer icy planets (Uranus and Neptune) would help to distinguish the shadow formation scenario proposed in Ohno & Ueda (2021) from other scenarios, since the elemental abundances such as N in such planets are still uncertain (see e.g., Atreya et al. 2018; Mandt et al. 2020).

Nitrogen abundances within the atmospheres of exoplanets (such as hot Jupiters) can be constrained by the observations of HCN and NH_3 (e.g., MacDonald & Madhusudhan 2017; Hawker et al. 2018; Giacobbe et al. 2021), which are the major nitrogen-bearing species in hot gas-giant atmospheres along with N_2 (e.g., Moses et al. 2011, 2013). Through upcoming observations with the James Webb Space Telescope (JWST) and observations with next-generation facilities (such as ARIEL and ground-based telescopes), it is anticipated that the elemental composition of carbon, oxygen, and nitrogen, and the ratios between them will be determined with much higher precision than currently possible for the atmospheres of many exoplanets such as hot Jupiters (see e.g., Tinetti et al. 2018; Madhusudhan 2019; Changeat et al. 2020; Turrini et al. 2021b).

We note that in addition to C/O ratios, the C/H ratios (carbon elemental abundances) of exoplanet atmospheres have been also proposed to be a possible tool to link gas-giant exoplanets to their formation sites in the protoplanetary disk (e.g., Öberg et al. 2011; Madhusudhan et al. 2014; Pontoppidan et al. 2014; Line et al. 2021; Pelletier et al. 2021). Recently, super-solar and Jupiter-like C/H ratios ($\gtrsim 10^{-3}$) have been confirmed for some hot Jupiters (e.g., Brogi & Line 2019; Gandhi et al. 2019; Pelletier et al. 2021). Pelletier et al. (2021) analyzed thermal emission spectra of a non-transiting hot Jupiter τ Boo b with high spectral resolutions ($R = \lambda/\Delta\lambda = 70000$) and reported that the planet’s atmosphere has super-solar C/H ratio and possibly super-solar C/O ratio. We suggest that the super-solar C/H and C/O ratios might be explained if the atmosphere was formed near the inner edge of the shadowed region and polluted by solid components,

since the solid C/O ratio exceeds unity there when disk chemistry starts from the atomise initial abundances and the cosmic-ray ionization rate is low (see Figure 11, see also Eistrup et al. 2016).

Figures 20, 21, and 22 in Appendix C show respectively the radial profiles of C/H, O/H, and N/H ratios at $t=10^6$ years. In the shadowed disk ($f \leq 0.03$), at $r \sim 3 - 8$ au (around the current orbit of Jupiter), the gas-phase N/H ratios ($\sim 10^{-7} - 10^{-5}$) are larger than the gas-phase C/H and O/H ratios ($\sim 10^{-8} - 10^{-6}$) in each model, which produce super-stellar N/O ratios of $\gg 1$ (see Figures 10 and 11).

4.2. Implications for the small bodies in the solar system

On the basis of our calculations, in the shadowed region the snowline positions of molecules with smaller E_{des} than that of H_2O move inward, and even the most volatile species CO and N_2 freeze-out onto dust grains at around the current orbit of Jupiter ($r \sim 3 - 8$ au), as found in Ohno & Ueda (2021). In the shadowed region, the dust grains at $r \sim 3 - 8$ au are expected to have significant (more than $\sim 5 - 10$ times) amounts of saturated hydrocarbon ices such as CH_4 and C_2H_6 , ices of organic molecules (which are mostly saturated) such as H_2CO , NH_2CHO , CH_3OH , and CH_3NH_2 , in addition to H_2O , CO, CO_2 , NH_3 , N_2 , HCN, and NH_2OH ices, compared with those in the non-shadowed disks (mostly ices of H_2O , CO_2 , NH_3 , and unsaturated hydrocarbon molecules). In addition, the icy abundances of unsaturated hydrocarbons and other organic molecules in the shadowed disks are much smaller than those in the non-shadowed disks.

Here it is worth discussing whether the presence of the shadowed region influences the chemical composition of small objects, such as primitive comets in the solar system. If primitive comets formed from the icy dust grains in the shadowed region of the disks (such as $r \sim 3 - 8$ au for $f \leq 0.03$), they are expected to include more saturated hydrocarbons and complex organic molecules such as H_2CO , NH_2CHO , and CH_3OH , and less unsaturated organic molecules than those formed in the non-shadowed disks.

Reactions of radicals, which are mainly formed by cosmic-ray induced photodissociation of CH_3OH ice, are needed to form complex organic molecules in disks (see Sections 3.2.2 and 3.2.4), assuming that they are not already formed in the molecular cloud phases. In addition, Garrod et al. (2008) discussed that $(CH_2OH)_2$

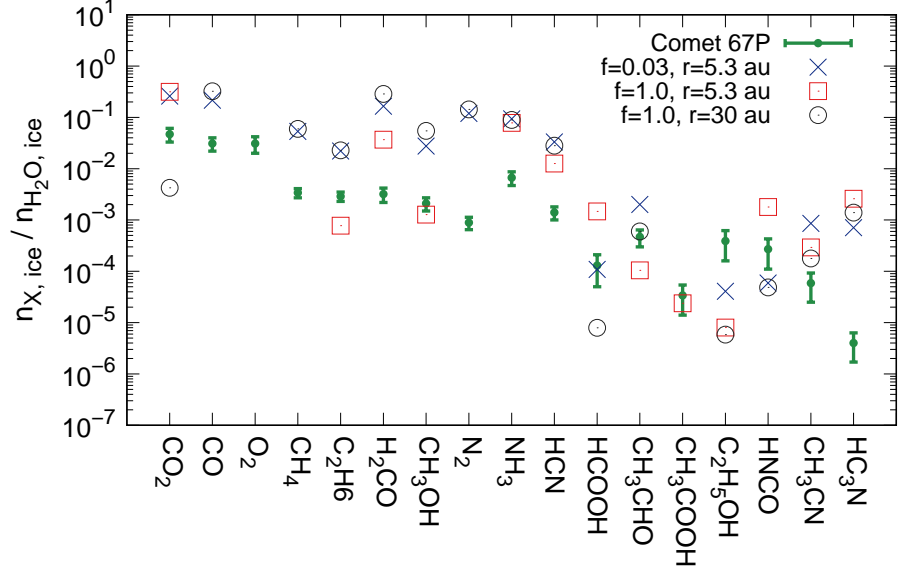


Figure 12. The fractional molecular ice abundances with respect to water ice $n_{X,ice}/n_{H_2O,ice}$ for the coma of comet 67P/Churyumov-Gerasimenko and our standard disk model calculations at $t=10^6$ years. The comet data (green filled circles and lines) are taken from Rubin et al. (2019, 2020) and originally derived from in-situ measurements by ROSINA (Rosetta Orbiter Spectrometer for Ion and Neutral Analysis) for the coma of comet 67P in May/June 2015 before perihelion. The blue crosses show the results of our standard model calculations at $r = 5.3$ au and for $f = 0.03$ (in the shadowed region), the red open squares show those at $r = 5.3$ au and for $f = 1.0$ (between CO_2 and CH_4 snowlines in the non-shadowed disk), and the black open circles show those at $r = 30$ au and for $f = 1.0$ (outside CO and N_2 snowlines in the non-shadowed disk). We note that the points which are not shown in this Figure indicate low ice abundances ($< 10^{-7}$ with respect to water ice) of those species. In our standard model, we assume molecular initial abundances and $\xi_{CR}(r) = 1.0 \times 10^{-17} [s^{-1}]$ (see Sections 3.1 and 3.2).

(ethylene glycol) is formed on the dust grains around the water snowline from its precursor radical CH_2OH , which becomes mobile just as water and other species are beginning to desorb. Moreover, icy grains can efficiently coagulate into larger ($\gg 1$ mm) dust particles and cm-size pebbles outside the water snowline (see Section 2.1 and e.g., Ros & Johansen 2013; Sato et al. 2016; Drążkowska & Alibert 2017; Pinilla et al. 2017). If CH_3OH rich large dust grains and/or pebbles migrate to inside the shadowed region (such as around the water snowline), and/or if the shadowed region disappears due to the disk evolution, the ice abundances of various complex organic molecules in such dust grains and pebbles are also expected to increase (see also Section 4.4). This is because the temperature of such dust grains and pebbles increases (> 30 K) and radical-radical reactions can proceed efficiently in such warm conditions.

Thus in the shadowed disk, both efficient CH_3OH ice formation and the formation of ices of further complex organic molecules such as $(CH_2OH)_2$ may be realized due to the dissipation of shadowed structures and/or migration inside the shadowed region, and they can be realized without dust grains and/or pebbles migrating vast distances, compared with the non-shadowed disk. We suggest that in shadowed disks, complex organic molecules can be formed in situ rather than being fully inherited from molecular clouds.

To date, various complex organic molecules have been detected in comets (such as Hale-Bopp and 67P/Churyumov-Gerasimenko). Several studies discussed that the molecular abundances in comets are determined by the combination of chemical evolution in the protosolar disk and inheritance from molecular

clouds (e.g., Mumma & Charnley 2011; Caselli & Ceccarelli 2012; Walsh et al. 2014; Eistrup et al. 2016, 2018; Altwegg et al. 2017, 2019; Drozdovskaya et al. 2019; Öberg & Bergin 2021). Walsh et al. (2014) discussed that grain-surface fractional abundances (relative to water ice) for the outer region of the non-shadowed disk ($T < 50$ K) are consistent with abundances derived for comets, suggesting a grain-surface route to the formation of COMs observed in cometary comae.

Recently, the abundances of various volatiles and organic molecules (including hydrocarbons) towards comet 67P/Churyumov-Gerasimenko were reported by e.g., Le Roy et al. (2015), Rubin et al. (2015a,b, 2019, 2020), Altwegg et al. (2017, 2019) and Schuhmann et al. (2019). They reported that the relative abundances of CO, CO₂, and C₂H₆ with respect to H₂O are larger than those of other Jupiter-family comets, which might suggest the formation of cometary grains at lower temperature regions (such as below 30 K). In addition, Rubin et al. (2015a) reported the first cometary detection of N₂ towards comet 67P, and discussed that the lower N₂/CO abundance ratio ($\sim 3 \times 10^{-2}$ based on Rubin et al. 2019, 2020) compared with the protostar value ($\sim 10^{-1}$) suggested the cometary grains of 67P are formed in cold regions with $\sim 24 - 30$ K. Schuhmann et al. (2019) also reported the existence of unsaturated hydrocarbons in the coma of comet 67P. We note that gas-phase reactions within the CH₄ snowline are needed to efficiently form unsaturated hydrocarbons (see Sections 3.2.2 and 3.2.4).

In Figure 12, we compare the molecular ice abundances (with respect to water ice) of the coma of comet 67P (Rubin et al. 2019, 2020) and our standard disk model calculations (see Sections 3.1 and 3.2). On the basis of Figure 12, the ice abundances of CO, CH₄, and N₂ in the coma of comet 67P cannot be explained by the icy grains within the CH₄ snowline in non-shadowed disks. In addition, as for results in the cold regions where both CO and N₂ are frozen onto dust grains (both in the shadowed and non-shadowed disks), the CO ice abundances are closer to the value of comet 67P than the N₂ ice abundances. These results also suggest that the icy grains of comet 67P were formed between the CO and N₂ snowlines (see above and Rubin et al. 2015a, 2019, 2020). Such cold regions, where the icy grains of comet 67P are formed, can be located at $r \sim$ a few au for the shadowed disks, whereas they are located at $r > 20$ au for the non-shadowed disk.

In the results of our standard disk model calculations,

the CO₂ ice abundances at $r \sim 5.3$ au in the shadowed disk are around two orders of magnitude larger than those at $r \sim 30$ au in the non-shadowed disk, although the differences in other molecular ice abundances between the two cases are within around one order of magnitude. This is because CO₂ ice formation on the dust grains is not efficient in the coldest regions with $T(r) \lesssim 20$ K (see Section 3.2.1). Thus, the CO₂ ice abundances can be used to distinguish these two regions (the inner cold region ($r \sim 3 - 8$ au, $T(r) \sim 20 - 30$ K) in the shadowed disk and outermost coldest region ($r \sim 30$ au, $T(r) \lesssim 20$ K) in the non-shadowed disk) as formation sites of icy dust grains. The CO₂ ice abundance at $r \sim 30$ au in the non-shadowed disk is around one orders of magnitude smaller than that in comet 67P, whereas that at $r \sim 5.3$ au in the shadowed disk is 4-7 times larger than that in comet 67P. Thus, for explaining the CO₂ ice abundance in comet 67P, the formation of CO₂ ice at $r \sim 5.3$ au in the shadowed disk may be more suitable than that at $r \sim 30$ au in the non-shadowed disk. In addition, if we also include the above discussion about the CO and N₂ abundances, we suggest that the icy grains of comet 67P may have been formed at the region with $T(r) \sim 25$ K, such as the shadowed region.

For the model results in the shadowed region (see Figure 12), the abundances of ices such as H₂CO and CH₃OH are around 1-2 orders of magnitude larger than those of comet 67P, whereas those of C₂H₅OH and CH₃COOH are more than 1 and 3 orders of magnitude smaller, respectively. We suggest that if the cometary grains of 67P are originally from the shadowed region, a temperature rise (due to the inward migration and/or dissipation of the shadowed region) after CH₃OH ice formation in the shadowed region may be needed to trigger radical-radical reactions (see also above) to produce more complex molecules such as C₂H₅OH and CH₃COOH. Future detailed chemical modeling including such physical evolutions may be needed to construct the formation scenario which explains the ice abundances of all molecules in comet 67P simultaneously.

Bieler et al. (2015) and Rubin et al. (2015b) reported that O₂ ice is abundant in comet 67P and the ratio of O₂/H₂O is a few percent (see also Luspay-Kuti et al. 2022). On the basis of Figure 12, our standard disk model is unable to explain the cometary O₂ ice abundances (see Sections 3.1 and 3.2). According to previous studies (e.g., Eistrup et al. 2016, 2018; Taquet et al. 2016) and our calculations, such higher O₂ ice abundances are possible in disks only if chemical starting

conditions were purely atomised and the disk ionisation level was low (see Appendix A.1). In addition, O_2 is very volatile and freezes-out onto dust grains at $r \sim 2 - 10$ au only in the shadowed disk ($f \leq 0.03$, see Appendix A.1). We note that Taquet et al. (2016) suggest that O_2 trapping in H_2O ice at earlier evolutionary stages (such as in the molecular clouds) may also be an explanation.

Other small objects such as asteroids will have similar abundances (such as CO_2 and CH_3OH rich), if they are formed from the dust grains in the shadowed region. Yada et al. (2021) reported the results of preliminary analyses of the Hayabusa2 samples returned from C-type asteroid Ryugu, and showed the infrared spectral profile with weak absorptions at 2.7 and 3.4 μm that imply a carbonaceous composition with indigenous aqueous alteration. Kurokawa et al. (2022) compared the infrared spectra (including 3.1 μm absorption features of ammoniated phyllosilicate) of main belt asteroids collected by the AKARI space telescope and their models of water-rock reactions, and suggested that multiple large main belt asteroids formed beyond the NH_3 and CO_2 snowlines and have been transported to their current locations. Fujiya et al. (2019) inferred from the measurements of CO_2 and H_2O abundances and carbon isotope ratios of carbonate minerals in the Tagish Lake meteorite (an carbonaceous chondrite) that at least some D-type asteroids were formed beyond the CO_2 snowline. We note that D-type asteroids are discovered mainly at the outer edge of the main asteroid belt and in the Jupiter Trojan regions (DeMeo & Carry 2014). Tsuchiyama et al. (2021) reported the discovery of primitive CO_2 -bearing fluids in an aqueously altered carbonaceous chondrite (one of the primitive meteorites), and discussed that its parent body was formed outside the CO_2 snowline and later transported to the inner solar system. Since the CO_2 snowline position moves inward in the shadowed disk, the supply of dust grains and small objects with significant amounts of CO_2 and complex organic molecules to the inner region may be relatively easier than that in the non-shadowed disk. We note that if the shadowed region is maintained for a relatively long time ($t \sim 10^6$ years), chemical evolution may produce dust grains and solid objects with large amounts of CO_2 ice and ices of complex organic molecules such as H_2CO and CH_3OH .

The solid bodies formed at the Kuiper belt may be CO_2 rich if we consider the disk shadowing effect. This is because at $r > 20$ au, the CO_2 ice abundance in the shadowed disk is around one orders of magnitude larger than that in the non-shadowed disk (see Section 3.2.1

and Figure 3).

We note that the CO_2 snowline position will be important both for chemistry and dust grain growth in the disk. Recent laboratory experiments showed that CO_2 ice is less sticky compared to H_2O ice (Musiolik et al. 2016a,b; Fritscher & Teiser 2021). Thus, efficient grain growth is only expected between the H_2O and CO_2 snowlines (Okuzumi & Tazaki 2019; Arakawa & Krijt 2021). If the disk has a shadowed region beyond the water snowline, the region where efficient grain growth can take place might become narrower.

Dartois et al. (2013, 2018) found that UltraCarbonaceous Antarctic MicroMeteorites (UCAMMs) have higher C/Si abundance ratios ($\gtrsim 10^2$) and N/C abundance ratios ($\sim 0.05 - 0.12$) in organic compounds than those in other primitive meteorites and the local interplanetary dust particle (IDPs). They discussed that UCAMMs might be formed in a cold nitrogen rich environment, such as outside the N_2 snowline. We suggest that if the disk has a shadowed region beyond the water snowline, the formation sites of UCAMMs may be located in the inner region of the disk, such as $r \sim 3 - 8$ au.

4.3. Implication for the observations of protoplanetary disks

Many of the complex (organic) molecules described in Sections 3.2.2-3.2.4 have been observed by previous observations with e.g., ALMA towards hot cores/corinos in high-/low-mass star forming regions, respectively (see e.g., Herbst & van Dishoeck 2009; Sakai & Yamamoto 2013; Jørgensen et al. 2020; Yang et al. 2021), and have been detected in the comae of multiple comets (see Section 4.2 and e.g., Mumma & Charnley 2011; Walsh et al. 2014; Altwegg et al. 2019; Drozdovskaya et al. 2019; Rubin et al. 2020). Lee et al. (2019) reported the detections of CH_3CHO and CH_3CN , in addition to CH_3OH , towards Class I disk around FU Ori type young star V883 Ori with ALMA. In addition, some of these molecules have been observed towards Class II disks by previous infrared observations (C_2H_2 , e.g., Pontoppidan et al. 2010) and ALMA observations, such as H_2CO and CH_3OH (see e.g., Loomis et al. 2015; Walsh et al. 2016, 2018; Booth et al. 2021a; van der Marel et al. 2021; Guzmán et al. 2021), and C_3H_2 , CH_3CN , HC_3N , and HCOOH (see e.g., Qi et al. 2013; Öberg et al. 2015; Bergner et al. 2018; Favre et al. 2018; Loomis et al. 2018, 2020; Ilee et al. 2021).

Booth et al. (2021a) reported the first detection of

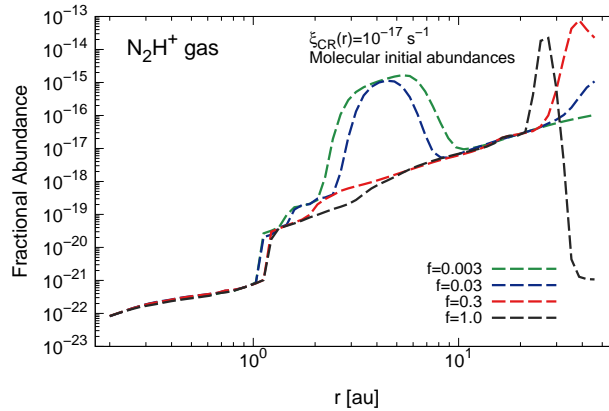


Figure 13. The radial profiles of gas-phase fractional abundances with respect to total hydrogen nuclei densities at $t=10^6$ years for N_2H^+ ($n_{\text{N}_2\text{H}^+}/n_{\text{H}}$). These profiles show the results for $\xi_{\text{CR}}(r) = 1.0 \times 10^{-17} [\text{s}^{-1}]$ and molecular initial abundances (the “inheritance” scenario). The black, red, blue, and green lines show the profiles for different values of the parameter f ($=1.0, 0.3, 0.03, \text{ and } 0.003$), respectively.

CH_3OH in the disk around a Herbig Ae star, HD 100546. They reported that the CH_3OH to H_2CO abundance ratio is higher ($\gtrsim 10$) at the inner edge of the dust ring in the disk ($\sim 10 - 30$ au) than those ($\sim 1 - 2$) in the outer disk (> 100 au) and in the TW Hya disk (Walsh et al. 2016). They discussed that at the inner edge CH_3OH is proposed to originate from thermal desorption. van der Marel et al. (2021) and Brunken et al. (2022) reported the detections of CH_3OH , H_2CO , and CH_3OCH_3 line emission in the vicinity of the asymmetric dust trap in the disk around a Herbig Ae star Oph IRS 48. They discussed that these molecules are thermally desorbed from icy dust grains and that such dust traps provide huge icy grain reservoirs in the disk midplane.

Recent dust continuum survey observations of protoplanetary disks (with e.g., ALMA) have shown that disk substructures, most prominently gas-depleted gaps and dust-rich rings, are common (e.g., Andrews et al. 2016, 2018; Andrews 2020; Dullemond et al. 2018; Huang et al. 2018; Isella et al. 2016, 2018; Tsukagoshi et al. 2016). In addition, the recent MAPS (Molecules with ALMA at Planet-forming Scales)⁴ survey obtained spatial distributions (with $\Delta r \sim 10 - 50$ au) of line emission for CO (Zhang et al. 2021) and some other organic molecules (H_2CO , HCN, CH_3CN , HC_3N , and C_3H_2 , see Guzmán et al. 2021; Öberg et al. 2021; Ilee

et al. 2021) towards three T Tauri disks (IM Lup, GM Aur, AS 209) and two Herbig Ae disks (HD 163296, MWC 480). They found that disk substructures (such as rings and gaps) are also common in molecular gas emission.

Since a shadowed region can be formed in the midplanes beyond such dust rings/traps of these disks by blocking the radiation from the central star, we propose that the effects of shadows need to be taken into account when we discuss chemical evolution of complex organic molecules in disks with such dust rings and asymmetric traps. Alarcón et al. (2020) calculated the temperature and chemical structures of disks with gas-depleted gaps. They showed that the disk midplane temperature in the gap increases, producing local sublimation of key volatiles, while it decreases in the ring, causing a higher volatile deposition onto the dust grain surfaces. Isella et al. (2018) and Okuzumi et al. (2022) described that the outer wall of the gap produced by a giant planet receives extra starlight heating and puffs up, throwing a shadow across the disk beyond. In addition, Ohashi et al. (2022) suggested from their ALMA observations that the dust clumps in the disk around a Class 0/I protostar create the shadowed region outside, resulting in the sudden drop in temperature. We predict that, as well as the shadowed region beyond the water snowline (discussed in this paper), the freeze-out of molecules onto dust grains and efficient formation of organic molecules are also expected to occur in the shadowed region formed

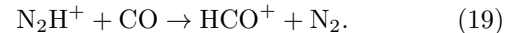
⁴ <http://alma-maps.info>

by the presence of a giant planet and/or dust clumps.

In this study, we adopt a 1D physical model of the protosolar disk (T Tauri disk) in order to investigate the effects of shadow structures on the chemical evolution of the disk midplane and compare the results with the molecular composition of small objects in the solar system (see also Section 4.2). The influence of disk shadowing is expected to be larger in the disk midplane than in the disk surface, since it is easier for direct stellar light to reach the surface than the midplane (Ueda et al. 2019; Okuzumi et al. 2022). We note that the lines from more rare isotopologues trace deeper regions in the disks, but the disk midplane is obscured if the dust emission is optically thick. In addition to future observations of molecular lines with much higher spatial resolutions towards the disks using e.g., ALMA and ngVLA (next generation Very Large Array), further calculations of disk chemical evolution with 2D physical models of both T Tauri disks and Herbig Ae disks are also important to investigate whether or not the effects of shadows are needed to explain the observed distributions of molecular emission. Since the dust opacities at the frequencies of ngVLA are lower than those of ALMA, observations with ngVLA will be useful to trace the inner molecular gas abundances, such as within 10 au. In addition, ngVLA expects to resolve the dust emission at cm wavelengths with $\Delta r \lesssim 1$ au, and thus will be able to confirm the variation in dust density profile at the water snowline and presence of the shadowed region beyond the water snowline even in disks around T Tauri stars ⁵.

We note that future calculations of disk chemical evolution with 2D physical models would be also useful to investigate the effects of shadowing on composition of planetary atmospheres. This is because some recent theoretical studies (e.g., Tanigawa et al. 2012; Morbidelli et al. 2014) and observational studies (e.g., Teague et al. 2019) suggested that the flow of gas into the gap produced by a growing planet is dominated by gas falling vertically from a height of at least one scale height (see e.g., Cridland et al. 2020a).

N_2H^+ is considered to be a useful probe of the CO and N_2 snowlines in disks (e.g., Qi et al. 2013, 2019; Aikawa et al. 2015; van 't Hoff et al. 2017; Murillo et al. 2022), because it is destroyed by proton transfer to CO,



Aikawa et al. (2015) suggested from their disk modeling that the N_2H^+ abundance can have a peak at the temperature slightly below that of CO sublimation, even if the binding energies of CO and N_2 are nearly the same. Figure 13 shows the radial profiles of the N_2H^+ abundances for various values of f . The CO freezes-out onto dust grains in the shadowed region, and thus N_2H^+ abundances at $r \sim 3 - 8$ au become larger in the shadowed disk ($\sim 10^{-15}$ for $f \leq 0.03$) than those in the non-shadowed disk ($< 10^{-17}$ for $f = 1.0$) by several orders of magnitudes. Thus, N_2H^+ line emission may potentially trace the shadowed region of the disk beyond the water snowline, although previous observations of N_2H^+ lines do not resolve the spatial scales around the water snowline ($r \sim 1 - 10$ au). We note that the N_2H^+ abundances in the disk midplane are lower than those within the disk surface (Aikawa et al. 2015; van 't Hoff et al. 2017), because of the high densities and low ionization rates. Further chemical and radiative-transfer modeling in the 2D disk structures with shadow structures are needed to confirm whether N_2H^+ line emission can really be used as observational tracer of such shadowed regions, since the line emission also traces the vertical distributions of CO and N_2 (Qi et al. 2019), and observations of the disk midplane directly are not easy because of the high optical depths at ALMA wavelengths.

4.4. Other model caveats

In our disk chemical modeling, we implicitly assumed that ices on grains are formed by homogeneous layers regardless of their composition or crystallinity, as most astrochemical models of disks assume. However, recently Kouchi et al. (2021) suggested from their transmission electron microscopy studies that the macroscopic morphology of icy dust grains are as follows: amorphous H_2O covered the refractory grain uniformly, CO_2 nanocrystals were embedded in the amorphous H_2O , and a polyhedral CO crystal is attached to the amorphous H_2O . Such morphology of dust grains would affect the chemical evolution in the disks, since the binding energies and non-thermal desorption rates depend on the chemical composition of the ice mantles on the dust grains (e.g., Bertin et al. 2016; Cuppen et al. 2017; Penteado et al. 2017).

Heinzeller et al. (2011) investigated the effects of physical mass transport phenomena in the radial direction by viscous accretion and in the vertical direction by diffusive turbulent mixing and disk winds. They showed that the gas-phase molecular abundances of such as H_2O

⁵ see Okuzumi et al. (2021) in ngVLA-J memo series, <https://ngvla.nao.ac.jp/researcher/memo/>

and CH₃OH are enhanced in the warm surface layer due to the effects of vertical mixing. [van der Marel et al. \(2021\)](#) discussed that this vertical transport may be important to explain the observed abundance of CH₃OH in the disk around IRS 48, in addition to icy dust concentrations at the dust trap. In addition, we assume that the disk physical structure is steady and that the shadow structure is maintained for 10⁶ years. We note that the inward migration of solids and/or destruction of the shadow structure after the efficient formation of CH₃OH ice in the shadowed region may increase the abundances of various complex organic molecules in the inner disks around the water snowline (see also Section 4.2). Future observations of organic molecular lines with e.g., ngVLA and infrared telescopes (such as JWST and GREX-PLUS) are expected to constrain the abundances in such inner warm region.

5. CONCLUSIONS

In this study, we investigated the radial abundance distributions of dominant carbon-, oxygen-, and nitrogen-bearing molecules and the radial distributions of elemental abundance ratios (C/O and N/O ratios) in the gas and ice of disks with shadow structures. We used a detailed gas-grain chemical reaction network and calculated chemical structures in the shadowed disk mid-plane around a T Tauri star (a protosolar-like star). Gas-phase reactions, thermal and non-thermal gas-grain interactions, and grain-surface reactions were included in our adopted reaction network. We investigated the dependance of the disk chemical structures on ionisation rates and initial abundances. We discussed the effects of disk shadowing on chemical evolution of complex organic molecules and forming planetary atmospheres. We also compared the results of our calculations with the molecular composition of small bodies in the solar system (such as comets and asteroids) and recent observational results of protoplanetary disks. Our findings can be summarized as follows:

- In the shadowed disks ($f \leq 0.03$), the snowline positions of molecules with smaller E_{des} than that of H₂O move inward, and even the most volatile species, CO and N₂, freeze-out onto dust grains at around the current orbit of Jupiter ($r \sim 3 - 8$ au). Our detailed calculations confirm the results of [Ohno & Ueda \(2021\)](#) who showed the freeze-out of CO and N₂ onto dust grains in the shadowed region with using more simplified calculations. Meanwhile, we newly find that the dust grains within the shadowed regions have significant (more than 5–10 times) amounts of saturated

hydrocarbon ices such as CH₄ and C₂H₆, ices of organic molecules such as H₂CO, NH₂CHO, and CH₃OH, in addition to H₂O, CO, CO₂, NH₃, N₂, HCN, and NH₂OH ices, compared with those in the non-shadowed disks (mostly ices of H₂O, CO₂, NH₃, and unsaturated hydrocarbon molecules). We note that these abundant saturated hydrocarbons and various organic molecules such as H₂CO, NH₂CHO, and CH₃OH were not reported by [Ohno & Ueda \(2021\)](#), since they approximated various organic molecules by considering C₂H₆ alone.

- The icy abundances of C₂H₆, HCN, NH₂OH, and complex organic molecules (which are mostly saturated) such as H₂CO, CH₃OH, NH₂OH, NH₂CHO, and CH₃NH₂ at $r \sim 3 - 8$ au in the shadowed disks are enhanced compared with the values in the non-shadowed disk, although the snowline positions of these molecules are $r \lesssim 3$ au regardless of the values of f . We concluded that the sequential hydrogenation reactions of (especially) CO on the cold dust grains play a vital role in efficiently forming these molecules, in addition to reaction pathways starting from the cosmic-ray induced photodissociation of CH₃OH. We found that if the shadowed region is maintained for a relatively long time ($t \sim 10^6$ years), chemical evolution may produce dust grains and solid objects with large amounts of CO₂ and organic molecular ices (see also Appendix B).
- The icy abundances of unsaturated hydrocarbons such as C₂H₂, C₂H₄, C₃H₂, C₃H₄, C₃H₆ and HC₃N at $r \sim 3 - 8$ au (just outside their snowlines) are much smaller than those of a non-shadowed disk, since gas-phase chemical reactions especially within the CH₄ snowline (~ 15 au for $f = 1.0$ and $\lesssim 2$ au for $f \leq 0.03$) mainly drive the formation of these molecules. Moreover, the icy abundances of unsaturated complex organic molecules such as HCOOCH₃, HCOOH, CH₃COOH outside the snowlines are much smaller than those of a non-shadowed disk, since grain-surface association of large radical-radical reactions in the warm regions ($T(r) \sim 50$ K) are needed for the formation of these molecules. In addition, the icy abundances of other molecules such as CH₃CN, CH₃CHO, CH₃OCH₃, and C₂H₅OH are larger for $f = 0.03$ than those for $f = 1.0, 0.3$, and 0.003 , since they are determined by the combinations of radical-

radical reactions and gas-phase reactions / radical formation reactions from CO and/or CH₃OH on the dust grain surfaces.

- We also studied the impacts of different ionization rates and initial chemical abundances on disk chemical structures in Appendix A. We found that CO/CO₂ abundances become smaller/larger with increasing ionization rates, respectively. In addition, CH₄ and C₂H₆ gas abundances within their snowline become smaller as the ionization rates become larger. Abundances of H₂O and organic molecules are larger for molecular initial abundances than those for atomic initial abundances. Moreover, O₂ ice abundances are $\sim 10^{-5} - 10^{-4}$ (consistent with the measured cometary abundances) only for atomic initial abundances and the low ionization rates. O₂ is very volatile and freezes-out onto dust grains at $r \sim 2 - 10$ au only in the shadowed disk.
- In the shadowed region, the gas-phase C/O ratios are almost unity for the high ionisation rate and/or molecular initial abundances and 0.8 for the low ionisation rate and atomic initial abundances. In addition, the radial profiles of the gas-phase N/O ratios show spatial variations which are much larger than those of the C/O ratios, and thus the N/O ratio would be a useful tracer of the shadowed regions of disks. For molecular initial abundances, the gas-phase N/O ratios are much larger than unity in the shadowed region, and they are $\sim 6-9$ for the low ionization rate and $\sim 10-20$ for the high ionization rate. The icy-phase C/O and N/O ratios reach the initial elemental values in the shadowed region. Therefore, if the planets acquire their atmospheres from the gas in the shadowed region ($r \sim 3 - 8$ au in our disk model), they are expected to have super-stellar N/O ratios of $\gg 1$, super-stellar C/O ratios of around unity in most cases, and sub-stellar metallicities. In contrast, they are expected to have stellar N/O and C/O ratios and super-solar metallicities if the planetary atmospheres are efficiently polluted by solid components (including the case of Jupiter, see Ohno & Ueda 2021). Upcoming and future observations by JWST and ARIEL will constrain such elemental ratios precisely for atmospheres of many exoplanets such as hot Jupiters.
- We discussed whether the presence of a shadowed region influences the chemical composition of small objects, such as primitive comets and asteroids in the solar system. Recently the abundances of various volatiles and organic molecules towards comet 67P/Churyumov-Gerasimenko were reported, and some of the results (including CO, CO₂, C₂H₆, N₂, and O₂ abundances) would suggest the formation of cometary grains in lower temperature regions with $T \sim 25$ K, which can be found in the shadowed region.
- We propose that CO₂ ice abundances can be used to distinguish the inner cold region ($r \sim 3 - 8$ au, $T(r) \sim 20 - 30$ K) in the shadowed disk and the outermost coldest region ($r \sim 30$ au, $T(r) \lesssim 20$ K) in the non-shadowed disk as formation sites of icy dust grains. Moreover, if CH₃OH rich large dust grains and/or pebbles migrate to inside the shadowed region (such as around the water snowline), and/or if the shadowed region disappears due to the disk evolution, the ice abundances of various complex organic molecules are also expected to increase. This is because radical-radical reactions may be able to proceed efficiently due to the rapid heating.
- N₂H⁺ line emission could potentially trace the shadowed region of the protoplanetary disks beyond the water snowline, although further modeling and observations with much higher spatial resolution than currently conducted are needed.

On the basis of our calculations, we conclude that a shadowed region allows the recondensation of key volatiles onto dust grains, and may explain to some degree the trapping of icy molecules such as CO₂, CO, N₂ and O₂ in the dust grains that formed comet 67P/Churyumov-Gerasimenko. In addition, in a shadowed disk Jupiter need not to have migrated vast distances to explain its atmospheric composition. In the shadowed disk, both efficient CH₃OH ice formation and formation of ices of further complex organic molecules such as (CH₂OH)₂ driven by rapid heating may be realized without dust grains and/or pebbles migrating vast distances, compared with the non-shadowed disk. Thus, we propose that in the shadowed disks various complex organic molecules can be formed in situ rather than being fully inherited from molecular clouds. Further chemical modeling (such as using 2D physical models of both T Tauri disks and Herbig Ae disks) and comparison with observations of disks (using e.g., ALMA

and ngVLA), planetary atmospheres, and small objects (comets and asteroids) in the solar system will further constrain the effects of disk shadowing on chemical evolution.

Software: RADMC-3D (Dullemond et al. 2012)

1 This study was started originally based on the discussion
 2 during and after the online workshop 2021 on planetary
 3 system formation for young scientists in Japan, in which
 4 S.N. and T.U. are two of organizers of the workshop. We
 5 thank the referee for important suggestions and com-
 6 ments. We are grateful to Nami Sakai, Yuri Aikawa,
 7 and Satoshi Okuzumi for their useful comments. Our
 8 numerical studies were carried out on PC cluster at Cen-
 9 ter for Computational Astrophysics (CfCA), National
 10 Astronomical Observatory of Japan (NAOJ). S.N. is
 11 grateful for support from RIKEN Special Postdoctoral
 12 Researcher Program (Fellowships), and MEXT/JSPS
 13 (Japan Society for the Promotion of Science) Grants-in-
 14 Aid for Scientific Research (KAKENHI) Grant Numbers
 15 JP20K22376, JP20H05845, and JP20H05847. K.O. is
 16 supported by JSPS Overseas Research Fellowships and
 17 JSPS KAKENHI Grant Number JP19K03926. T.U. is
 18 supported by Grants-in-Aid for JSPS Fellows Grant
 19 Number JP19J01929, and acknowledges the support of
 20 the DFG-Grant “Inside: inner regions of protoplanetary
 21 disks: simulations and observations” (FL 909/5-
 22 1). C.W. acknowledges financial support from the Uni-
 23 versity of Leeds and from the Science and Technology
 24 Facilities Council (grant numbers ST/T000287/1 and
 25 MR/T040726/1). H.N. is supported by MEXT/JSPS
 26 KAKENHI Grant Numbers JP18H05441, JP19K03910
 27 and JP20H00182, NAOJ ALMA Scientific Research
 28 grant No. 2018-10B, and FY2019 Leadership Program
 29 at NAOJ.

APPENDIX

A. THE DEPENDANCE OF THE DISK CHEMICAL STRUCTURES ON IONIZATION RATES AND INITIAL ABUNDANCES

In this Appendix A, we explain the dependance of the disk chemical evolution on disk ionization rates and initial abundances. Figures 14-16 shows the radial profiles of fractional abundances at $t=10^6$ years for dominant oxygen-, carbon-, nitrogen-bearing molecules (H_2O , CO , CO_2 , O_2 , CH_4 , C_2H_6 , H_2CO , CH_3OH , N_2 , NH_3 , HCN , and NH_2CHO) in the shadowed and non-shadowed disk midplane ($f = 1.0$ and $f = 0.03$, respectively). In these Figures, we assume either molecular or atomic initial abundances and either low or high ionization rates ($\xi_{\text{CR}}(r) = 10^{-18}$, 10^{-17} [s^{-1}]). We note that Figures 3-5 in Section 3.2 show the radial abundance profiles for the same molecules with molecular initial abundances and $\xi_{\text{CR}}(r) = 10^{-17}$ [s^{-1}].

A.1. H_2O , CO , CO_2 , and O_2

Figure 14 shows the radial profiles of fractional abundances for dominant oxygen-bearing molecules; H_2O , CO , CO_2 , and O_2 . For molecular initial abundances, the H_2O ice abundances outside the water snowline are $\sim (1 - 2) \times 10^{-4}$

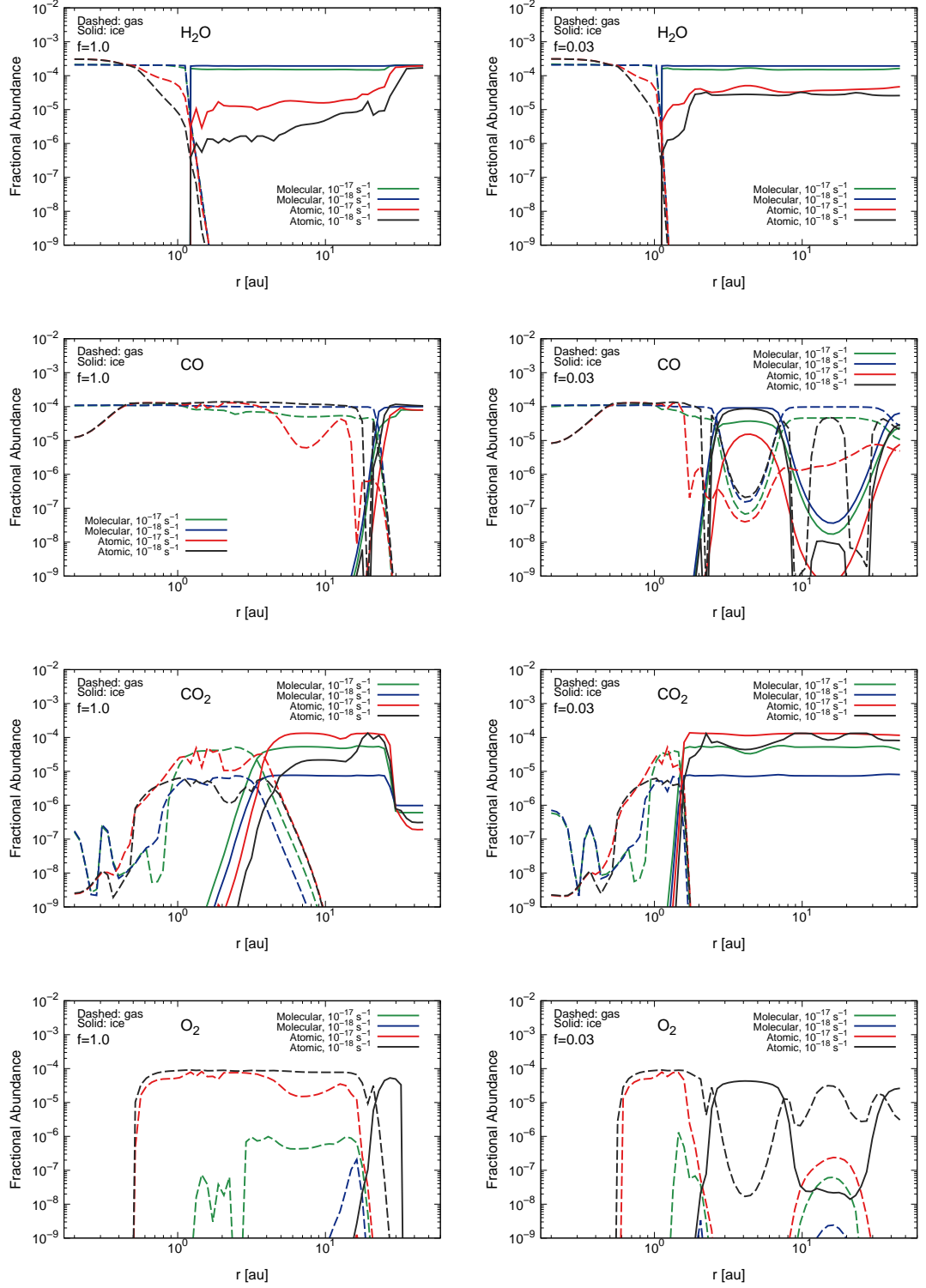


Figure 14. The radial profiles of fractional abundances with respect to total hydrogen nuclei densities n_X/n_H at $t=10^6$ years for H_2O (top panels), CO (second row panels), CO_2 (third row panels), and O_2 (bottom panels). Left panels show the results for the disk midplane with the monotonically decreasing density and temperature profile ($f=1.0$), and right panels show the results for the shadowed disk midplane ($f=0.03$). In each panel, the dashed and solid lines show the profiles for gaseous and icy molecules, respectively. Green and blue lines show the results for molecular initial abundances (the “inheritance” scenario), and red and black lines show the results for atomic initial abundances (the “reset” scenario). Green and red lines show the results for the higher cosmic-ray ionization rate $\xi_{CR}(r) = 1.0 \times 10^{-17} [s^{-1}]$, whereas blue and black lines show the results for the lower cosmic-ray ionization rate $\xi_{CR}(r) = 1.0 \times 10^{-18} [s^{-1}]$.

(see also Section 3.2.1), which are similar to the assumed value of the initial H₂O ice abundance ($= 1.984 \times 10^{-4}$). For atomic initial abundances, they decrease outside the water snowline, and at $r \sim 2 - 10$ au they are $\sim 10^{-6} - 10^{-5}$ for $f = 1.0$ and $\sim (2 - 5) \times 10^{-5}$ for $f \leq 0.03$. In addition, just outside the H₂O snowline the H₂O ice abundances are about an order of magnitude larger in the high ionisation case ($\sim 10^{-5}$) than those in the low ionisation case ($\sim 10^{-6}$). Eistrup et al. (2016) described that in the case of atomic initial abundances, the H₂O ice is not efficiently produced in the outer disk and the ion-molecule reactions in the gas-phase (Hollenbach et al. 2009) are contributing to the formation of water. Previous studies (e.g., Schmalzl et al. 2014; Notsu et al. 2021; van Dishoeck et al. 2021) discussed that it takes more than around 1 Myr of the pre-stellar phase to produce water ice with an abundance of $\gtrsim 10^{-4}$.

For molecular initial abundances, the total CO (gas+ice) abundances outside the water snowline are $\sim 10^{-4}$ for the low ionisation rate and $\sim (3 - 6) \times 10^{-5}$ for the high ionisation rate. This decrease of CO coincides with the overall enhancement of CO₂ ice outside the CO₂ snowline. Under the high ionisation rate, CO destruction pathways of Reactions 6 (icy phase) and 7 (gas phase) are efficient (see Section 3.2.1). In the shadowed disk ($f = 0.03$), CO freezes-out onto dust grains at around the current orbit of Jupiter ($r \sim 3 - 8$ au), and for atomic initial abundances and the high ionisation rate, a larger decrease of total CO abundance ($\lesssim 10^{-5}$) beyond the CO₂ snowline is shown.

CO₂ gas abundances between the H₂O and CO₂ snowlines and CO₂ ice abundances outside CO₂ snowline are larger for the high ionisation rate than those for the low ionisation rate. In addition, they are also larger for atomic initial abundances than those for molecular initial abundances. For atomic initial abundances and the high ionisation rate, CO₂ ice abundances are larger ($\gtrsim 10^{-4}$) outside the CO₂ snowline, with the decreases of CH₄ gas and total (gas+ice) CO abundances. We note that in the non-shadowed disk ($f = 1.0$), CO₂ ice abundances at $r > 30$ au are significantly smaller ($< 10^{-6}$). This is because this region has the coldest conditions ($T(r) \lesssim 20$ K), and the formation of H₂O ice (Reaction 5) is faster than that of CO₂ ice (Reaction 6) (Eistrup et al. 2016).

The gas-phase O₂ abundances are approximately two orders of magnitude larger for atomic initial abundances than those for molecular initial abundances. The O₂ gas abundances between the water and O₂ snowlines are $\sim 10^{-5} - 10^{-4}$ for atomic initial abundances and $< 10^{-6}$ for molecular initial abundances. This is because in the gas-phase O₂ is formed from atomic oxygen via Reaction 8 (Walsh et al. 2015; Taquet et al. 2016; Eistrup & Walsh 2019), and the initial atomic oxygen abundance is 3.2×10^{-4} for atomic initial abundances whereas that is zero for molecular initial abundances. In the shadowed disk ($f \leq 0.03$), O₂ freezes-out onto dust grains at $r \sim 2 - 10$ au, and returns to the gas phase at $r > 10$ au. O₂ ice is mainly formed from atomic oxygen via Reaction 10 (Taquet et al. 2016; Eistrup & Walsh 2019). For the high ionisation rate, O₂ ice photodissociation becomes efficient and the released oxygen is contained in other major oxygen-bearing molecules (Eistrup et al. 2016; Taquet et al. 2016)). Thus, O₂ ice abundances are low ($\ll 10^{-9}$) for molecular initial abundances and/or the high ionisation rates, and they are $\sim 10^{-5} - 10^{-4}$ only for atomic initial abundances and the low ionisation rates, which is consistent with the results of previous studies (e.g., Eistrup et al. 2016; Eistrup & Walsh 2019; Taquet et al. 2016). Such larger abundances are consistent with the measured cometary abundances (Bieler et al. 2015; Rubin et al. 2015b, see also Section 4.2 of this paper).

According to right-hand panels in Figure 14, both O₂ and H₂O ice abundances are similar ($\sim (3 - 5) \times 10^{-5}$) in the shadowed region ($r \sim 2 - 10$ au) in the disk with atomic initial abundances and low ionisation rates. As we explain in Section 4.2, the ratio of O₂/H₂O in comet 67P is a few percent (Bieler et al. 2015; Rubin et al. 2015b). Thus in reality, the models between our assumed parameters (such as partially inheritance initial abundances and/or the ionization rates of $\sim 5 \times 10^{-18}$) might well reproduced the observed O₂ and H₂O ice abundance ratios.

A.2. Other dominant carbon-bearing molecules

For molecular initial abundances, the CH₄ and C₂H₆ gas abundances within their snowline become smaller as the ionisation rate becomes larger. This is because CH₄ and C₂H₆ gas are not efficiently formed in these regions, and they are destroyed by cosmic-ray-induced photodissociation and ion-molecule reactions (such as CH₄+C⁺). Thus, carbon is converted from CH₄ gas to CO₂, H₂CO, and hydrocarbons such as e.g., C₂H₂, C₂H₄, C₃H₂, and C₃H₄ (Aikawa et al. 1999; Eistrup et al. 2016, 2018; Yu et al. 2016, see also Sections 3.2.2 and 3.2.4). In addition, for atomic initial abundances, the CH₄ and C₂H₆ gas abundances within the CH₄ snowline are much smaller ($\ll 10^{-8}$) than those for molecular initial abundances. For atomic initial abundances, the CH₄ and C₂H₆ ice abundances outside their

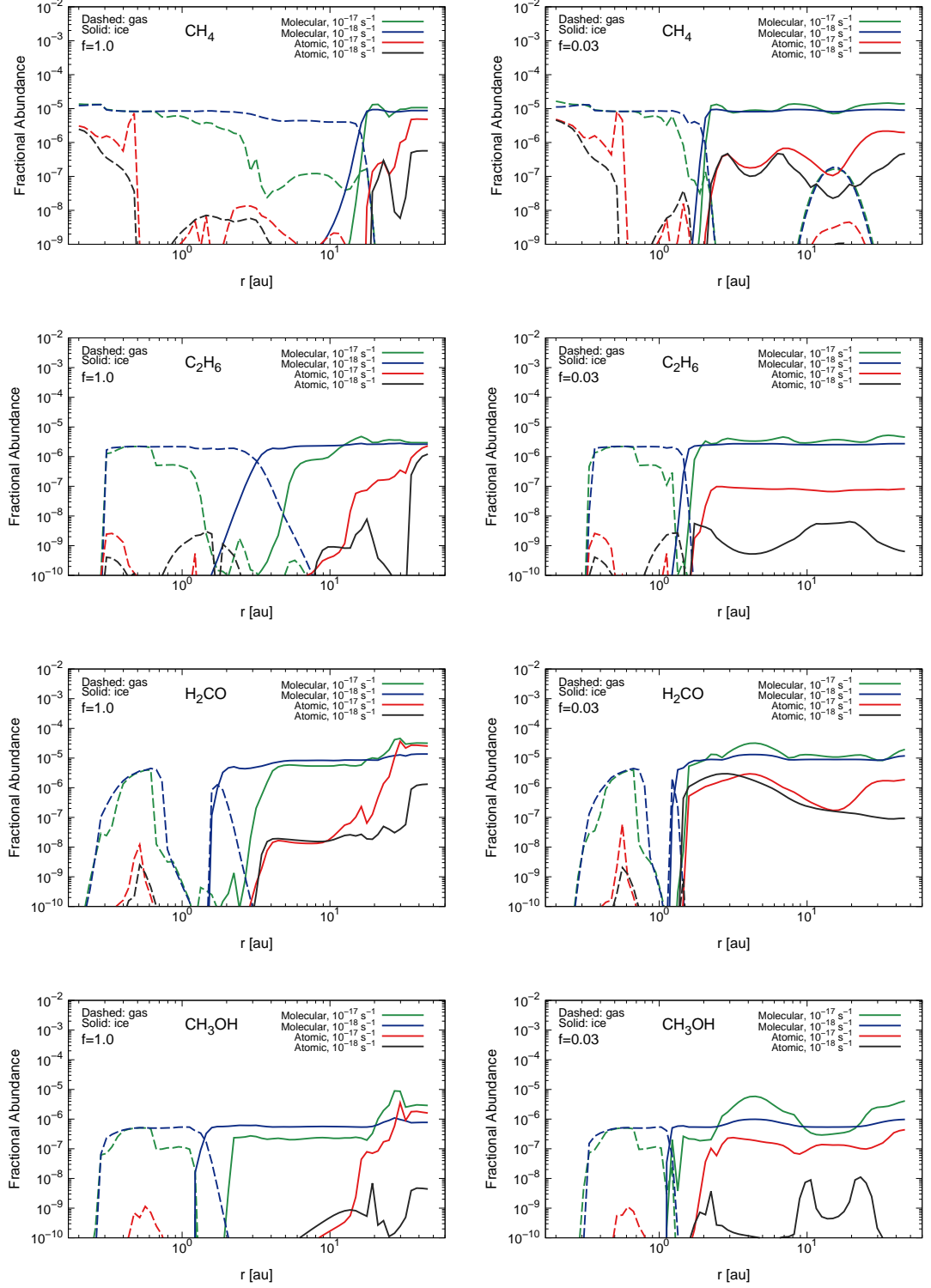


Figure 15. Same as Figure 14, but for CH_4 (top panels), C_2H_6 (second row panels), H_2CO (third row panels), and CH_3OH (bottom panels).

snowlines ($< 10^{-6}$ for CH_4 ice and $< 10^{-6}$ for C_2H_6 ice) are much smaller than those for molecular initial abundances ($\sim 10^{-5}$ for CH_4 ice and $\gtrsim 10^{-6}$ for C_2H_6 ice).

For molecular initial abundances, H_2CO and CH_3OH ice abundances between their snowlines and the CO snowline are larger for the low ionisation rate ($\sim 2 \times 10^{-7}$ for CH_3OH ice) than those for the high ionisation rate ($\sim 5 \times 10^{-7}$ for CH_3OH ice). We note that cosmic-ray photodissociation of these molecules are efficient in these regions and produce many radicals, which creates more complex organic molecules (see Section 3.2.2). In addition, H_2CO and CH_3OH ice abundances outside the CO snowline (including the shadowed region) are smaller for the low ionisation rate ($\gtrsim 10^{-6}$ for CH_3OH ice) than those for the high ionisation rate ($\gtrsim 3 \times 10^{-6}$ for CH_3OH ice). This is because H_2CO and CH_3OH ice are mainly formed by the sequential hydrogenation of CO on the grains surfaces (see Reactions 10 and 11), and the atomic hydrogen needed to hydrogenate CO is an end product of H_2 ionization (e.g., Schwarz et al. 2018).

For atomic initial abundances, both H_2CO and CH_3OH ice abundances at $r \sim 2 - 10$ au significantly decrease. The H_2CO ice abundances at such radii are $\ll 10^{-7}$ in the non-shadowed disk ($f = 1.0$) and $\sim (1 - 6) \times 10^{-6}$ in the shadowed disk ($f \leq 0.03$). The CH_3OH ice abundances are $\ll 10^{-8}$ in the non-shadowed disk ($f = 1.0$) and $\sim (1 - 3) \times 10^{-7}$ in the shadowed disk ($f \leq 0.03$). Schwarz et al. (2018) discussed that the timescales needed to build a reservoir of CH_3OH ice are longer than those needed for CO_2 , because CO_2 can form directly from CO ice (see Reactions 6) while CH_3OH ice is formed via a series of hydrogenation reactions.

A.3. Dominant nitrogen-bearing molecules

Unlike the case for CO, N_2 gas and ice abundance profiles barely change for different initial abundances and ionisation rates.

For molecular initial abundances, NH_3 gas and ice abundances around the NH_3 snowline decrease with increasing the ionisation rate. This is because NH_3 is converted into N_2 both through ion-molecule reactions as well as through cosmic-ray-induced photoreactions (Eistrup et al. 2016). In addition, for molecular initial abundances, NH_3 ice abundances at $r > 5$ au are $\sim 1 \times 10^{-5}$. In contrast, for atomic initial abundances NH_3 ice abundances at $r > 5$ au decrease ($\sim 10^{-6} - 10^{-5}$ for the high ionisation rate and $\sim 10^{-7} - 10^{-6}$ for the low ionisation rate). Schwarz & Bergin (2014) and Eistrup et al. (2016) noted that under atomic initial abundances, atomic N quickly forms N_2 gas.

Between the HCN and CO snowlines, HCN ice abundances are larger for molecular initial abundances ($\sim 10^{-6} - 10^{-5}$) than those for atomic initial abundances ($\sim 10^{-7} - 10^{-6}$). In contrast, HCN ice abundances just outside the CO snowline (including the shadowed region) are similar ($\sim (3 - 5) \times 10^{-6}$) both for the atomic and molecular initial abundances. This is because HCN is formed through the gas-phase reaction of HCO with N atom, with subsequent freeze-out onto dust grains, where HCO is formed by hydrogenation of CO on the dust grain surface (see Section 3.2.3 and e.g., Aikawa et al. 1999; Eistrup et al. 2016).

Between the NH_2CHO and CO snowlines, NH_2CHO ice abundances are larger for molecular initial abundances ($\sim 10^{-6} - 10^{-5}$ at $r \sim 1 - 5$ au) than those for atomic initial abundances ($\sim 10^{-9} - 10^{-8}$ at $r \sim 1 - 5$ au). Just outside the CO snowline (including the shadowed region), NH_2CHO ice abundances for molecular initial abundances are around $10^{-6} - 10^{-5}$. In addition, NH_2CHO ice abundances for atomic initial abundances significantly increase with increasing the ionisation rate. We find that NH_2CHO ice can form via the subsequent hydrogenation of OCN in the cold region (see Reaction 13 in Section 3.2.3 and Garrod et al. 2008; Walsh et al. 2014; López-Sepulcre et al. 2015), and the atomic hydrogen is an end product of H_2 ionization.

B. TIME EVOLUTION OF MOLECULAR ABUNDANCES

Figures 17-19 show the time evolution of the radial profiles of fractional abundances for dominant oxygen-, carbon-, nitrogen-bearing molecules (H_2O , CO, CO_2 , O_2 , CH_4 , C_2H_6 , H_2CO , CH_3OH , N_2 , NH_3 , HCN, and NH_2CHO) in the shadowed and non-shadowed disk midplane ($f = 1.0$ and $f = 0.03$, respectively), for molecular initial abundances and a high ionization rate ($\xi_{\text{CR}}(r) = 10^{-17} [\text{s}^{-1}]$). These initial conditions are same as those in Sections 3.1 and 3.2.

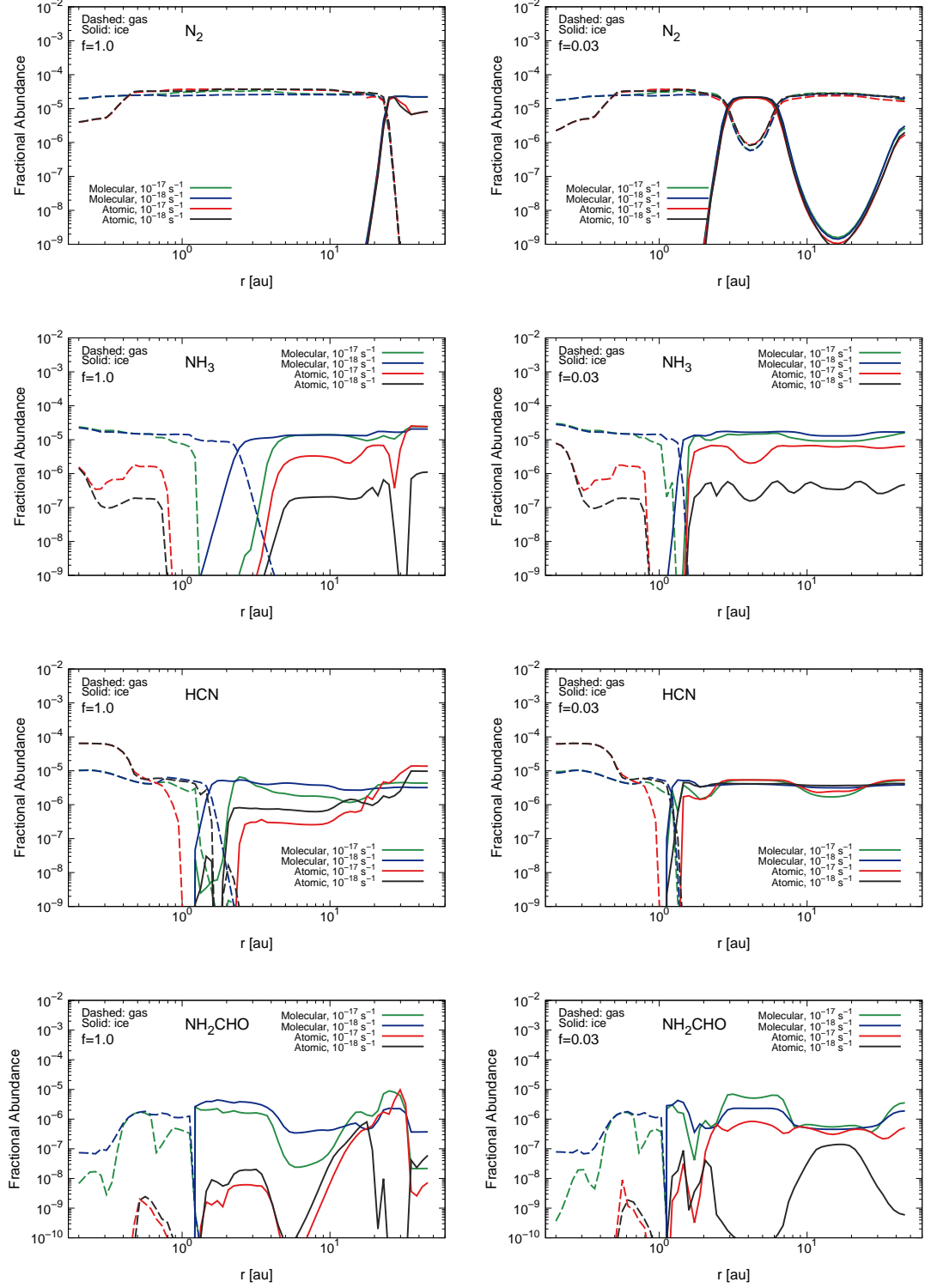


Figure 16. Same as Figure 14, but for N_2 (top panels), NH_3 (second row panels), HCN (third row panels), and NH_2CHO (bottom panels).

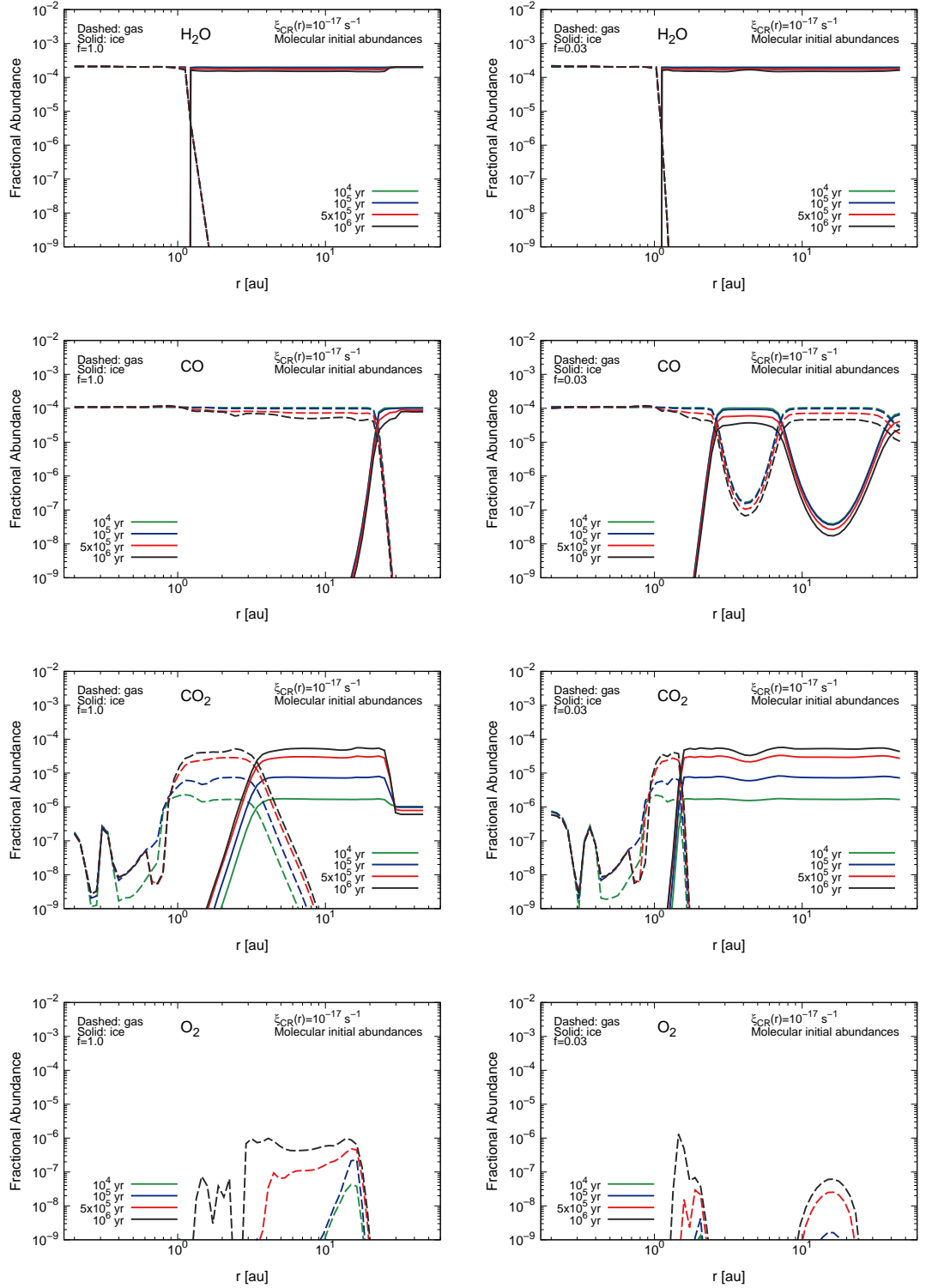


Figure 17. The time evolution of the radial profiles of fractional abundances with respect to total hydrogen nuclei densities for H_2O (top panels), CO (second row panels), CO_2 (third row panels), and O_2 (bottom panels). The dashed and solid lines show the profiles for gaseous and icy molecules, respectively. The green, blue, red, and black lines show the profiles for different evolutionary stage ($t=10^4$, 10^5 , 5×10^5 , and 10^6 years), respectively. These panels show the results when assuming molecular initial abundances (the “inheritance” scenario) and for $\xi_{\text{CR}}(r) = 1.0 \times 10^{-17} [\text{s}^{-1}]$. Left panels show those for the disk midplane with the monotonically decreasing temperature and density structure ($f = 1.0$), and right panels show the results for the shadowed disk midplane ($f = 0.03$).

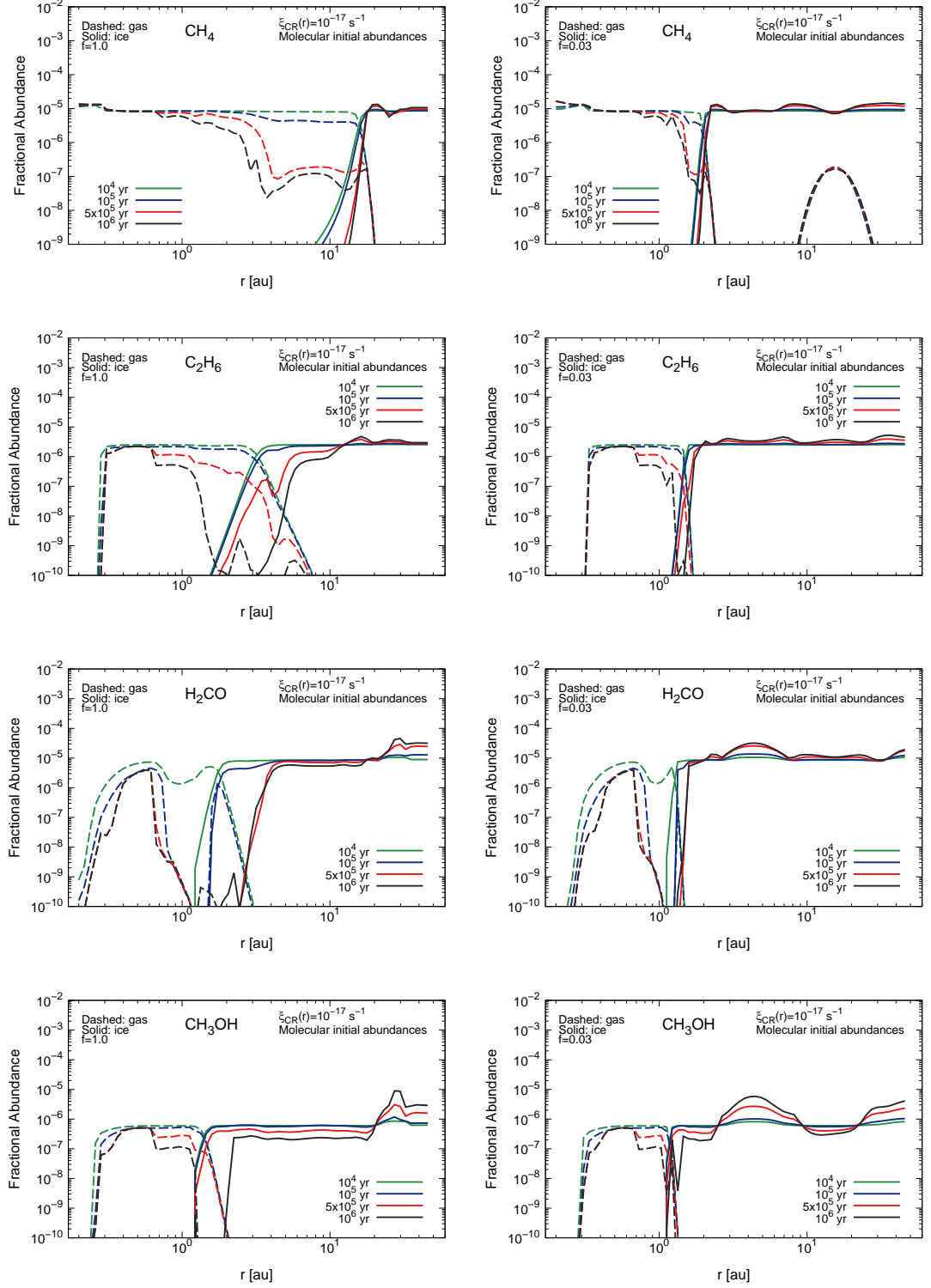


Figure 18. Same as Figure 17, but for CH_4 (top panels), C_2H_6 (second row panels), H_2CO (third row panels), and CH_3OH (bottom panels).

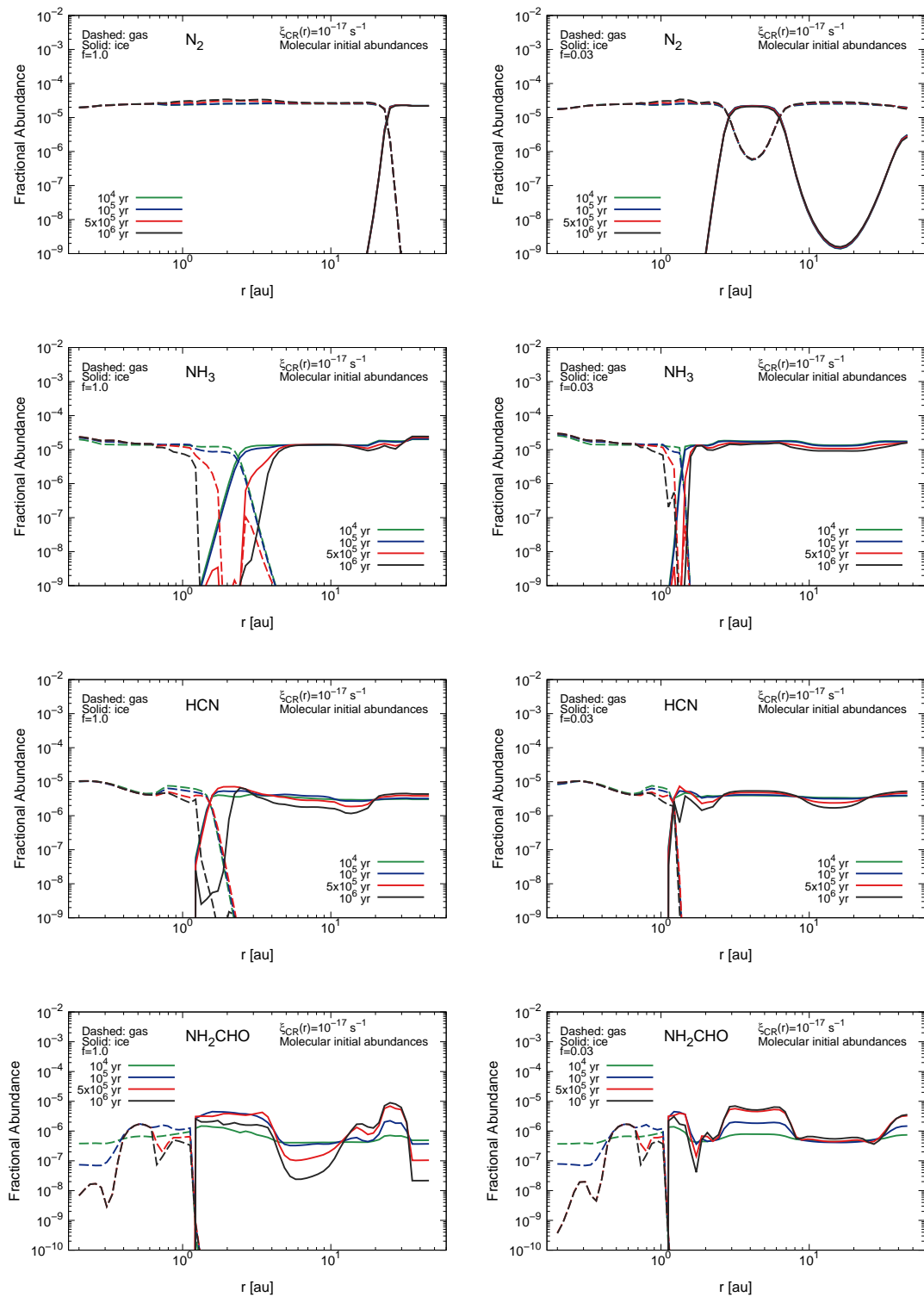


Figure 19. Same as Figure 17, but for N_2 (top panels), NH_3 (second row panels), HCN (third row panels), and NH_2CHO (bottom panels).

According to these Figures, H₂O and N₂ abundances do not change with time (see Table 2). O₂ gas abundances inside its snowline increase with time (from $\ll 10^{-9}$ at $t \lesssim 10^5$ years to $\sim 10^{-6}$ at $t \sim 10^6$ years).

Both CO gas and ice abundances (inside and outside the CO snowline, respectively) decrease with time (from $\sim 10^{-4}$ at $t \lesssim 10^5$ years to $\sim (3-5) \times 10^{-5}$ at $t \sim 10^6$ years). In contrast, both CO₂ gas and ice abundances (inside and outside the CO₂ snowline, respectively) increase with time (from $\ll 10^{-5}$ at $t < 10^5$ years to $\sim 5 \times 10^{-5}$ at $t \sim 10^6$ years), Eistrup et al. (2018) discussed that the decreasing abundance of CO gas and increasing abundance of CO₂ ice with time between CO₂ and CO snowlines can be explained by CO gas collisions with the grains, followed by fast reactions with OH (faster than CO can desorb) that produce CO₂ on dust grain surfaces. Bosman et al. (2018) discussed that for $\xi_{\text{CR}}(r) = 1.0 \times 10^{-17} [\text{s}^{-1}]$, the CO abundance can be reduced by two orders of magnitude in $t \sim (2-3) \times 10^6$ years.

As previous studies have shown (see e.g., Eistrup et al. 2018), CH₄ gas abundances within its snowline decrease with time (from $\gtrsim 5 \times 10^{-6}$ at $t \lesssim 10^5$ years to $\lesssim 10^{-7}$ at $t \gtrsim 5 \times 10^5$ years) and convert to CO₂ (see Section 3.2.2). In addition, we show that abundances of other molecules such as C₂H₆, H₂CO, CH₃OH, and NH₃ decrease with time around their own snowlines. We predict that in these regions gas-phase destruction processes (ion-molecule reactions and cosmic-ray-induced photodissociation) and cosmic-ray-induced photodesorption/photodissociation overcome the production processes in gas and on the dust grain surfaces, respectively.

In the region where CO is frozen-out onto dust grains (including the shadowed region for $f \leq 0.03$), the abundances of e.g., H₂CO, CH₃OH, and NH₂CHO increase with time because of the grain-surface reactions (from $\lesssim 10^{-6}$ at $t \lesssim 10^5$ years to $\gtrsim 5 \times 10^{-6}$ at $t \sim 10^6$ years for CH₃OH). On the basis of these results, the timescales of gas-phase reactions (such as ion-molecule reactions and cosmic-ray-induced photodissociation) and cosmic-ray-induced photodesorption/photodissociation are generally shorter than those of the grain-surface formation reactions, such as sequential hydrogenation reactions.

The HCN ice abundances are slightly enhanced (from $\sim 3 \times 10^{-6}$ at 10^4 years to $\sim 5 \times 10^{-6}$ at 10^6 years) in the region where CO is frozen-out onto dust grains (including the shadowed region for $f \leq 0.03$). As we describe in Section 3.2.3, HCN ice is efficiently formed within the cold regions where CO freezes out onto dust grains. Schwarz & Bergin (2014) and Eistrup et al. (2018) described that HCN ice is efficiently produced by a few $\times 10^6$ years.

On the basis of these results, in the shadowed region ($r \sim 3-8$ au) the icy abundances of CO₂ and organic molecules such as H₂CO, CH₃OH, and NH₂CHO become larger with time. Thus, we find that if the shadowed region is maintained for a relatively long time ($t \sim 10^6$ years), chemical evolution may produce dust grains and solid objects with large amounts of CO₂ and organic molecular ices (see also Section 4.2). In addition, the ice abundances of these molecules can be a clue in constraining the formation age of solid bodies in the shadowed region.

We note that in our modeling, we assume a constant central stellar luminosity and a constant viscous accretion heating (see Section 2.1). Kunitomo et al. (2021) calculated that in the case of in the case of a T Tauri star with mass $M_* = 1.0 M_\odot$, the central star luminosity L_* gradually decreases from $\sim 5L_\odot$ at $t \sim 10^5$ years to $\lesssim L_\odot$ at $t \gtrsim 3 \times 10^6$ years. In addition, the viscous accretion heating determines the temperature in the inner disk (see Section 2.1). Thus, the disk temperature in the inner disk (around the water snowline) does not change very much within the timescale of 10^6 years by evolving stellar luminosity.

In addition, in reality the efficiency of viscous accretion heating also changes with time. Oka et al. (2011) described the relation between the midplane temperature and mass accretion rate: $T \propto \dot{M}^{1/4}$. Thus, based on Oka et al. (2011), the water snowline position expects to move inward (from ~ 5 au to ~ 1.3 au) as the mass accretion rate becomes around ten times smaller with time (from $t \sim 10^5$ years (Class 0-I disk) to $t \sim 10^6$ years (Class II disk)).

C. THE C/H, O/H, AND N/H RATIOS

Figures 20, 21, and 22 show respectively the radial profiles of C/H, O/H, and N/H ratios at $t = 10^6$ years. Different color lines show the profiles for different values of the parameter f ($=1.0, 0.3, 0.03, \text{ and } 0.003$), respectively. As

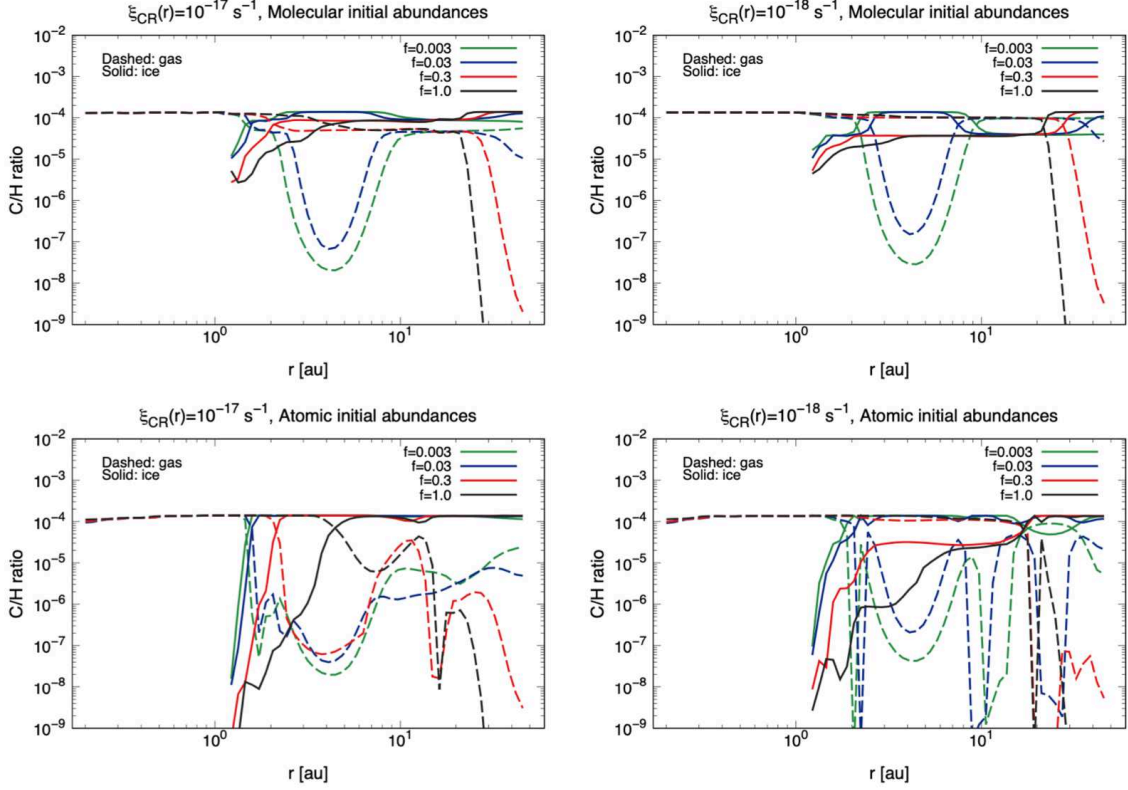


Figure 20. The radial profiles of C/H ratios at $t=10^6$ years. The dashed and solid lines show the profiles for gaseous and icy molecules, respectively. The black, red, blue, and green lines show the profiles for different values of the parameter f ($=1.0, 0.3, 0.03, \text{ and } 0.003$), respectively. Top panels show the results when assuming molecular initial abundances (the “inheritance” scenario), whereas bottom panels show those when assuming atomic initial abundances (“reset” scenario). Left panels show the results for $\xi_{\text{CR}}(r) = 1.0 \times 10^{-17} [\text{s}^{-1}]$, whereas right panels show the results for $\xi_{\text{CR}}(r) = 1.0 \times 10^{-18} [\text{s}^{-1}]$. The initial elemental C/H ratio is 1.40×10^{-4} .

described in our previous studies for the case of non-shadowed disk (see Section 2.3 and Figure 2 of Notsu et al. 2020), the inclusion of chemistry has a significant impact on the disk elemental abundances of both gas and ice.

In the non-shadowed disk ($f = 1.0$), for $\xi_{\text{CR}}(r) = 1.0 \times 10^{-18} [\text{s}^{-1}]$, the gas-phase C/H and O/H ratios are respectively $\sim 10^{-4}$ and $\sim (1 - 3) \times 10^{-4}$ at $r \lesssim 22$ au (within the CO snowline). In addition, for $\xi_{\text{CR}}(r) = 1.0 \times 10^{-17}$

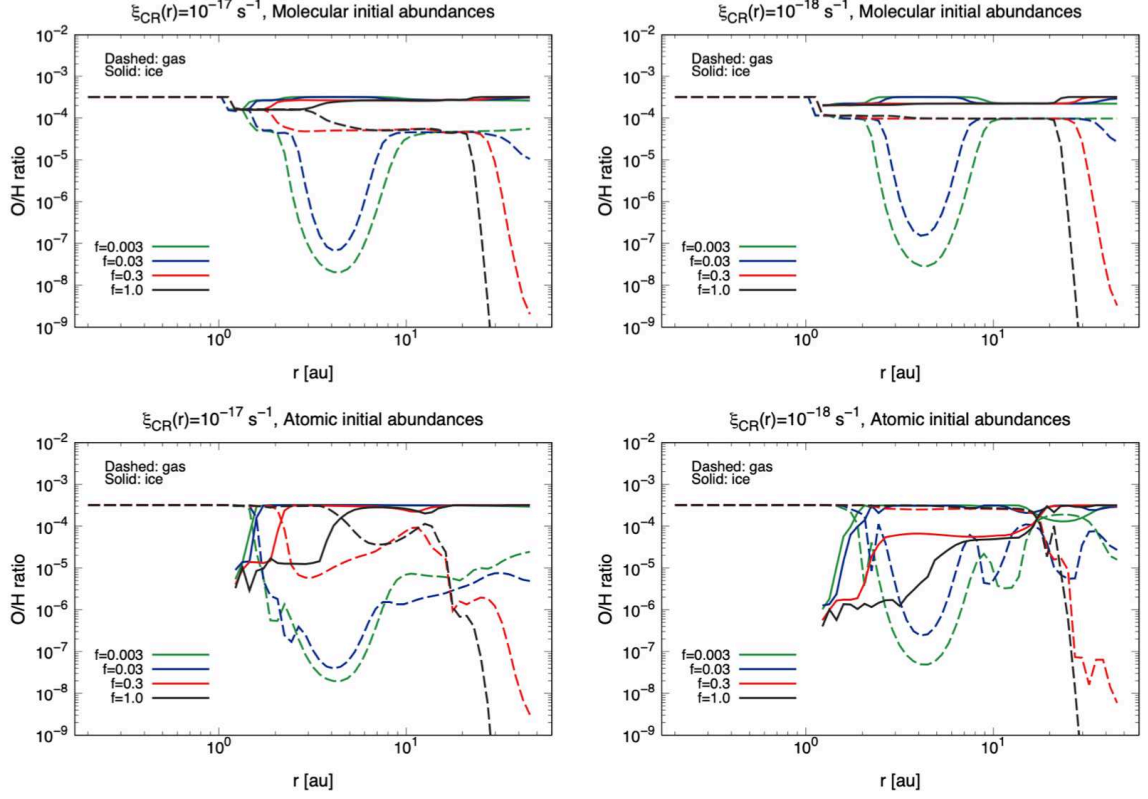


Figure 21. Same as Figure 20, but for the radial profiles of O/H ratios at $t=10^6$ years. The initial elemental O/H ratio is 3.20×10^{-4} .

$[\text{s}^{-1}]$, the gas-phase C/H and O/H ratios are respectively $\sim 10^{-4}$ and $\gtrsim 10^{-4}$ within the CO_2 snowline and respectively $\sim 10^{-6} - 5 \times 10^{-5}$ and $\sim 10^{-5} - 10^{-4}$ between the CO_2 and CO snowlines. This is because under the high ionisation rate ($\xi_{\text{CR}}(r) = 1.0 \times 10^{-17} [\text{s}^{-1}]$), CO and CH_4 gas are converted to less volatile molecules, such as CO_2 , H_2CO , and hydrocarbons (see Sections 3.2.1 and 3.2.2). Outside the CO snowline ($r > 22$ au), both gas-phase C/H and O/H abundances are $\ll 10^{-7}$. The icy-phase C/H and O/H ratios increase with increasing r , and reach the similar value as the initial elemental abundance outside the CO snowline.

In the non-shadowed disk ($f = 1.0$), the gas-phase N/H ratios are $\sim (5 - 7) \times 10^{-5}$ at $r \lesssim 24$ au (within the

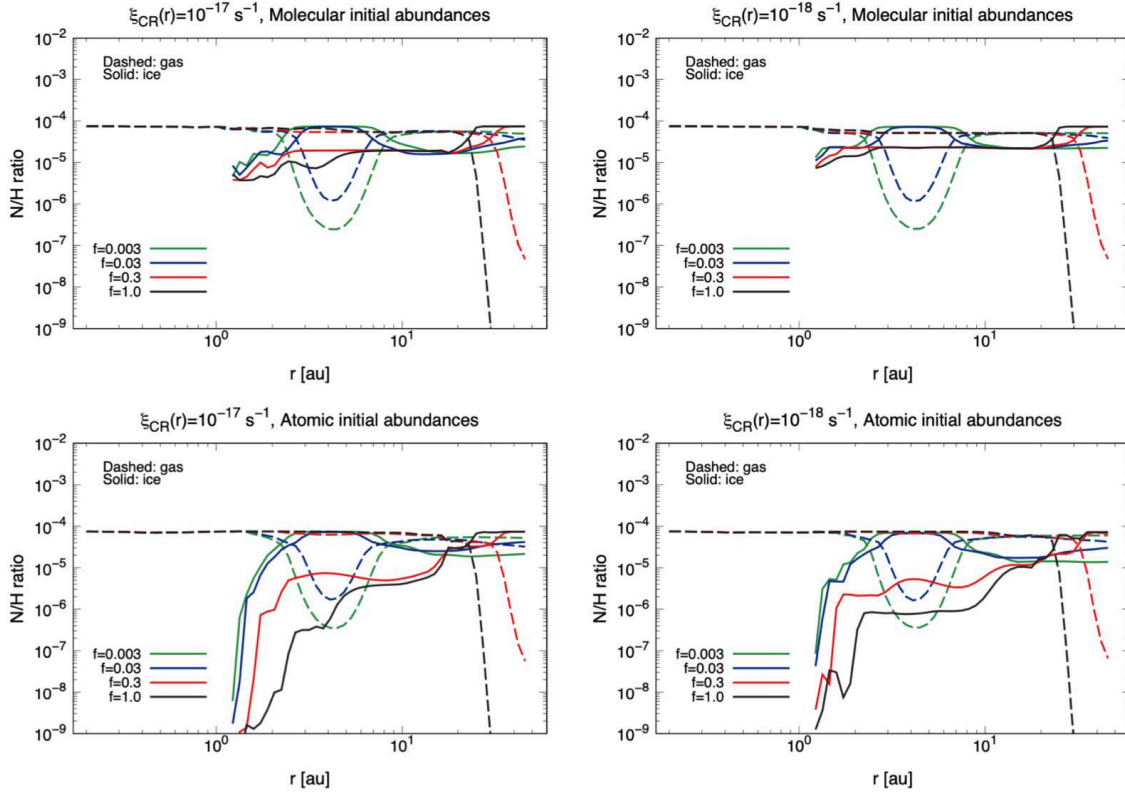


Figure 22. Same as Figure 20, but for the radial profiles of N/H ratios at $t=10^6$ years. The initial elemental N/H ratio is 7.50×10^{-5} .

N_2 snowline). Outside the N_2 snowline ($r > 24$ au), the gas-phase N/H abundances are $\ll 10^{-7}$. The icy-phase N/H ratios increase with increasing r , and reach the similar value as the initial elemental abundance outside the N_2 snowline.

In the shadowed disk ($f \leq 0.03$), at $r \sim 3 - 8$ au (around the current orbit of Jupiter), the gas-phase C/H and O/H ratios are both $\sim 10^{-8} - 10^{-6}$. In addition, at $r \sim 3 - 8$ au (around the current orbit of Jupiter), the gas-phase N/H ratios ($\sim 10^{-7} - 10^{-5}$) are larger than the gas-phase C/H and O/H ratios in each model, which produce super-

stellar N/O ratios of $\gg 1$ (see Figures 10 and 11). The icy-phase C/H, O/H, and N/H ratios reach the similar values as the initial elemental abundances.

REFERENCES

- Aikawa, Y., Cataldi, G., Yamato, Y., et al. 2021, *ApJS*, 257, 13. doi:10.3847/1538-4365/ac143c
- Aikawa, Y., Furuya, K., Nomura, H., et al. 2015, *ApJ*, 807, 120. doi:10.1088/0004-637X/807/2/120
- Aikawa, Y., Furuya, K., Yamamoto, S., et al. 2020, *ApJ*, 897, 110. doi:10.3847/1538-4357/ab994a
- Aikawa, Y., Umebayashi, T., Nakano, T., et al. 1999, *ApJ*, 519, 705. doi:10.1086/307400
- Alarcón, F., Teague, R., Zhang, K., et al. 2020, *ApJ*, 905, 68. doi:10.3847/1538-4357/abc1d6
- Altwegg, K., Balsiger, H., Berthelier, J. J., et al. 2017, *MNRAS*, 469, S130. doi:10.1093/mnras/stx1415
- Altwegg, K., Balsiger, H., & Fuselier, S. A. 2019, *ARA&A*, 57, 113. doi:10.1146/annurev-astro-091918-104409
- Andrews, S. M. 2020, *ARA&A*, 58, 483. doi:10.1146/annurev-astro-031220-010302
- Andrews, S. M., Huang, J., Pérez, L. M., et al. 2018, *ApJL*, 869, L41. doi:10.3847/2041-8213/aaf741
- Andrews, S. M., Wilner, D. J., Zhu, Z., et al. 2016, *ApJL*, 820, L40. doi:10.3847/2041-8205/820/2/L40
- Arakawa, S. & Krijt, S. 2021, *ApJ*, 910, 130. doi:10.3847/1538-4357/abe61d
- Arasa, C., Andersson, S., Cuppen, H. M., et al. 2010, *JChPh*, 132, 184510. doi:10.1063/1.3422213
- Arasa, C., Koning, J., Kroes, G.-J., et al. 2015, *A&A*, 575, A121. doi:10.1051/0004-6361/201322695
- Atkinson, R., Baulch, D. L., Cox, R. A., et al. 2006, *Atmospheric Chemistry & Physics*, 6, 3625. doi:10.5194/acp-6-3625-2006
- Atreya, S. K., Crida, A., Guillot, T., et al. 2018, *Saturn in the 21st Century*, 5. doi:10.1017/9781316227220.002
- Atreya, S. K., Hofstadter, M. H., In, J. H., et al. 2020, *SSRv*, 216, 18. doi:10.1007/s11214-020-0640-8
- Banzatti, A., Pinilla, P., Ricci, L., et al. 2015, *ApJL*, 815, L15. doi:10.1088/2041-8205/815/1/L15
- Bergner, J. B., Guzmán, V. G., Öberg, K. I., et al. 2018, *ApJ*, 857, 69. doi:10.3847/1538-4357/aab664
- Bergner, J. B., Öberg, K. I., Bergin, E. A., et al. 2020, *ApJ*, 898, 97. doi:10.3847/1538-4357/ab9e71
- Bertin, M., Romanzin, C., Doronin, M., et al. 2016, *ApJL*, 817, L12. doi:10.3847/2041-8205/817/2/L12
- Bieler, A., Altwegg, K., Balsiger, H., et al. 2015, *Nature*, 526, 678. doi:10.1038/nature15707
- Birnstiel, T., Dullemond, C. P., & Brauer, F. 2010, *A&A*, 513, A79. doi:10.1051/0004-6361/200913731
- Birnstiel, T., Dullemond, C. P., Zhu, Z., et al. 2018, *ApJL*, 869, L45. doi:10.3847/2041-8213/aaf743
- Bitsch, B., Izidoro, A., Johansen, A., et al. 2019, *A&A*, 623, A88. doi:10.1051/0004-6361/201834489
- Bockelée-Morvan, D., Lis, D. C., Wink, J. E., et al. 2000, *A&A*, 353, 1101
- Booth, R. A., Clarke, C. J., Madhusudhan, N., et al. 2017, *MNRAS*, 469, 3994. doi:10.1093/mnras/stx1103
- Booth, R. A. & Ilee, J. D. 2019, *MNRAS*, 487, 3998. doi:10.1093/mnras/stz1488
- Booth, A. S., Walsh, C., Terwisscha van Scheltinga, J., et al. 2021a, *Nature Astronomy*, 5, 684. doi:10.1038/s41550-021-01352-w
- Booth, A. S., van der Marel, N., Leemker, M., et al. 2021b, *A&A*, 651, L6. doi:10.1051/0004-6361/202141057
- Bosman, A. D. & Banzatti, A. 2019, *A&A*, 632, L10. doi:10.1051/0004-6361/201936638
- Bosman, A. D., Cridland, A. J., & Miguel, Y. 2019, *A&A*, 632, L11. doi:10.1051/0004-6361/201936827
- Bosman, A. D., Walsh, C., & van Dishoeck, E. F. 2018, *A&A*, 618, A182. doi:10.1051/0004-6361/201833497
- Brogi, M. & Line, M. R. 2019, *AJ*, 157, 114. doi:10.3847/1538-3881/aaffd3
- Brunken, N. G. C., Booth, A. S., Leemker, M., et al. 2022, *A&A*, 659, A29. doi:10.1051/0004-6361/202142981
- Carney, M. T., Hogerheijde, M. R., Guzmán, V. V., et al. 2019, *A&A*, 623, A124. doi:10.1051/0004-6361/201834353
- Caselli, P. & Ceccarelli, C. 2012, *A&A Rv*, 20, 56. doi:10.1007/s00159-012-0056-x
- Changeat, Q., Al-Refaie, A., Mugnai, L. V., et al. 2020, *AJ*, 160, 80. doi:10.3847/1538-3881/ab9a53
- Chiang, E. I. & Goldreich, P. 1997, *ApJ*, 490, 368. doi:10.1086/304869
- Chuang, K.-J., Fedoseev, G., Ioppolo, S., et al. 2016, *MNRAS*, 455, 1702. doi:10.1093/mnras/stv2288
- Cieza, L. A., Casassus, S., Tobin, J., et al. 2016, *Nature*, 535, 258. doi:10.1038/nature18612
- Cleeves, L. I. 2016, *ApJL*, 816, L21. doi:10.3847/2041-8205/816/2/L21
- Cleeves, L. I., Adams, F. C., & Bergin, E. A. 2013a, *ApJ*, 772, 5. doi:10.1088/0004-637X/772/1/5
- Cleeves, L. I., Adams, F. C., Bergin, E. A., et al. 2013b, *ApJ*, 777, 28. doi:10.1088/0004-637X/777/1/28
- Cleeves, L. I., Bergin, E. A., & Adams, F. C. 2014b, *ApJ*, 794, 123. doi:10.1088/0004-637X/794/2/123

- Cleeves, L. I., Bergin, E. A., Alexander, C. M. O. 'D., et al. 2014a, *Science*, 345, 1590. doi:10.1126/science.1258055
- Cridland, A. J., Pudritz, R. E., Birnstiel, T., et al. 2017, *MNRAS*, 469, 3910. doi:10.1093/mnras/stx1069
- Cridland, A. J., Bosman, A. D., & van Dishoeck, E. F. 2020a, *A&A*, 635, A68. doi:10.1051/0004-6361/201936858
- Cridland, A. J., van Dishoeck, E. F., Alessi, M., et al. 2020b, *A&A*, 642, A229. doi:10.1051/0004-6361/202038767
- Cruz-Diaz, G. A., Martín-Doménech, R., Muñoz Caro, G. M., et al. 2016, *A&A*, 592, A68. doi:10.1051/0004-6361/201526761
- Cuppen, H. M., van Dishoeck, E. F., Herbst, E., et al. 2009, *A&A*, 508, 275. doi:10.1051/0004-6361/200913119
- Cuppen, H. M., Walsh, C., Lamberts, T., et al. 2017, *SSRv*, 212, 1. doi:10.1007/s11214-016-0319-3
- Dartois, E., Engrand, C., Brunetto, R., et al. 2013, *Icarus*, 224, 243. doi:10.1016/j.icarus.2013.03.002
- Dartois, E., Engrand, C., Duprat, J., et al. 2018, *A&A*, 609, A65. doi:10.1051/0004-6361/201731322
- Dash, S., Majumdar, L., Willacy, K., et al. 2022, *ApJ*, 932, 20. doi:10.3847/1538-4357/ac67f0
- DeMeo, F. E. & Carry, B. 2014, *Nature*, 505, 629. doi:10.1038/nature12908
- Draine, B. T. 2003, *ARA&A*, 41, 241. doi:10.1146/annurev.astro.41.011802.094840
- Drażkowska, J. & Alibert, Y. 2017, *A&A*, 608, A92. doi:10.1051/0004-6361/201731491
- Drozdovskaya, M. N., van Dishoeck, E. F., Rubin, M., et al. 2019, *MNRAS*, 490, 50. doi:10.1093/mnras/stz2430
- Drozdovskaya, M. N., Walsh, C., van Dishoeck, E. F., et al. 2016, *MNRAS*, 462, 977. doi:10.1093/mnras/stw1632
- Drozdovskaya, M. N., Walsh, C., Visser, R., et al. 2014, *MNRAS*, 445, 913. doi:10.1093/mnras/stu1789
- Dullemond, C. P., Birnstiel, T., Huang, J., et al. 2018, *ApJL*, 869, L46. doi:10.3847/2041-8213/aaf742
- Dullemond, C. P. & Dominik, C. 2004, *A&A*, 417, 159. doi:10.1051/0004-6361:20031768
- Dullemond, C. P., Dominik, C., & Natta, A. 2001, *ApJ*, 560, 957. doi:10.1086/323057
- Dullemond, C. P., Juhasz, A., Pohl, A., et al. 2012, *RADMC-3D: A Multi-purpose Radiative Transfer Tool, Astrophysics Source Code Library*, ascl:1202.015
- Dullemond, C. P. & Monnier, J. D. 2010, *ARA&A*, 48, 205. doi:10.1146/annurev-astro-081309-130932
- Eistrup, C. & Walsh, C. 2019, *A&A*, 621, A75. doi:10.1051/0004-6361/201833380
- Eistrup, C., Walsh, C., & van Dishoeck, E. F. 2016, *A&A*, 595, A83. doi:10.1051/0004-6361/201628509
- Eistrup, C., Walsh, C., & van Dishoeck, E. F. 2018, *A&A*, 613, A14. doi:10.1051/0004-6361/201731302
- Favre, C., Fedele, D., Semenov, D., et al. 2018, *ApJL*, 862, L2. doi:10.3847/2041-8213/aad046
- Fillion, J.-H., Fayolle, E. C., Michaut, X., et al. 2014, *Faraday Discussions*, 168, 533. doi:10.1039/C3FD00129F
- Flock, M., Fromang, S., Turner, N. J., et al. 2016, *ApJ*, 827, 144. doi:10.3847/0004-637X/827/2/144
- Fockenberg, C. & Preses, J. M. 2002, *Journal of Physical Chemistry A*, 106, 2924. doi:10.1021/jp0141880
- Fritscher, M. & Teiser, J. 2021, *ApJ*, 923, 134. doi:10.3847/1538-4357/ac2df4
- Fuchs, G. W., Cuppen, H. M., Ioppolo, S., et al. 2009, *A&A*, 505, 629. doi:10.1051/0004-6361/200810784
- Fujii, Y. I. & Kimura, S. S. 2022, *ApJL* in press (arXiv: 2208.02503)
- Fujiya, W., Hoppe, P., Ushikubo, T., et al. 2019, *Nature Astronomy*, 3, 910. doi:10.1038/s41550-019-0801-4
- Furuya, K. & Aikawa, Y. 2014, *ApJ*, 790, 97. doi:10.1088/0004-637X/790/2/97
- Furuya, K., Drozdovskaya, M. N., Visser, R., et al. 2017, *A&A*, 599, A40. doi:10.1051/0004-6361/201629269
- Furuya, K., van Dishoeck, E. F., & Aikawa, Y. 2016, *A&A*, 586, A127. doi:10.1051/0004-6361/201527579
- Gandhi, S., Madhusudhan, N., Hawker, G., et al. 2019, *AJ*, 158, 228. doi:10.3847/1538-3881/ab4efc
- Garrod, R. T. & Herbst, E. 2006, *A&A*, 457, 927. doi:10.1051/0004-6361:20065560
- Garrod, R. T., Widicus Weaver, S. L., & Herbst, E. 2008, *ApJ*, 682, 283. doi:10.1086/588035
- Giacobbe, P., Brogi, M., Gandhi, S., et al. 2021, *Nature*, 592, 205. doi:10.1038/s41586-021-03381-x
- Graedel, T. E., Langer, W. D., & Frerking, M. A. 1982, *ApJS*, 48, 321. doi:10.1086/190780
- Gredel, R., Lepp, S., & Dalgarno, A. 1987, *ApJL*, 323, L137. doi:10.1086/185073
- Gredel, R., Lepp, S., Dalgarno, A., et al. 1989, *ApJ*, 347, 289. doi:10.1086/168117
- Guzmán, V. V., Bergner, J. B., Law, C. J., et al. 2021, *ApJS*, 257, 6. doi:10.3847/1538-4365/ac1440
- Hansen, B. M. S. 2009, *ApJ*, 703, 1131. doi:10.1088/0004-637X/703/1/1131
- Hasegawa, T. I. & Herbst, E. 1993, *MNRAS*, 261, 83. doi:10.1093/mnras/261.1.83
- Hasegawa, T. I., Herbst, E., & Leung, C. M. 1992, *ApJS*, 82, 167. doi:10.1086/191713
- Hawker, G. A., Madhusudhan, N., Cabot, S. H. C., et al. 2018, *ApJL*, 863, L11. doi:10.3847/2041-8213/aac49d
- Hayashi, C. 1981, *Progress of Theoretical Physics Supplement*, 70, 35. doi:10.1143/PTPS.70.35

- Heinzeller, D., Nomura, H., Walsh, C., et al. 2011, *ApJ*, 731, 115. doi:10.1088/0004-637X/731/2/115
- Helling, C., Woitke, P., Rimmer, P. B., et al. 2014, *Life*, 4, 142. doi:10.3390/life4020142
- Henning, T. & Stognienko, R. 1996, *A&A*, 311, 291
- Herbst, E. & van Dishoeck, E. F. 2009, *ARA&A*, 47, 427. doi:10.1146/annurev-astro-082708-101654
- Hollenbach, D., Kaufman, M. J., Bergin, E. A., et al. 2009, *ApJ*, 690, 1497. doi:10.1088/0004-637X/690/2/1497
- Hori, Y. & Ikoma, M. 2011, *MNRAS*, 416, 1419. doi:10.1111/j.1365-2966.2011.19140.x
- Huang, J., Andrews, S. M., Dullemond, C. P., et al. 2018, *ApJL*, 869, L42. doi:10.3847/2041-8213/aaf740
- Iaroslavitz, E. & Podolak, M. 2007, *Icarus*, 187, 600. doi:10.1016/j.icarus.2006.10.008
- Ilee, J. D., Walsh, C., Booth, A. S., et al. 2021, *ApJS*, 257, 9. doi:10.3847/1538-4365/ac1441
- Isella, A., Guidi, G., Testi, L., et al. 2016, *PhRvL*, 117, 251101. doi:10.1103/PhysRevLett.117.251101
- Isella, A., Huang, J., Andrews, S. M., et al. 2018, *ApJL*, 869, L49. doi:10.3847/2041-8213/aaf747
- Isella, A. & Turner, N. J. 2018, *ApJ*, 860, 27. doi:10.3847/1538-4357/aabb07
- Jang-Condell, H. & Turner, N. J. 2012, *ApJ*, 749, 153. doi:10.1088/0004-637X/749/2/153
- Jensen, S. S., Jørgensen, J. K., Kristensen, L. E., et al. 2021, *A&A*, 650, A172. doi:10.1051/0004-6361/202140560
- Jones, B. M., Bennett, C. J., & Kaiser, R. I. 2011, *ApJ*, 734, 78. doi:10.1088/0004-637X/734/2/78
- Jørgensen, J. K., Belloche, A., & Garrod, R. T. 2020, *ARA&A*, 58, 727. doi:10.1146/annurev-astro-032620-021927
- Kahane, C., Ceccarelli, C., Faure, A., et al. 2013, *ApJL*, 763, L38. doi:10.1088/2041-8205/763/2/L38
- Kenyon, S. J. & Hartmann, L. 1987, *ApJ*, 323, 714. doi:10.1086/165866
- Kouchi, A., Tsuboi, M., Hama, T., et al. 2021, *ApJ*, 918, 45. doi:10.3847/1538-4357/ac0ae6
- Krijt, S., Bosman, A. D., Zhang, K., et al. 2020, *ApJ*, 899, 134. doi:10.3847/1538-4357/aba75d
- Krijt, S., Schwarz, K. R., Bergin, E. A., et al. 2018, *ApJ*, 864, 78. doi:10.3847/1538-4357/aad69b
- Kruijjer, T. S., Burkhardt, C., Budde, G., et al. 2017, *Proceedings of the National Academy of Science*, 114, 6712. doi:10.1073/pnas.1704461114
- Kruijjer, T. S., Kleine, T., & Borg, L. E. 2020, *Nature Astronomy*, 4, 32. doi:10.1038/s41550-019-0959-9
- Kunitomo, M., Ida, S., Takeuchi, T., et al. 2021, *ApJ*, 909, 109. doi:10.3847/1538-4357/abdb2a
- Kurokawa, H., Shibuya, T., Sekine, Y., Ehlmann, B. L., Usui, F., Kikuchi, S., & Yoda, M. 2022, *AGU Advances*, 3, e2021AV000568. doi: 10.1029/2021AV000568
- Kusaka, T., Nakano, T., & Hayashi, C. 1970, *Progress of Theoretical Physics*, 44, 1580. doi:10.1143/PTP.44.1580
- Lee, J.-E., Lee, S., Baek, G., et al. 2019, *Nature Astronomy*, 3, 314. doi:10.1038/s41550-018-0680-0
- Leger, A., Jura, M., & Omont, A. 1985, *A&A*, 144, 147
- Le Roy, L., Altwegg, K., Balsiger, H., et al. 2015, *A&A*, 583, A1. doi:10.1051/0004-6361/201526450
- Li, C., Ingersoll, A., Bolton, S., et al. 2020, *Nature Astronomy*, 4, 609. doi:10.1038/s41550-020-1009-3
- Line, M. R., Brogi, M., Bean, J. L., et al. 2021, *Nature*, 598, 580. doi:10.1038/s41586-021-03912-6
- Loomis, R. A., Cleaves, L. I., Öberg, K. I., et al. 2015, *ApJL*, 809, L25. doi:10.1088/2041-8205/809/2/L25
- Loomis, R. A., Cleaves, L. I., Öberg, K. I., et al. 2018, *ApJ*, 859, 131. doi:10.3847/1538-4357/aac169
- Loomis, R. A., Öberg, K. I., Andrews, S. M., et al. 2020, *ApJ*, 893, 101. doi:10.3847/1538-4357/ab7cc8
- López-Sepulcre, A., Jaber, A. A., Mendoza, E., et al. 2015, *MNRAS*, 449, 2438. doi:10.1093/mnras/stv377
- Luspay-Kuti, A., Mousis, O., Pauzat, F., et al. 2022, *Nature Astronomy*. doi:10.1038/s41550-022-01614-1
- Lynden-Bell, D. & Pringle, J. E. 1974, *MNRAS*, 168, 603. doi:10.1093/mnras/168.3.603
- MacDonald, R. J. & Madhusudhan, N. 2017, *ApJL*, 850, L15. doi:10.3847/2041-8213/aa97d4
- Madhusudhan, N. 2019, *ARA&A*, 57, 617. doi:10.1146/annurev-astro-081817-051846
- Madhusudhan, N., Amin, M. A., & Kennedy, G. M. 2014, *ApJL*, 794, L12. doi:10.1088/2041-8205/794/1/L12
- Mandt, K. E., Mousis, O., Lunine, J., et al. 2020, *SSRv*, 216, 99. doi:10.1007/s11214-020-00723-5
- Mathis, J. S., Rimpl, W., & Nordsieck, K. H. 1977, *ApJ*, 217, 425. doi:10.1086/155591
- McElroy, D., Walsh, C., Markwick, A. J., et al. 2013, *A&A*, 550, A36. doi:10.1051/0004-6361/201220465
- Miura, H., Yamamoto, T., Nomura, H., et al. 2017, *ApJ*, 839, 47. doi:10.3847/1538-4357/aa67df
- Miyake, K. & Nakagawa, Y. 1993, *Icarus*, 106, 20. doi:10.1006/icar.1993.1156
- Moll, R., Garaud, P., Mankovich, C., et al. 2017, *ApJ*, 849, 24. doi:10.3847/1538-4357/aa8d74
- Mollière, P., Molyarova, T., Bitsch, B., et al. 2022, *ApJ*, 934, 74. doi:10.3847/1538-4357/ac6a56
- Molyarova, T., Akimkin, V., Semenov, D., et al. 2018, *ApJ*, 866, 46. doi:10.3847/1538-4357/aadfd9
- Morbidelli, A., Szulágyi, J., Crida, A., et al. 2014, *Icarus*, 232, 266. doi:10.1016/j.icarus.2014.01.010

- Mordasini, C., van Boekel, R., Mollière, P., et al. 2016, *ApJ*, 832, 41. doi:10.3847/0004-637X/832/1/41
- Mori, S., Okuzumi, S., Kunitomo, M., et al. 2021, *ApJ*, 916, 72. doi:10.3847/1538-4357/ac06a9
- Moses, J. I., Line, M. R., Visscher, C., et al. 2013, *ApJ*, 777, 34. doi:10.1088/0004-637X/777/1/34
- Moses, J. I., Visscher, C., Fortney, J. J., et al. 2011, *ApJ*, 737, 15. doi:10.1088/0004-637X/737/1/15
- Müller, J., Savvidou, S., & Bitsch, B. 2021, *A&A*, 650, A185. doi:10.1051/0004-6361/202039930
- Murillo, N. M., Hsieh, T.-H., & Walsh, C. 2022, *A&A* in press (arXiv: 2206.04314)
- Mumma, M. J. & Charnley, S. B. 2011, *ARA&A*, 49, 471. doi:10.1146/annurev-astro-081309-130811
- Musioliik, G., Teiser, J., Jankowski, T., et al. 2016a, *ApJ*, 818, 16. doi:10.3847/0004-637X/818/1/16
- Musioliik, G., Teiser, J., Jankowski, T., et al. 2016b, *ApJ*, 827, 63. doi:10.3847/0004-637X/827/1/63
- Nakamoto, T. & Nakagawa, Y. 1994, *ApJ*, 421, 640. doi:10.1086/173678
- Noble, J. A., Congiu, E., Dulieu, F., et al. 2012, *MNRAS*, 421, 768. doi:10.1111/j.1365-2966.2011.20351.x
- Noble, J. A., Theule, P., Borget, F., et al. 2013, *MNRAS*, 428, 3262. doi:10.1093/mnras/sts272
- Noble, J. A., Theule, P., Congiu, E., et al. 2015, *A&A*, 576, A91. doi:10.1051/0004-6361/201425403
- Nomura, H., Aikawa, Y., Tsujimoto, M., et al. 2007, *ApJ*, 661, 334. doi:10.1086/513419
- Nomura, H. & Millar, T. J. 2005, *A&A*, 438, 923. doi:10.1051/0004-6361:20052809
- Nomura, H., Tsukagoshi, T., Kawabe, R., et al. 2016, *ApJL*, 819, L7. doi:10.3847/2041-8205/819/1/L7
- Nomura, H., Tsukagoshi, T., Kawabe, R., et al. 2021, *ApJ*, 914, 113. doi:10.3847/1538-4357/abfb6a
- Notsu, S., Akiyama, E., Booth, A., et al. 2019, *ApJ*, 875, 96. doi:10.3847/1538-4357/ab0ae9
- Notsu, S., Eistrup, C., Walsh, C., & Nomura, H. 2020, *MNRAS*, 499, 2229. doi:10.1093/mnras/staa2944
- Notsu, S., Nomura, H., Ishimoto, D., et al. 2017, *ApJ*, 836, 118. doi:10.3847/1538-4357/836/1/118
- Notsu, S., Nomura, H., Ishimoto, D., et al. 2016, *ApJ*, 827, 113. doi:10.3847/0004-637X/827/2/113
- Notsu, S., Nomura, H., Walsh, C., et al. 2018, *ApJ*, 855, 62. doi:10.3847/1538-4357/aaaa72
- Notsu, S., van Dishoeck, E. F., Walsh, C., Bosman, A. D., & Nomura, H. 2021, *A&A*, 650, A180. doi:10.1051/0004-6361/202140667
- Öberg, K. I. & Bergin, E. A. 2016, *ApJL*, 831, L19. doi:10.3847/2041-8205/831/2/L19
- Öberg, K. I. & Bergin, E. A. 2021, *PhR*, 893, 1. doi:10.1016/j.physrep.2020.09.004
- Öberg, K. I., Fuchs, G. W., Awad, Z., et al. 2007, *ApJL*, 662, L23. doi:10.1086/519281
- Öberg, K. I., Guzmán, V. V., Furuya, K., et al. 2015, *Nature*, 520, 198. doi:10.1038/nature14276
- Öberg, K. I., Guzmán, V. V., Merchantz, C. J., et al. 2017, *ApJ*, 839, 43. doi:10.3847/1538-4357/aa689a
- Öberg, K. I., Guzmán, V. V., Walsh, C., et al. 2021, *ApJS*, 257, 1. doi:10.3847/1538-4365/ac1432
- Öberg, K. I., Linnartz, H., Visser, R., et al. 2009b, *ApJ*, 693, 1209. doi:10.1088/0004-637X/693/2/1209
- Öberg, K. I., Murray-Clay, R., & Bergin, E. A. 2011, *ApJL*, 743, L16. doi:10.1088/2041-8205/743/1/L16
- Öberg, K. I., van Broekhuizen, F., Fraser, H. J., et al. 2005, *ApJL*, 621, L33. doi:10.1086/428901
- Öberg, K. I., van Dishoeck, E. F., & Linnartz, H. 2009a, *A&A*, 496, 281. doi:10.1051/0004-6361/200810207
- Öberg, K. I. & Wordsworth, R. 2019, *AJ*, 158, 194. doi:10.3847/1538-3881/ab46a8
- Ohashi, S., Nakatani, R., Liu, H. B., et al. 2022, *ApJ*, 934, 163. doi:10.3847/1538-4357/ac794e
- Ohno, K. & Ueda, T. 2021, *A&A*, 651, L2. doi:10.1051/0004-6361/202141169
- Oka, A., Nakamoto, T., & Ida, S. 2011, *ApJ*, 738, 141. doi:10.1088/0004-637X/738/2/141
- Okoda, Y., Oya, Y., Abe, S., et al. 2021, *ApJ*, 923, 168. doi:10.3847/1538-4357/ac2c6c
- Okuzumi, S. & Tazaki, R. 2019, *ApJ*, 878, 132. doi:10.3847/1538-4357/ab204d
- Okuzumi, S., Ueda, T., & Turner, N. J. 2022, *PASJ*, psac040. doi: 10.1093/pasj/psac040/6612125
- Owen, T., Mahaffy, P., Niemann, H. B., et al. 1999, *Nature*, 402, 269. doi:10.1038/46232
- Padovani, M., Ivlev, A. V., Galli, D., et al. 2018, *A&A*, 614, A111. doi:10.1051/0004-6361/201732202
- Pegues, J., Öberg, K. I., Bergner, J. B., et al. 2020, *ApJ*, 890, 142. doi:10.3847/1538-4357/ab64d9
- Pelletier, S., Benneke, B., Darveau-Bernier, A., et al. 2021, *AJ*, 162, 73. doi:10.3847/1538-3881/ac0428
- Penteado, E. M., Walsh, C., & Cuppen, H. M. 2017, *ApJ*, 844, 71. doi:10.3847/1538-4357/aa78f9
- Pinilla, P., Pohl, A., Stammler, S. M., et al. 2017, *ApJ*, 845, 68. doi:10.3847/1538-4357/aa7edb
- Piso, A.-M. A., Pegues, J., & Öberg, K. I. 2016, *ApJ*, 833, 203. doi:10.3847/1538-4357/833/2/203
- Pontoppidan, K. M., Salyk, C., Bergin, E. A., et al. 2014, in *Protostars and Planets VI*, ed. H. Beuther et al. (Tucson, AZ: Univ. Arizona Press), 363. doi:10.2458/azu_uapress_9780816531240-ch016

- Pollack, J. B., Podolak, M., Bodenheimer, P., et al. 1986, *Icarus*, 67, 409. doi:10.1016/0019-1035(86)90123-5
- Pontoppidan, K. M., Salyk, C., Blake, G. A., et al. 2010, *ApJ*, 720, 887. doi:10.1088/0004-637X/720/1/887
- Prasad, S. S. & Tarafdar, S. P. 1983, *ApJ*, 267, 603. doi:10.1086/160896
- Pringle, J. E. 1981, *ARA&A*, 19, 137. doi:10.1146/annurev.aa.19.090181.001033
- Qi, C., Öberg, K. I., Espaillat, C. C., et al. 2019, *ApJ*, 882, 160. doi:10.3847/1538-4357/ab35d3
- Qi, C., Öberg, K. I., Wilner, D. J., et al. 2013, *ApJL*, 765, L14. doi:10.1088/2041-8205/765/1/L14
- Ros, K. & Johansen, A. 2013, *A&A*, 552, A137. doi:10.1051/0004-6361/201220536
- Rubin, M., Altwegg, K., Balsiger, H., et al. 2015a, *Science*, 348, 232. doi:10.1126/science.aaa6100
- Rubin, M., Altwegg, K., Balsiger, H., et al. 2019, *MNRAS*, 489, 594. doi:10.1093/mnras/stz2086
- Rubin, M., Altwegg, K., van Dishoeck, E. F., et al. 2015b, *ApJL*, 815, L11. doi:10.1088/2041-8205/815/1/L11
- Rubin, M., Engrand, C., Snodgrass, C., et al. 2020, *SSRv*, 216, 102. doi:10.1007/s11214-020-00718-2
- Sakai, N. & Yamamoto, S. 2013, *Chemical Reviews*, 113, 8981. doi:10.1021/cr4001308
- Saladino, R., Botta, G., Pino, S., Costanzo, G., Di Mauro, E. 2012, *Chem. Soc. Rev.*, 41, 5526. doi:10.1039/C2CS35066A
- Sato, T., Okuzumi, S., & Ida, S. 2016, *A&A*, 589, A15. doi:10.1051/0004-6361/201527069
- Schmalzl, M., Visser, R., Walsh, C., et al. 2014, *A&A*, 572, A81. doi:10.1051/0004-6361/201424236
- Schneider, A. D. & Bitsch, B. 2021, *A&A*, 654, A71. doi:10.1051/0004-6361/202039640
- Schuhmann, M., Altwegg, K., Balsiger, H., et al. 2019, *A&A*, 630, A31. doi:10.1051/0004-6361/201834666
- Schwarz, K. R. & Bergin, E. A. 2014, *ApJ*, 797, 113. doi:10.1088/0004-637X/797/2/113
- Schwarz, K. R., Bergin, E. A., Cleaves, L. I., et al. 2016, *ApJ*, 823, 91. doi:10.3847/0004-637X/823/2/91
- Schwarz, K. R., Bergin, E. A., Cleaves, L. I., et al. 2018, *ApJ*, 856, 85. doi:10.3847/1538-4357/aaae08
- Schwarz, K. R., Bergin, E. A., Cleaves, L. I., et al. 2019, *ApJ*, 877, 131. doi:10.3847/1538-4357/ab1c5e
- Seifert, R. A., Cleaves, L. I., Adams, F. C., et al. 2021, *ApJ*, 912, 136. doi:10.3847/1538-4357/abf09a
- Shakura, N. I. & Sunyaev, R. A. 1973, *A&A*, 500, 33
- Shibata, S. & Helled, R. 2022, *ApJL*, 926, L37. doi:10.3847/2041-8213/ac54b1
- Tanigawa, T., Ohtsuki, K., & Machida, M. N. 2012, *ApJ*, 747, 47. doi:10.1088/0004-637X/747/1/47
- Taquet, V., Furuya, K., Walsh, C., et al. 2016, *MNRAS*, 462, S99. doi:10.1093/mnras/stw2176
- Teague, R., Bae, J., & Bergin, E. A. 2019, *Nature*, 574, 378. doi:10.1038/s41586-019-1642-0
- Tielens, A. G. G. M. & Hagen, W. 1982, *A&A*, 114, 245
- Tinetti, G., Drossart, P., Eccleston, P., et al. 2018, *Experimental Astronomy*, 46, 135. doi:10.1007/s10686-018-9598-x
- Trapman, L., Zhang, K., van't Hoff, M. L. R., et al. 2022, *ApJL*, 926, L2. doi:10.3847/2041-8213/ac4f47
- Turner, N. J., Choukroun, M., Castillo-Rogez, J., et al. 2012, *ApJ*, 748, 92. doi:10.1088/0004-637X/748/2/92
- Turrini, D., Codella, C., Danielski, C., et al. 2021b, *Experimental Astronomy*. doi:10.1007/s10686-021-09754-4
- Turrini, D., Schisano, E., Fonte, S., et al. 2021a, *ApJ*, 909, 40. doi:10.3847/1538-4357/abd6e5
- Tsuchiyama, A., Miyake, A., Okuzumi, S., et al. 2021, *Science Advances*, 7, eabg9707. doi:10.1126/sciadv.abg9707
- Tsukagoshi, T., Nomura, H., Muto, T., et al. 2016, *ApJL*, 829, L35. doi:10.3847/2041-8205/829/2/L35
- Ueda, T., Flock, M., & Birnstiel, T. 2021, *ApJL*, 914, L38. doi:10.3847/2041-8213/ac0631
- Ueda, T., Flock, M., & Okuzumi, S. 2019, *ApJ*, 871, 10. doi:10.3847/1538-4357/aaf3a1
- Ueda, T., Okuzumi, S., & Flock, M. 2017, *ApJ*, 843, 49. doi:10.3847/1538-4357/aa74b5
- Umeyashiki, T. & Nakano, T. 2009, *ApJ*, 690, 69. doi:10.1088/0004-637X/690/1/69
- van der Marel, N., Booth, A. S., Leemker, M., et al. 2021, *A&A*, 651, L5. doi:10.1051/0004-6361/202141051
- van Dishoeck, E. F., Kristensen, L. E., Mottram, J. C., et al. 2021, *A&A*, 648, A24. doi:10.1051/0004-6361/202039084
- van 't Hoff, M. L. R., Walsh, C., Kama, M., et al. 2017, *A&A*, 599, A101. doi:10.1051/0004-6361/201629452
- Vasyunin, A. I. & Herbst, E. 2013, *ApJ*, 769, 34. doi:10.1088/0004-637X/769/1/34
- Venturini, J., Alibert, Y., & Benz, W. 2016, *A&A*, 596, A90. doi:10.1051/0004-6361/201628828
- Visser, R., van Dishoeck, E. F., Doty, S. D., et al. 2009, *A&A*, 495, 881. doi:10.1051/0004-6361/200810846
- Walsh, C., Loomis, R. A., Öberg, K. I., et al. 2016, *ApJL*, 823, L10. doi:10.3847/2041-8205/823/1/L10
- Walsh, C., Millar, T. J., & Nomura, H. 2010, *ApJ*, 722, 1607. doi:10.1088/0004-637X/722/2/1607
- Walsh, C., Millar, T. J., Nomura, H., et al. 2014, *A&A*, 563, A33. doi:10.1051/0004-6361/201322446

- Walsh, C., Nomura, H., Millar, T. J., et al. 2012, *ApJ*, 747, 114. doi:10.1088/0004-637X/747/2/114
- Walsh, C., Nomura, H., & van Dishoeck, E. 2015, *A&A*, 582, A88. doi:10.1051/0004-6361/201526751
- Walsh, C., Vissapragada, S., & McGee, H. 2018, *IAU Symposium*, 332, 395. doi:10.1017/S1743921317007037
- Watanabe, N. & Kouchi, A. 2002, *ApJL*, 571, L173. doi:10.1086/341412
- Warren, S. G., & Brandt, R. E. 2008, *J. Geophys. Res. (Atmos.)*, 113, D14220. doi:10.1029/2007JD009744
- Williams, J. P. & Cieza, L. A. 2011, *ARA&A*, 49, 67. doi:10.1146/annurev-astro-081710-102548
- Yada, T., Abe, M., Okada, T., et al. 2021, *Nature Astronomy*, 6, 214. doi:10.1038/s41550-021-01550-6
- Yang, Y.-L., Sakai, N., Zhang, Y., et al. 2021, *ApJ*, 910, 20. doi:10.3847/1538-4357/abdfd6
- Yu, M., Willacy, K., Dodson-Robinson, S. E., et al. 2016, *ApJ*, 822, 53. doi:10.3847/0004-637X/822/1/53
- Zhang, K., Booth, A. S., Law, C. J., et al. 2021, *ApJS*, 257, 5. doi:10.3847/1538-4365/ac1580
- Zhang, K., Schwarz, K. R., & Bergin, E. A. 2020, *ApJL*, 891, L17. doi:10.3847/2041-8213/ab7823